Primary nasal viral infection rewires the tissue-scale memory response

Samuel W. Kazer[1,2,3,4]*, Colette Matysiak Match[3,4]*, Erica M. Langan[1,2], Marie-Angèle Messou[3,4], Thomas J. LaSalle[2,5], Elise O'Leary[3], Jessica Marbourg[6], Katherine Naughton[7], Ulrich H. von Andrian[3,4,#], Jose Ordovas-Montanes[1,2,4,8,9,#,^]

[1]Division of Gastroenterology, Hepatology, and Nutrition, Boston Children's Hospital, Boston, MA, USA;

[2]Broad Institute of MIT and Harvard, Cambridge, MA, USA;

[3]Department of Immunology, Harvard Medical School, Boston, MA, USA;

[4]Ragon Institute of MGH, MIT and Harvard, Cambridge, MA, USA;

[5]Program in Health Sciences and Technology, Harvard Medical School & Massachusetts Institute of Technology, Boston, MA, USA;

[6]AbbVie Cambridge Research Center, Cambridge, MA, USA;

[7]AbbVie Genomics Research Center, North Chicago, IL, USA;

[8]Program in Immunology, Harvard Medical School, Boston, MA 02115, USA;

[9]Harvard Stem Cell Institute, Harvard University, Cambridge, MA, USA.

* These authors contributed equally to the work.

[#] These senior authors contributed equally to the work

^ Lead contact

Correspondence to Jose Ordovas-Montanes; jose.ordovas-montanes@childrens.harvard.edu

ABSTRACT

The nasal mucosa is frequently the initial site of respiratory viral infection, replication, and transmission. Recent work has started to clarify the independent responses of epithelial, myeloid, and lymphoid cells to viral infection in the nasal mucosa, but their spatiotemporal coordination and relative contributions remain unclear. Furthermore, understanding whether and how primary infection shapes tissue-scale memory responses to secondary challenge is critical for the rational design of nasal-targeting therapeutics and vaccines. Here, we generated a single-cell RNA-sequencing (scRNA-seq) atlas of the murine nasal mucosa sampling three distinct regions before and during primary and secondary influenza infection. Primary infection was largely restricted to respiratory mucosa and induced stepwise changes in cell type, subset, and state composition over time. Type I Interferon (IFN)-responsive neutrophils appeared 2 days post infection (dpi) and preceded transient IFN-responsive/cycling epithelial cell responses 5 dpi, which coincided with broader antiviral monocyte and NK cell accumulation. By 8 dpi, monocyte-derived macrophages (MDMs) expressing *Cxcl9* and *Cxcl16* arose alongside effector cytotoxic CD8 and *Ifng*-expressing CD4 T cells. Following viral clearance (14 dpi), rare, previously undescribed **K**rt13+ **n**asal **i**mmune-**i**nteracting **f**loor **e**pithelial (KNIIFE) cells expressing multiple genes with immune communication potential increased concurrently with tissue-resident memory T (T_{RM})-like cells and early IgG+/IgA+ plasmablasts. Proportionality analysis coupled with cell-cell communication inference, alongside validation by in situ microscopy, underscored the CXCL16–CXCR6 signaling axis between MDMs and effector CD8 T cells 8dpi and KNIIFE cells and T_{RM} cells 14 dpi. Secondary influenza challenge with a homologous or heterologous strain administered 60 dpi induced an accelerated and coordinated myeloid and lymphoid response without epithelial proliferation, illustrating how tissue-scale memory to natural infection engages both myeloid and lymphoid cells to reduce epithelial regenerative burden. Together, this atlas serves as a reference for viral infection in the upper respiratory tract and highlights the efficacy of local coordinated memory responses upon rechallenge.

49 ***INTRODUCTION***

50 As the primary passage to the lower airway, the nasal mucosa balances the complex roles
51 of olfaction, filtration and conditioning of inhaled air, and host defense. To accomplish these
52 diverse functions, the nose contains distinct anatomical structures, harbors a varied yet organized
53 cellular composition, and secretes a multitude of proteins with varied roles (Harkema et al., 2006).
54 In the face of pathogens, the nasal mucosa is thought to mount a variety of incompletely
55 understood defense mechanisms to protect against infection and limit spread to the lower
56 respiratory tract (Bosch et al., 2013). Nevertheless, many respiratory pathogens manage to infect
57 or colonize the upper airways and disseminate into the lungs, causing millions of cases of severe
58 disease, hospitalizations, and deaths annually (Clark, 2020; Roth et al., 2018; Shinya et al., 2006).

59 There is a growing appreciation for how the inflammatory state of nasal tissue affects
60 respiratory viral infection outcomes. The COVID-19 pandemic has helped accelerate research to
61 understand the roles of interferons (IFNs) in nasal protection and disease trajectory, with studies
62 highlighting the importance of sample timing and location, viral burden, and strain (Bastard et al.,
63 2022; Kim and Shin, 2021; Park and Iwasaki, 2020; Sposito et al., 2021). Single-cell analysis of
64 the human nasopharynx during SARS-CoV-2 infection showed muted IFN-responses in epithelial
65 cells from severe disease relative to mild cases (Ziegler et al., 2021). Expression of specific IFN
66 stimulated genes (ISGs) like *OAS1* associate with protection from severe COVID-19 and may
67 even drive viral mutations to overcome host protection (Wickenhagen et al., 2021). More
68 generally, evidence of a recent prior infection in children receiving a live-attenuated influenza
69 vaccine was associated with enhanced ISG signaling and lower viral shedding (Costa-Martins et
70 al., 2021). Collectively, this suggests that the present nasal state, cellular composition, and
71 antiviral signaling capacity, as informed by the cumulative history of environmental exposures,
72 may drive disease outcomes (Bastard et al., 2020; Habibi et al., 2020; Ordovas-Montanes et al.,
73 2020; Weisberg et al., 2021; Zhang et al., 2020).

74 Following viral infection or intranasal (i.n.) vaccination, immune memory in the nasal
75 mucosa can provide long-term protection both systemically and at the mucosal barrier, reducing
76 pathology and infection burden in the lower airways and elsewhere (Johnson et al., 1986; Johnson
77 Jr. et al., 1985; Rutigliano et al., 2010). Local protection is afforded by both cellular and humoral
78 immune mechanisms. For example, CD8+ tissue-resident memory (T_{RM}) cells that form following
79 upper respiratory tract influenza A virus (IAV) infection correlate with enhanced protection against
80 heterologous IAV strain rechallenge (Pizzolla et al., 2017). Protective mucosal IgA producing
81 plasma cells, and antibodies capable of neutralizing virus, can be generated in the nasal mucosa
82 following IAV, vesicular stomatitis virus, respiratory syncytial virus, and SARS-CoV-2 infections

83 (Johnson Jr. et al., 1985; Liew et al., 2023; Sterlin et al., 2021; Wellford et al., 2022; Weltzin et
84 al., 1996). Even so, respiratory infections like IAV remain epidemic and kill up to 500,000 people
85 each year (Iuliano et al., 2018).

86 To develop protective, durable, and efficacious vaccines for respiratory viruses, we must
87 reach a deeper understanding of the establishment, timing, and cooperation of tissue-scale
88 memory following natural infection (Morens et al., 2023). Immune responses to pathogens often
89 occur in stepwise fashion: recognition of pathogen-associated molecular patterns by immune
90 and/or epithelial cells leads to cytokine production that broadly activates innate immune cells that
91 in turn recruit pathogen-specific effector lymphocytes, some of which will develop into circulating
92 and tissue-resident memory cells (Iwasaki and Medzhitov, 2015). Following prior infection or
93 vaccination, however, these local circuits can be re-ordered and even inverted in the barrier
94 tissues that re-encounter infection (Kadoki et al., 2017; Kaufmann et al., 2018; Ols et al., 2020;
95 Ordovas-Montanes et al., 2020; Schenkel et al., 2014). During viral rechallenge, T_{RM} cells exhibit
96 antiviral effector functions and can act as sentinels that send antigen-specific inflammatory
97 "alarms" to local immune cells to activate multicellular anti-microbial responses at the site of
98 infection (Ariotti et al., 2014; McMaster et al., 2015; Schenkel et al., 2014; Steinbach et al., 2016).
99 In mucosal vaccination, IFNγ produced by antigen-specific T cells is sufficient to induce increased
100 inflammatory cytokine production by both distal (Bosch-Camós et al., 2022; Stary et al., 2015)
101 and local (Yao et al., 2018) antigen presenting cells, suggesting that recruited and/or tissue-
102 resident cells can contribute to rapid memory responses. Similarly, antibodies can directly
103 neutralize virus and also orchestrate a variety of antiviral effector functions through antibody Fc-
104 receptor mediated binding by NK cells, macrophages, and neutrophils (Boudreau and Alter,
105 2019). However, most of these studies to date have focused on the role of individual cell types or
106 limited interactions during a memory response.

107 Here, we present a tissue-scale single-cell RNA-sequencing (scRNA-seq) atlas of the
108 murine nasal mucosa before and during primary IAV infection and secondary rechallenge. By
109 sampling multiple regions, timepoints, and cell lineages, we develop a compositional landscape
110 of the tissue and reveal how the diversity of cell subsets and states dynamically changes in
111 response to infection and during a memory response. Primary IAV infection induced reproducible
112 stepwise shifts in cell composition starting with increased IFN-responsive neutrophil subsets
113 followed by broader antiviral/IFN-stimulated responses in epithelial, myeloid, and lymphoid
114 immune cells. Next, monocyte-derived macrophages (MDMs) accumulated along with effector
115 CD8 and CD4 T cells. Following viral resolution, early T_{RM} cells and plasmablasts are established
116 alongside increased frequencies of rare **K**rt13+ **n**asal **i**mmune-interacting **f**loor **e**pithelial (KNIIFE)

117 cells expressing genes for several ligands and receptors known to modulate immune cell activity.
118 Learning cell cluster identity in samples generated in memory and during either homologous or
119 heterologous IAV rechallenge, we demonstrate the applicability of our atlas to inform newly
120 generated data and show that the nasal memory response to IAV is accelerated and coordinated
121 compared to primary infection. Collectively, our spatial and temporal datasets enumerate and
122 characterize the diversity of cell types, states, and subsets in the murine nasal mucosa and
123 highlight those recruited and local cell subsets that exhibit memory and respond to viral infection.
124

125 ***RESULTS***

126 **Nasal mucosa infection with influenza virus and tissue processing**

127 We administered 10^4 plaque forming units (pfu) of IAV H1N1 strain PR8 i.n. to awake,
128 naïve mice in a small volume (5 µl/nostril) to restrict infection to the upper respiratory tract
129 (Klinkhammer et al., 2018; Pizzolla et al., 2017), and collected and processed nasal mucosa
130 tissue (n=3 biological samples/timepoint) by scRNA-seq at 0, 2, 5, 8, and 14 days post infection
131 (dpi; "primary") (**Figure 1A**).

132 Anatomically, the murine nasal mucosa can be divided into several distinct morphological,
133 histological, and functional tissue regions (Harkema et al., 2006). We mapped the cellular and
134 structural diversity in the naïve nasal mucosa by immunofluorescence imaging, observing broad
135 heterogeneity in epithelial, immune, and neural distribution throughout the tissue (**Figure 1B**).
136 Thus, to capture region-specific changes in cell composition and response following IAV infection,
137 we micro-dissected the tissue and separated into three different regions: (1) respiratory mucosa
138 (RM), inclusive of the nasal and maxillary turbinates, septum, and vomeronasal organ; (2)
139 olfactory mucosa (OM), inclusive of the ethmoid turbinates; and (3) the lateral nasal gland (LNG),
140 which sits underneath the RM and OM in the maxillary sinus (see **Methods**).
141

142 **Single-cell spatiotemporal atlas of primary influenza infection in the nasal mucosa**

143 Across all primary infection timepoints (0-14 dpi), regions, and replicates (n=45), we
144 collected 156,572 single-cell transcriptomes after filtering low-quality cell barcodes and hash-
145 annotated cell multiplets (**Methods**). Top-level clustering on the entire primary infection dataset
146 captured 42 clusters belonging to neural, epithelial, immune, and stromal (endothelial, fibroblast,
147 and others) cell lineages demarcated by known lineage-restricted genes (**Figures 2A and S1A**).
148 Neurons and epithelial cells comprised over half of the dataset, with immune and stromal cells
149 comprising the rest (**Figure S1B**). Major cell types were found to be distributed differently across
150 nasal regions, with enrichment of neurons, granulocytes, B cells, and hematopoietic stem cells

151 (HSCs) in the OM and more epithelial cells, fibroblasts, myeloid cells, and T & NK cells in the RM
152 (**Figures 2B and S1C**). As highly structured tissues, the turbinates in the nasal mucosa, and
153 especially the ethmoid turbinate (OM), consist of substantial pieces of bone with sizeable bone
154 marrow. Thus, the relative enrichment of specific immune cell types including HSCs and other
155 immune progenitors in the OM likely reside in this bone marrow and may directly enter the mucosa
156 and engage in pathogen defense (see **Figure 1B**). We note that succinctly depicting relative
157 proportions of the data across multiple replicates is complex; stacked bar charts like **Figure 2B**
158 show relative proportions within a cell type grouping, but do not reflect proportions within the cells
159 captured at each time point/region.
160 Sample replicates were called by demultiplexing oligo-hashtag count tables (Li et al.,
161 2020) and did not exhibit strong batch effects (**Figure S1D**). While clustering and differential
162 expression were performed on all singlets regardless of successful hash assignment, we counted
163 only those cells with annotated sample replicates for downstream compositional analyses (see
164 **Figure S1E** for assignment breakdown by cell type).
165 To delineate the diversity of cell subsets and states present in the nasal mucosa, we split
166 the dataset by cell type and conducted new clustering analyses, yielding a total of 127 clusters
167 across the dataset (**Figure S1F and Supplementary Table 1**). By counting the number of cells
168 assigned to each cluster in each sample replicate and scaling across samples by cell capture, we
169 calculated cell cluster abundances to interrogate the relationship between samples in cell
170 compositional space (see **Methods and Supplementary Table 2**). Performing principal
171 component analysis (PCA) on samples over center log-ratio (clr) transformed cell cluster
172 abundances, we saw strong separation by region (**Figure 2C**), reinforcing that the nasal mucosa
173 contains distinct regions with specific functions. Examination of the PCA loadings revealed that
174 LNG is defined by higher abundances of odorant binding protein (OBP)-expressing cells, serous
175 cells, and capillary endothelial cells (**Figure S1G**). OM has relatively more Schwann cells, HSCs,
176 and glandular, while RM is enriched for vomeronasal sensory neurons, chondrocytes, and
177 infection responsive epithelial cells. Collectively, this atlas represents a high-resolution,
178 comprehensive view of the mouse nasal mucosa enabling characterization of the dynamic
179 differences in cellular composition within and between nasal regions during infection.
180

181 **Influenza infection is largely restricted to the RM and induces reproducible changes in**
182 **cellular composition**

183 While viral, immune cell, and epithelial cell dynamics following IAV infection of the lung
184 have been partially mapped (Bouvier and Lowen, 2010; Boyd et al., 2020; Manicassamy et al.,

185 2010; Matsuoka et al., 2009; Steuerman et al., 2018), responses in the nasal mucosa are less
186 studied. Viral titers of entire nasal mucosa showed robust infection 2 dpi that waned through 8 dpi
187 and was completely cleared by 14 dpi (**Figure 2D**), while data from lungs showed sporadic spread
188 of virus from the nasal mucosa only occurring between 5 and 8 dpi (**Figure S2A**). Aligning to a
189 joint IAV and mouse genome, we also captured viral transcripts by scRNA-seq and thus could
190 identify which cells may have been infected or contained virus. Individual genes like NP and HA
191 were detected most strongly in epithelial and myeloid cells (**Figure S2B**). We calculated a
192 summative IAV unique molecular identifier (UMI) count for every single cell to assess "positivity"
193 for IAV (**Figure 2E**). Looking across time points and regions in epithelial and myeloid cells, we
194 captured low, but reproducible numbers of IAV+ cells 2, 5, and 8 dpi in the RM aligning with the
195 detectible plaque assays at these time points, but no positive cells in the OM, and only at 5 dpi in
196 the LNG (**Figures S2C-D**). Bulk RNAseq of whole RM tissue lysate better matched the plaque
197 forming assay results with higher IAV read counts than single-cell, suggesting non-cellular viral
198 RNA and/or potential loss of IAV+ cells during processing for scRNA-seq **(Figure S2E**).
199 Staining for IAV NS1 at 2 and 5 dpi confirmed that infection was largely restricted to
200 epithelial cells in the RM (**Figures 2F** and **S2F-G**) and is consistent with expression of binding
201 receptors marked by α2,3-linked sialic acid in mucous producing cells (Ibricevic et al., 2006). We
202 performed qPCR of total RM to validate an early response to infection and found robust
203 upregulation of type I and III IFNs 2 dpi, with even higher expression 5 dpi despite relatively lower
204 viral titers (**Figure 2G**). As expected, *Ifng* expression exhibited delayed kinetics peaking 8 dpi. To
205 understand the dynamics of the global IFN-induced response during infection, we calculated
206 enrichment scores for response to IFNα and IFNγ from bulk RNAseq data (**Figures 2H** and **S2H**).
207 Despite elevated levels of *Ifnb1* at 2 dpi, IFN-response signaling was not enriched until the
208 samples measured at 5 dpi; however, we cannot exclude that IFN-responses could start to occur
209 between 2 and 5 dpi given sampling limitations.
210 To understand how infection remodels each nasal region, we applied PCA to the sample
211 replicates within each region. In OM, 5 and 14 dpi samples separated from each other and the
212 other time points (**Figure S2I**). In LNG, only 14 dpi samples separated from the rest (**Figure S2J**).
213 Comparatively, PCA of RM samples showed clear separation between all timepoints in
214 chronological order across the first two PCs (**Figure 2I**) suggesting dynamic and linked responses
215 occur over the course of infection in this region. PCA loadings from RM highlight a shift in
216 composition from resting basal cells, fibroblasts, and ciliated cells in naïve mice and 2 dpi to
217 diverse activated myeloid and lymphoid clusters 5 and 8 dpi that gave way to specific
218 goblet/secretory cells, T_{RM}-like cells, and mature myeloid cells following viral resolution 14 dpi

(**Figure 2J**). Even though virus had been cleared by 14 dpi, we note that all three nasal regions reached compositions distinct from naïve mice at this timepoint.

Regional epithelial diversity in the nasal mucosa dynamically changes during IAV infection

Cellular diversity of the nasal epithelium

Having acquired high-level knowledge of how IAV infection broadly impacts the nasal mucosa, we next sought to understand the variety of epithelial cells present across the tissue and how they respond during infection as the main target of infection. Subclustering on all epithelial cells yielded 28 clusters encompassing diverse differentiation states and functions (**Figures 3A, S3A, and Supplementary Table 1**). We categorized these clusters into broader subsets including basal (*Krt5, Krt14*), ciliated (*Foxj1, Dnah5*), serous (*Ltf*, *Ccl9*), glandular (*Bpifb9b, Odam*), goblet/secretory (*Reg3g, Selenom, Scgb1c1,* and mucin-encoding genes), ionocyte (*Cftr, Coch*), tuft (*Trpm5, Il25*), and sustentacular cells (*Sec14l3, Cyp2g1*) (**Figure 3B**). In addition to known subsets, we also identified unique clusters of epithelial cells potentially specific to the nasal mucosa and present in naïve mice and throughout primary infection that separated distinctly in UMAP space: *Scgb-b27+Cck+*, *Klk1+Fxyd2+*, *Meg3+MHC-II+*, and *Krt13+Il1a+* cells. Comparison to human nasal biopsy and swab datasets (Deprez et al., 2020; Ziegler et al., 2021), readily annotated known epithelial subsets, and suggested that the *Krt13+Il1a+* cluster was squamous-like (**Figure S3B**). The other unique clusters did not map reliably to human subsets, potentially due to limitations in sampling human tissue. Epithelial clusters were differentially distributed across regions (**Figure 3C**): recently described nasal tuft cells, ionocytes, and *Dclk1+* cells (Ualiyeva et al., 2024), as well as olfactory sensory neuron supportive sustentacular cells (Brann et al., 2020), were enriched in OM, whereas serous and glandular cells were specific to LNG.

Cycling and IFN-responsive epithelial cells arise in the RM during infection

To understand the impact of IAV infection on the nasal epithelial compartment, we first determined which clusters harbored viral reads. Looking at the distribution of IAV UMIs across all epithelial clusters, we found that IAV+ cells were most prevalent in the IFN-stimulated cluster followed by cycling basal and ciliated cells (**Figure S3C**). The IFN-stimulated cluster, largely restricted to the RM, exhibited high levels of *Krt5*, a basal cell marker, but also *Cxcl17*, which in our dataset is expressed at steady state in serous cells in the LNG and some goblet/secretory subsets. Comparing cells within the IFN-stimulated cluster by presence of IAV transcripts, we found relatively higher levels of ISGs but lower expression of transcription factors *Atf3*, *Egr1*, and

253 *Junb* in IAV+ cells (**Figure S3D**). While infection was well-established at 2 dpi, IFN-stimulated
254 epithelial cells only arose at 5 dpi and made up ~20% of all RM epithelial cells 5 and 8 dpi (**Figure**
255 **3D**). The substantial detection of IAV transcripts by bulk RNA-seq (**Figure S2E**) but lack of an
256 IFN-response signature in total RM tissue at 2 dpi (**Figure 2H**) suggests that besides selective
257 loss of IAV+ cells during processing, host silencing mechanisms by IAV may contribute to the
258 measured muted IFN-response as well (Kochs et al., 2007). To understand the relative
259 contribution of type I/III and type II IFNs to the IFN-stimulated epithelial cluster, we scored these
260 cells with gene lists derived from nasal basal cells stimulated with IFNα or IFNγ in vitro (Ziegler et
261 al., 2020). While IFNα and IFNγ induce partially-overlapping ISGs, cells at 5 dpi scored higher for
262 the IFNα signature, cells at 8 dpi scored higher for the IFNγ signature (**Figure 3E**). Closer
263 exploration of genes with stronger induction following IFNα vs IFNγ stimulation confirmed the
264 sequential response timing within IFN-stimulated epithelial cells (**Figure S3E**).
265 Cycling basal cells demonstrated a similar transient increase in abundance, peaking 5 dpi
266 (**Figure 3F**). Interestingly, differential expression across timepoints revealed many ISGs were
267 upregulated in these cells 5 dpi (**Figure S3F**). Given recent work demonstrating that the epithelial
268 IFN-response can impede proliferation and tissue repair in the lower airway (Broggi et al., 2020;
269 Major et al., 2020), we leveraged our single-cell resolution to assess if individual nasal basal cells
270 co-express pathways for cell cycle and IFN-response. Gene set analysis confirmed significant
271 enrichment for both cell cycle and IFN-response pathways in cycling basal cells. Additionally, a
272 largely mutually exclusive apoptosis pathway was also significant (**Figures S3G**). Pathway
273 module scoring showed that while the IFNα response score changed over time, the G2M
274 checkpoint score was equally distributed across time points and independent of IFNα response
275 (**Figure 3G**). Thus, unlike their lower respiratory tract counterparts, nasal cycling basal cells
276 proliferate during primary infection and may concurrently support ISG expression alongside non-
277 proliferative IFN-stimulated basal cells.
278
279 *Rare unique epithelial cell subsets with lymphoid and myeloid communication potential*
280 *accumulate following viral clearance*
281 Looking at the compositional PCA, RM samples from 14 dpi separated from other
282 timepoints (**Figure 2G**). Among epithelial cells, two clusters, *Emp1*+*Ccdc3*+ basal cells and
283 *Gp2*+*Lyz2*+ goblet/secretory cells, accumulated to 9-12% of all epithelial cells following viral
284 clearance by 14 dpi (**Figure S3H**). In addition to *Gp2* and *Lyz2*, the goblet/secretory subset was
285 also enriched for *Il33*, *Muc1*, *Isg20*, and *Cd14* suggesting a potential shift in the epithelium toward
286 an antibacterial state. Additionally, two rare and transcriptionally distinct subsets of epithelial cells

287 (*Meg3*+MHC-II+ and *Krt13*+*Il1a*+), each only making up ~1% of all RM epithelial cells prior to viral
288 clearance, accumulated at 14 dpi (p=0.032 and p=0.067, respectively). The *Meg3*+MHC-II+
289 subset expressed high levels of maternally imprinted Meg genes (*Meg3*, *Rian*) alongside *Cd74*,
290 H2 class II genes, *Wnt5a*, *Cxcl12*, and *Ccl25* (**Figure 3H**). They also uniquely expressed *Fezf2*,
291 a transcription factor studied in the context of thymic self-antigen expression and immune
292 tolerance induction by thymic epithelial cells (Takaba et al., 2015), but not *Aire,* which is necessary
293 in the thymus for presentation of self-antigens. Whether these cells can promote tolerance in the
294 upper respiratory tract, like their thymic counterparts, remains to be determined.
295 The *Krt13*+*Il1a*+ subset uniquely expressed *Krt13* (93.8% expressing within cluster vs
296 0.6% expressing in other clusters), a keratin previously described on "hillock" cells in the mouse
297 trachea with undetermined functions (Montoro et al., 2018) and squamous/suprabasal cells in the
298 human nasal turbinate (Deprez et al., 2020). These *Krt13*+*Il1a*+ cells exhibited several of the
299 markers specific to tracheal hillock cells including *Lgals3*, *Ecm1,* and *Anxa1* but were not enriched
300 for *Cldn3* or club cell marker *Scgb1a1*. Unlike hillock cells, this nasal subset expressed genes for
301 several secreted and membrane bound immune cell regulatory factors including *Il1a*, *Tnf*, *Cd274*
302 (PD-L1), *Ifngr2*, and *Cxcl16* as well as secretory proteins like *Defb1*, *Muc4*, and *Muc1* (**Figure 3I**).
303 Flow cytometry confirmed the accumulation of Krt13+ cells 14 dpi (p=0.036, **Figure 3J**). Given
304 the potential for these *Krt13*+ cells to communicate with immune cells, we stained the mucosa for
305 Krt13 to understand their distribution throughout the nasal cavity. We found the strongest signal
306 for Krt13 along the nasal floor in the anterior RM (**Figure 3K**) and more distally where the nasal
307 mucosa meets the oral mucosa (**Figure S3I**). Comparing samples from naïve mice and 14 dpi,
308 we saw increased Krt13 staining and colocalization with PD-L1 in the post-infection samples
309 (**Figure 3L**). Thus, following resolution of IAV infection, rare subsets of nasal epithelial cells with
310 immune communication potential accumulate in the RM.
311
312 **Neutrophils mature and activate in the RM immediately following IAV infection**
313 Neutrophil accumulation in IAV infected lung has largely been associated with severe
314 disease and poor prognosis (Brandes et al., 2013; Johansson and Kirsebom, 2021; Tang et al.,
315 2019), but their role in the nasal viral infection is unknown. Given recent work showing a
316 relationship between increased neutrophil activation in the nose prior to RSV infection and higher
317 symptom occurrence (Habibi et al., 2020), and intrigued by the large number of neutrophils and
318 mast cells captured across the nasal mucosa (n=7,987), we investigated the transcriptional
319 programs and change in frequency of granulocytes in the nasal mucosa. Subclustering and UMAP
320 embedding revealed a continuum of granulocyte development starting with granulocyte-myeloid

321 precursor like cells (*Elane, Mpo)*, differentiating through immature states (*Camp, Mmp8, Retnlg*),
322 and ending with several clusters of mature neutrophils (*Il1b, H2-D1, Siglecf*) (**Figures 4A, S4A,**
323 **and Supplementary Table 1**). Mast cells expressing *Il6*, *Gata2*, and *Il4* were also detected in
324 small numbers. Many neutrophils originated from OM samples (**Figures 2B and S4B**) and are
325 likely present in high numbers in the bone marrow from that region. Pseudotime analysis across
326 both the OM and RM recapitulated known maturation gene expression patterns in the blood
327 (Grieshaber-Bouyer et al., 2021) and systemically (Xie et al., 2020) (**Figures 4B,C and S4C**).
328 Precursors and immature neutrophils present largely in OM samples, likely in bone marrow, may
329 give rise to activated and mature subsets in the RM that begin to accumulate in high frequencies
330 only during infection.
331 By 2 dpi, neutrophil composition in the RM transitioned into mature IFN-stimulated and
332 MHC-I-Hi states alongside an antimicrobial immature subset near the end of the pseudotime
333 development trajectory (**Figure 4D**). The accumulation of these neutrophil clusters is one of the
334 earliest changes in the RM following infection and may make up some of the earliest responses
335 to local viral molecules and/or type-I IFN, with epithelial and RM-wide IFN-stim responses not
336 arising until 5 dpi. Interestingly, the OM exhibited increased frequencies of mast cells, progenitors,
337 and cycling immature granulocytes in 2-of-3 mice at 5 dpi, likely within bone marrow, indicating
338 IAV infection may induce changes to adjacent hematopoiesis (**Figure S4D**). Thus, neutrophil
339 activation and maturation mark the earliest detectable responses using our sampling strategy in
340 the nasal mucosa to IAV infection.
341
342 **Stepwise recruitment of monocytes and differentiation of monocyte-derived macrophages**
343 **follow neutrophil activation**
344 Next, we explored heterogeneity among non-granulocyte myeloid cells (**Figure 4E, S5A**
345 **and Supplementary Table 1**) — i.e., macrophages, monocytes, and dendritic cells (DCs). We
346 captured a spectrum of macrophage (*Cd74, C1qb, Ccl4*) clusters including a *Trem2*+ subset
347 expressing *Fcrls, Il1a,* and *Pf4* (CXCL4), an innate immune recruiting subset expressing *Ccl7,*
348 *Ccl8,* and *Pf4* (CXCL4), and a small cluster of osteoclasts (*Ctsk, Mmp9*). Monocytes clustered
349 into classical (*Ly6c2, Ccr2, Chil3*) and non-classical (*Ace*, *Ear2, Itgal*) subsets (Jung et al., 2022)
350 alongside IFN-stimulated monocytes and monocyte-derived macrophages (MDMs). DCs
351 separated into distinct clusters including Langerhans-like (*Epcam, Ccl17, Ccl22*), intraepithelial
352 (*Cd103, Xcr1, Tlr3*), migratory (*Ccr7, Ccl22, Cd274)*, and a subset uniquely expressing *Cd209a*
353 (DC-SIGN), *Tnfsf9* (4-1BB), and *Klrd1*. We also captured plasmacytoid DCs (*Siglech, Irf8*; pDCs).

354 Most myeloid clusters were present in all nasal regions with some exceptions like the IFN-
355 stimulated monocytes and MDMs, which were restricted to the RM (**Figure S5B**).
356 While non-existent at baseline, upward of 30-40% of all myeloid cells belonged to these
357 antiviral monocyte and MDM clusters 5 and 8 dpi, respectively (**Figure 4F**). The appearance and
358 accumulation of monocytes and MDMs is concordant with lower frequencies of several tissue
359 macrophage clusters, likely reflecting an overall increase in the total number of myeloid cells in
360 the tissue as monocytes infiltrate from circulation. To understand the difference between the IFN-
361 stimulated monocytes and MDMs, we performed differential expression analysis between clusters
362 (**Figure 4G**). While the monocyte cluster had higher ISG expression than the MDM cluster, the
363 MDMs still had relatively high ISG expression when compared with resting tissue macrophages.
364 Notably, IFN-stimulated MDMs expressed higher levels of *Cxcl9* and *Cxcl16*, whose receptors
365 (CXCR3 and CXCR6, respectively) have been implicated in T_{RM} cell development in the lung
366 (Slütter et al., 2013; Wein et al., 2019). Comparison of response scores to IFNα and IFNγ
367 stimulation derived from in vitro macrophage cultures (Liu et al., 2012) on all IFN-stimulated
368 monocytes and MDMs showed relatively higher expression of the IFNα score at 5 dpi and the
369 IFNγ score at 8 dpi (**Figure S5C-D**), a similar pattern noted for IFN-stimulated epithelial cells
370 (**Figure 3E**).
371 The IFN-stimulated MDM cluster also had the largest number of IAV+ cells of all myeloid
372 cells (**Figure S5E**). Bystander analysis showed higher expression of some ISGs (*Isg15, Ifit3,*
373 *Rsad2*) in IAV+ myeloid cells, like IAV+ epithelial cells (**Figure S5F**). However, the small fraction
374 of IAV+ cells, compared to their bystander counterparts, had lower expression of MHC-II genes
375 and other ISGs such as *Ccl6* and *Cxcl9* suggesting reduced antigen presentation and immune
376 cell recruitment capacity. This is consistent with prior research in the lung showing that IAV
377 suppresses myeloid cell activation and maturation (Moriyama et al., 2016; Zhang et al., 2022a).
378 The rapid shift in the myeloid compartment from IFN-stimulated monocytes at 5 dpi to a
379 predominance of IFN-stimulated MDMs 3 days later (**Figure 4F**) suggested that recruited
380 monocytes differentiated into MDMs within the RM during this interval. To test this idea, we treated
381 mice with an anti-CCR2 antibody known to deplete circulating monocytes from the blood for 48
382 hours (Mack et al., 2001; Schneider et al., 2005) (**Figure S5G**). In the nasal mucosa, we stained
383 for differentiating monocytes using MHC-II, CD11c, F4/80, CD64, and an intravascular CD45 stain
384 to separate cells that had extravasated into the tissue from those in circulation (**Figure S5H**).
385 Patrolling (Ly6C+) monocytes upregulate MHC-II, in addition to F4/80 and CD64, as they
386 differentiate into MDMs. To deplete monocytes during their recruitment to the nasal mucosa
387 (between 3-7 dpi), we treated animals with anti-CCR2 from 3 to 5 dpi. Depletion led to reduced

388 frequencies of patrolling monocytes at 8 dpi (**Figures 4H**). Moreover, the proportion and number
389 of MHC-II+ patrolling monocytes (i.e., differentiating MDMs) were considerably lower (18.4% vs
390 60.1% and 2558 vs 625, respectively), suggesting that the large proportion of IFN-stim MDMs
391 measured at 8 dpi by scRNA-seq are derived from monocytes. Together, these data show that
392 IAV infection induces a large recruitment of antiviral monocytes 5 dpi that differentiate into MDMs
393 by 8 dpi in the RM.
394
395 **Antiviral NK cell responses precede transient effector T cells that are replaced by durable**
396 **T_{RM} cells following viral clearance**
397 Following the accumulation of inflammatory and chemokine secreting monocytes and
398 MDMs at 5 and 8 dpi, we anticipated a strong lymphocyte response during IAV infection. Thus,
399 we next further investigated NK and T cells, the latter of which have been shown to be essential
400 in clearing IAV infection in the lungs (Hufford et al., 2015) and nasal mucosa (Pizzolla et al., 2017).
401 Subclustering revealed NK cell subsets (*Klrb1c, Ncr1*), type 2 (*Areg, Il13*) and type 3 (*Il22, Rorc*)
402 innate lymphoid cells (ILC), $\gamma\delta$T cells (*Trdc, Cd163l1, Cd3e*), and a spectrum of $\alpha\beta$T cell subsets
403 and states including naïve/central memory CD8 (*Ccr7, Dapl1*), effector CD8 (*Gzmb, Gzmk*), T_{RM}-
404 like CD8 cells (*Itgae* [CD103]), resting CD4 (*Cd4, Tnfrsf4* [OX40]), Th1 CD4 (*Ifng, Cd200*), Th17
405 (*Cd40lg, Il17a*), and a cluster of Helios (*Ikzf2*) expressing cells (**Figures 5A, S6A, and**
406 **Supplementary Table 1**). Most T and NK cell clusters were enriched or restricted to the RM, but
407 *Ccr7*+ CD8 T cells, ILCs, and $\gamma\delta$T cells were also found in the OM and LNG (**Figure S6B**).
408 Looking at T and NK cell frequencies, we found that IFN-stimulated T and NK cells
409 accumulated 5 dpi alongside cytotoxic NK cells that remained elevated through 8 dpi (**Figure**
410 **S6C**). By 8 dpi, the T and NK cell compartment completely shifted towards effector antiviral T cell
411 subsets, with high abundances of *Gzmk*+ CD8, Th1-like *Ifng*+*Cd200*+ CD4, cycling, and Helios+
412 T cell clusters (**Figure 5B**). These effector responses were short-lived, however, and were
413 followed by increased frequencies of T_{RM} cells and resting CD4 T cells (**Figure 5C**). Flow
414 cytometry of RM tissue at matched time points confirmed an influx of CD69+CD103– activated
415 CD8 T cells at 5 and 8 dpi that receded by 14 dpi alongside the accumulation of CD69+CD103+
416 T_{RM}-like cells (**Figure 5D and S6D**). Notably, while detectable infection was largely restricted to
417 the RM, T_{RM} cells also increased in OM and LNG 14 dpi (**Figure 5E**), supporting the notion that
418 even low levels of infection can result in T_{RM} accumulation and development (Jiang et al., 2012).
419 To contextualize the T_{RM}-like cells that arise following IAV clearance, we examined two
420 recently published signatures separating resident memory from central/circulating memory. A
421 universal T_{RM} gene score (Milner et al., 2017) reasonably separated our T_{RM} cluster from effector

422 and naïve/memory CD8 T cells, but IFN-stimulated T cells also scored highly (**Figure 5F**).
423 Conversely, the T_{RM}-like cells also scored low for the associated circulating memory gene score,
424 while naïve/memory CD8 T cells scored highest (**Figure S6E**). Closer inspection of known
425 resident memory and central memory markers and transcription factors (Crowl et al., 2022)
426 confirmed restriction of *CD103* (*Itgae*) expression to our T_{RM} cluster, but *Cd69* was only highly
427 expressed in IFN-stimulated cells. *Runx3* was also most highly expressed in T_{RM}-like cells but
428 also at lower levels in effector CD8 T cells. The *Cd103*+ CD8 cluster lacked the known
429 naïve/central memory transcription factors *Klf2* and *Tcf7* (**Figure 5G**). In summary, effector T cell
430 responses in the RM 8 dpi are replaced by T_{RM}-like cells across all nasal mucosa regions following
431 viral clearance.
432
433 **IgA+ cells populate throughout the NM following viral clearance**
434 Following IAV infection, local mucosal plasma cells and activated B cells produce and
435 secrete neutralizing soluble IgA into the airways (Rossen et al., 1970; Wellford et al., 2022; Woof
436 and Mestecky, 2005). In the lungs, resident memory B cells form after primary infection and can
437 be recruited upon secondary challenge to produce additional antibodies (MacLean et al., 2022),
438 suggesting infection can lead to long term changes in both local and distal B cell subsets.
439 Clustering of B cells in the nasal mucosa (**Figures S7A-B and Supplementary Table 1**) revealed
440 mature subsets (*Ighd, Cd74*), IgG+/IgA+ early plasmablast cells (*Aicda, Jchain, Igha*), lambda-
441 chain-high expressing cells (*Iglc1, Iglc2*), nucleoside diphosphate kinase (NME) expressing cells
442 (*Nme1*, *Nme2*) and, primarily in OM, developing subsets including pro-B (*Dntt, Vpreb1, Rag1*),
443 pre-B (*Bub1b, Mki67, Sox4*), and immature B cells (*Ms4a1, Ifi30*). The preponderance of
444 precursor and developing B cell subsets in OM likely reflects bone marrow cells, whereas
445 IgG+/IgA+ cells were found at highest frequency within LNG tissue, but class-switched B cells
446 were also detectable in RM and OM (**Figure S7C**).
447 Looking at changes in cluster frequency over the course of IAV infection, we found that
448 pro-B and pre-B cells collectively comprised up to 80-90% of all B cells in the OM 5 dpi increasing
449 from 5-15% at baseline, suggesting that IAV infection may induce local B cell proliferation and
450 differentiation in the bone marrow following infection and/or egress of mature B cells from this
451 region (**Figure S7D**). This increase in B cell precursor frequency in OM 5 dpi paralleled that of
452 granulocyte precursors (**Figure S4D**), supporting the notion of activation in nasal bone marrow.
453 By 14 dpi, IgG+/IgA+ early plasmablast cells were detected in the RM in all three replicate
454 samples. However, their recovery was more variable in OM and LNG samples, which could be
455 due to biological variability and/or inconsistent cell capture. Flow cytometry staining for

456 intracellular IgA confirmed the increase of IgA+ cells in both RM and LNG (**Figure S7E**) at 14 dpi.
457 Moreover, imaging of the RM and LNG at 30 dpi confirmed the presence of IgA+ cells in both
458 regions following infection (**Figure S7F**). Thus, B cells may undergo proliferative development
459 during acute IAV infection and IgA+ plasmablasts accumulate in the RM and LNG following
460 clearance.
461
462 **Proportionality guided cell-cell communication analysis highlights the CXCL16-CXCR6**
463 **signaling axis in effector and memory T cell responses**
464 To understand how compositional changes in the tissue during primary infection may be
465 coordinated across multiple cell subsets, we next characterized relationships between pairs of
466 cell clusters over time using our compositional data. We employed proportionality analysis (Lovell
467 et al., 2015), an alternative to correlation that avoids intra-sample abundance dependence
468 present in compositional data (Quinn et al., 2018), to find cell clusters with significantly similar
469 abundance trajectories (see **Methods**). Given that the RM was the major site of infection and
470 showed temporally structured changes in cell composition over time (**Figure 2I**), we applied our
471 proportionality analysis to all samples from this region. We discovered a highly structured
472 proportionality landscape with 101 significantly proportional cluster pairs (FDR < 0.05) (**Figures**
473 **6A and S8A**). To understand coordination among larger groups of cell clusters, we built a network
474 of all significantly proportional cluster pairs (**Figure S8B**). The network revealed larger groups of
475 proportional responses made up of clusters from several different cell types and smaller and
476 single-pair groups with 1-2 contributing cell types. Next, to further characterize the coordination
477 among immune cells and between immune and epithelial cells, we investigated subsets of
478 clusters with high proportionalities by cell-cell communication analysis.
479
480 *IFN-stimulated MDMs – Gzmk+ CD8 T cells – Ifng+Cd200+ CD4 T cells*
481 The strongest proportionality was observed among highly networked IFN-stimulated
482 clusters and effector T cell clusters (**Figure 6B**). Given the strong myeloid and T cell responses
483 8 dpi and the possibility that activated MDMs may function as APCs, alongside DCs, within the
484 nasal mucosa, we focused on the relationship between the IFN-stimulated MDM, *Gzmk*+ CD8 T
485 cell, and *Ifng*+*Cd200*+ CD4 T cell clusters. Plotting abundance values confirmed synchronous
486 trajectories of these three clusters with transient accumulation starting 5 dpi, peaking at 8 dpi, and
487 waning by 14 dpi (**Figure 6C**). We next assessed cell-cell communication potential using
488 NICHES, an approach that finds single-cell pairs with multiplicative high expression of known
489 interacting ligands and receptors (Raredon et al., 2023). Differential ligand-receptor expression

490 between groups of cell-pairs was then used to identify interactions specific to pairs of clusters
491 (see **Methods** and **Supplementary Table 3**). Applied to cells from these three clusters at 8 dpi,
492 we found several predicted, literature supported, interactions between the MDM cluster and both
493 effector T cell clusters including *Cd274–Pdcd1* (PD-L1–PD-1), *Cd86–Cd28*, *Cxcl9/10–Cxcr3,* and
494 *Cxcl16–Cxcr6* (**Figure 6D**). Imaging confirmed the spatial proximity of CD8 T cells and
495 MDMs/DCs RM 8 dpi (**Figure 6E**).
496
497 *Cd103+ DCs – Dusp2+Icam1+ mature neutrophils – Gp2+Lyz2+ goblet/secretory cells*
498 The second largest networked group included various myeloid, granulocyte, and epithelial
499 cell clusters. Intrigued by the inclusion of the late arising Gp2+Lyz2+ goblet/secretory cell cluster
500 (**Figure S3G**), we took a closer look at this cluster and the two clusters most proportional with it:
501 *Cd103*+ DCs and *Dusp2*+*Icam1*+ mature neutrophils. Plotting cluster abundances confirmed that
502 all three clusters peaked following viral clearance 14 dpi (**Figure S8C**). Closer inspection of
503 differentially expressed ligand-receptor pairs revealed potential pro-inflammatory signaling by
504 Gp2+Lyz2+ Gob/Sec cells to mature neutrophils via *Sftpd–Sirpa*, which blocks Cd47 binding
505 (Gardai et al., 2003), *Cirbp–Trem1* which has been shown to occur in sepsis (Denning et al.,
506 2020), and *Tgfb2–Tgfbr1*. DC–neutrophil interactions included *Ccl2–Ccr1* and *Il18–Il18rap*
507 suggesting mutual immune recruitment/homeostasis (**Figure S8D**). These interactions suggest
508 that late arising *Gp2*+*Lyz2*+ goblet/secretory cells may recruit and regulate *Cd103*+ DCs and
509 mature neutrophils in the RM following viral clearance.
510
511 *Krt13+Il1a+ epithelial cells express Cxcl16 and increase when T_{RM}-like cells accumulate*
512 Like IFN-stim MDMs producing *Cxcl16* 8 dpi in concert with abundant *Cxcr6* expressing
513 effector CD8 and CD4 T cells, the late arising *Krt13*+*Il1a*+ epithelial cell subset expressed *Cxcl16*
514 alongside increasing frequencies of *Cxcr6*+ T_{RM} and CD4 T cells 14 dpi (**Figures 6F-G**). Although
515 not significantly proportional over all time points (ρ = 0.53, 0.32, 0.77), we applied cell-cell
516 communication analysis to cells from 14 dpi in these three clusters given the role of CXCL16–
517 CXCR6 signaling in T_{RM} localization in the lower airways (Morgan et al., 2008; Wein et al., 2019).
518 In addition to discovering the *Cxcl16-Cxcr6* interaction, the analysis also captured additional
519 interactions like *Cd274–Pdcd1*, *Tnf–Tnfsrsf1b*, *Il18–Cd48*, *Alcam–Cd6*, and *Il16–Cd9* (**Figure**
520 **6H**). RNAscope of the nasal floor in a naïve mouse and 14 dpi mouse confirmed expression of
521 *Cd274* (PD-L1) and *Cxcl16* by *Krt13*+ cells in the vicinity of cells expressing *Cxcr6* (**Figure 6I-J**).
522 Comparison between time points showed higher relative abundance of Cxcl16 transcripts within
523 *Krt13*+ regions at 14 dpi compared to naïve samples (**Figures 6K and S8E**). Considering the

524 transcriptional programming and localization of these cells, we propose the name ***K**rt13*+ **n**asal
525 **i**mmune-**i**nteracting **f**loor **e**pithelial (KNIIFE) cells. Notably, KNIIFE cells are a fraction of many
526 cells on the nasal floor expressing *Cxcl16* at 14 dpi, suggesting that this region of the nasal
527 mucosa may be important in instructing T_{RM} cells following viral clearance and/or tissue damage.
528 In summary, proportionality analysis coupled with cell-cell communication approaches
529 reveal temporally synced cell cluster abundance changes over the course of primary infection and
530 highlight potential cell-cell interactions contributing to T cell function and residual inflammation
531 following viral clearance.
532
533 **Evaluating the reference capacity of the nasal mucosa atlas to learn compositions of**
534 **additional scRNA-seq datasets**
535 To assess the ability of our primary IAV infection atlas to contextualize and analyze
536 additional scRNA-seq data generated from murine nasal mucosa, we leveraged the replicate
537 structure of our dataset to test label transfer methods. Separating one RM replicate from each
538 timepoint as a query set, we compared Seurat's built-in weighted nearest neighbors method (Hao
539 et al., 2021) to the generative model approach used in single-cell Annotation using Variational
540 Inference (scANVI) (Xu et al., 2021). First trying cluster annotation on the entire RM query dataset,
541 we found poor accuracy in assigning correct cluster identity in both methods and several clusters
542 were completely lost in the predicted annotations (**Figure S9A**). Since the primary infection atlas
543 clusters were found following multiple rounds of clustering, we next applied the same stepwise
544 approach for label transfer: assign a cell type label and then split into cell types for cluster label
545 predictions (**Figure 7A**). Using this stepwise approach, we correctly labeled 99.66% cell types
546 using Seurat and 99.27% using scANVI (**Figure S9B**). Cluster identity calling, however, was more
547 accurate in Seurat with 89.11-95.19% of cells correctly annotated across cell types, whereas
548 scANVI had 69.33-92.31% properly labeled (**Figure S9C**). Moving forward with Seurat given its
549 superior predictions, we repeated the analysis two more times using the other sets of replicates
550 as the query dataset, finding robust reproducibility across models for cell type and cluster calling
551 (**Figure S9D-E)**. Finally, we validated the output by calculating cell cluster abundances using the
552 predicted cell cluster labels and projecting these "query" replicates into the primary infection RM
553 compositional PCA. Remarkably, the query replicates aligned very closely to their real sample
554 replicate counterparts in compositional space (**Figure S9F**). Thus, we validated a label transfer
555 approach to learn cell cluster identities and cellular composition of new scRNA-seq data using
556 our primary infection atlas as a reference.
557

558 **IAV rechallenge is characterized by accelerated and concurrent myeloid and lymphocyte**
559 **memory responses**

560 Having developed a tissue-scale response timeline of acute IAV infection in the nasal
561 mucosa, we next asked how strain matched and unmatched induced memory responses differ
562 from primary infection on cluster and compositional levels. After priming mice with IAV PR8
563 infection, we rechallenged 60 dpi with either the same virus or IAV X31, a H3N2 strain (**Figure**
564 **7B**). In the PR8→PR8 arm, both antibody and T-cell mediated mechanisms of protection will
565 occur; in the PR8→X31 arm, however, antibodies from the primary infection will fail to neutralize
566 IAV, but T cells will still exhibit memory responses (Pizzolla et al., 2017). Sampling RM prior to
567 rechallenge at 60 dpi, and 2- and 5-days post rechallenge (dprc), we applied our label transfer
568 approach — using the primary infection data as a reference — to annotate an additional 76,159
569 cells with cluster labels derived from primary infection (**Figures 7A**). All cell types present in the
570 primary infection dataset were captured in the rechallenge samples and UMAP projection showed
571 strong overlap between the datasets (**Figure S10A,B**). Plaque assays following PR8 rechallenge
572 detected infectious virus in 1-of-5 mice in nasal mucosa, and in 0-of-6 mice in lung at 2 dprc, and
573 none at 5 dprc, suggesting immediate control of infection or baseline resistance (**Figure S10C**).

574 Inspection of cell type frequencies in rechallenge demonstrated substantial accumulation
575 of immune cells in both the homologous and heterologous settings. Even with neutralizing
576 antibody mediated protection in the PR8 challenge and nearly undetectable viral titers, we
577 measured increased proportions of granulocytes, T & NK cells, and B cells following rechallenge
578 (**Figures 7C and S10D**). Following X31 challenge, T & NK cell frequencies increased even higher
579 than following PR8 challenge alongside a substantial but transient accumulation of myeloid cells,
580 supporting a bigger role for T cell-mediated responses in the absence of antibodies. Since plasma
581 cells were not captured in our primary infection time course and thus could not be identified by
582 label transfer, we re-clustered all the B cells in our acute and memory dataset. We readily resolved
583 a small cluster (n = 75 cells) of plasma cells expressing *Slpi*, *Jchain*, *Igha,* and *Xbp1* present at
584 low, variable frequencies at 60 dpi and during rechallenge (**Figures S10E,F**).

585 Following annotation, we compared changes in cluster abundance over time between the
586 primary and secondary responses to IAV infection (**Figures 7D and S10G**). Like primary infection,
587 the IFN-Stim neutrophil subset accumulated immediately and maintained elevated levels through
588 5 dprc. Interestingly, in homologous rechallenge IFN-stimulated MDMs rapidly accumulated while
589 monocytes only slightly increased; in heterologous rechallenge, both increased substantially.
590 Given the total proportion of myeloid cells in the dataset was similar between 60 dpi, 2 dprc, and
591 5 dprc following PR8, these data suggest that MDMs already inside the RM prior to homologous

592 rechallenge quickly responded. Effector Th1 CD4 T cells were also elevated 2 dprc, but effector
593 CD8 T and T_{RM} cells were slower to accumulate. Cycling basal cells showed no change in
594 abundance following rechallenge regardless of rechallenge strain, and the increase in IFN-
595 responsive epithelial cells was also stunted. Notably, both the *Meg3+MHC-II+* subset and KNIIFE
596 cells that arose following viral clearance in primary infection remained at low levels throughout
597 rechallenge. While we do not yet understand whether their roles may be restricted to resolving
598 primary infection, there may be a necessary inflammation threshold for their expansion, or they
599 may take longer to increase in frequency than the relatively early sampling timepoints post re-
600 challenge. In summary, both PR8 and X31 rechallenge induced the rapid accumulation of several
601 anti-viral myeloid and T cell subsets and states despite little detectible virus, with even greater
602 induction following heterologous challenge.

603 To understand if cell state and the quality of antiviral effector responses differs depending
604 on prior exposure and viral strain, we performed differential expression analysis within cell
605 clusters across primary infection, PR8, and X31 rechallenge (**Figure 7E** and **Supplementary**
606 **Table 4**). IFN-stimulated MDMs at 2 dprc in both PR8 and X31 rechallenge compared to 8 dpi
607 had lower expression of *Lgmn, Cd72, and Ccr1*, but higher levels of *Tnfaip2*, *Lars2*, or *Parp14*.
608 *Ifng+Cd200+* CD4 T cells may become more prone to cell death during a memory response, with
609 lower levels of *Tnfrsf4* (OX40), *Icos*, and *Cd200*. However, they expressed higher levels of *Itga1*,
610 which has been shown to mark a subset of CD4 T cells that rapidly secrete IFN-γ in the airways
611 following IAV infection (Chapman and Topham, 2010). Compared to 8 dpi, *Gzmk+* CD8 T cells at
612 5 dprc in both PR8 and X31 rechallenge exhibited reduced expression of cytotoxic and activation
613 genes, but higher levels of cell survival genes *Birc5* and *Selenoh*, and histone *H2afv*, suggesting
614 induction of epigenetic modifications. During rechallenge, Cd103+ CD8 T cells expressed lower
615 levels of *Id2*, *Cxcr6*, and *Ccr2* relative to 14 dpi, when these cells were likely just starting exhibit
616 a T_{RM} phenotype; during rechallenge, expression of *Xcl1*, *Bcl2*, and *Klf2* was moderately, but
617 significantly increased.

618 While changes in abundance or gene expression on an individual cell subset/state level
619 highlight specific differences between primary and secondary responses, we sought to
620 understand how the collective RM tissue-scale response differs. To contextualize on the
621 compositional level, we projected the memory and rechallenge sample replicates into the
622 previously derived compositional PC space for RM in primary infection (**Figure 7F**). The RM 60
623 dpi samples were separated from naïve samples and most resembled 2 dpi, suggesting that even
624 though IAV was cleared by 14 dpi, the nasal mucosa sustained significant changes in
625 composition. For both memory arms, the 2 dprc time point recapitulated the variance described

626 by PC1, with X31 rechallenge samples moving further negative in PC1 and overlapping 8 dpi. No
627 significant shift along PC2, unlike in primary infection, suggests increases in effector immune
628 responses occur upon rechallenge but not broad antiviral activation across all cell types like those
629 seen 5 dpi (i.e., IFN-Stim clusters) (**Figure 2H**). Notably, by 5 dprc in the PR8. rechallenge, the
630 tissue had almost returned to "memory baseline" at 60 dpi in PC-space, indicating that responses
631 had already largely resolved; however, in the X31 challenge, a high level of immune infiltration is
632 still taking place at 5 dprc. To assess variation between the primary infection distinct secondary
633 response arms, we re-ran PCA with abundances from all timepoints, finding some separation
634 between experiments, potentially arising from variation in the primary infection (**Figure S10H**).
635 Nevertheless, infection in the naïve setting and both rechallenge paradigms resulted in a
636 concerted and parallel directional shift in compositional PC space, supporting the conclusions of
637 induced effector myeloid and T cell clusters from the projected PCA. Notably, PC4 captured the
638 aspects unique to a "optimal" memory response, with increased abundances of several B cell
639 clusters during homologous rechallenge (**Figure S10I**).
640 To quantify the overall difference between timepoints, we calculated compositional
641 Aitchison distances between all pairs of sample replicates (**Methods**). In primary infection, RM
642 increasingly separated from the naïve state up through 8 dpi but then became closer as infection
643 is resolved (**Figure 7G**). Corroborating the PCA, the nasal mucosa 60 dpi was still distinct from
644 its naïve state. Upon rechallenge with PR8, RM also separated from 60 dpi; however, the extent
645 of that difference (MD=3.96) was less than between naïve and 5 dpi (MD=7.00) and 8 dpi
646 (MD=7.40) indicating that the memory response to the same IAV strain was more succinct (**Figure**
647 **7H**). In comparison, X31 rechallenge led to the largest distance increase (MD=9.18), highlighting
648 the massive accumulation of immune cells induced without antibody-mediated protection (**Figure**
649 **7I)**. Comparing primary infection timepoints with peak memory response, each primary infection
650 timepoint was substantially distinct from 2 dprc, suggesting that prior infection rewired the RM
651 response to IAV infection (**Figure S10J**). Summarizing the primary and secondary responses to
652 infection described here, we present a timeline of the key immune and epithelial cell responses
653 during IAV infection and rechallenge illustrating that many of the stepwise changes seen in
654 primary infection occur in a more coordinated and accelerated fashion in memory (**Figure 7J**).
655
656 ***DISCUSSION***
657 Comprehensively understanding airway mucosal immunity is an urgent unmet need in the
658 face of emerging and recurring respiratory pathogens (Lavelle and Ward, 2022; Morens et al.,
659 2023; Roth et al., 2018; Russell et al., 2020). In particular, the nasal mucosa is at the forefront of

660 mammalian host responses to airborne pathogens and functions as both an entry site and the
661 primary barrier for infections of the respiratory tract. Consequently, the nasal mucosa is thought
662 to be the site of initial engagement of respiratory viruses to generate both local T cell memory
663 (Pizzolla et al., 2017) and neutralizing antibodies (Liew et al., 2023; Sterlin et al., 2021; Wellford
664 et al., 2022; Weltzin et al., 1996). Determining how these responses occur following primary
665 infection, and how immune and non-immune cells in the nasal mucosa contribute to viral
666 clearance and subsequent memory, is critical to inform the design of next-generation nasal
667 vaccines and therapeutics.

668 Here, we present a longitudinal, multi-region, scRNA-seq atlas of the murine nasal
669 mucosa during primary and secondary IAV infection. Cataloguing the distribution and temporal
670 dynamics of the diverse cell types, subsets, and states present, we develop and apply a
671 compositional framework to understand tissue-scale changes occurring throughout primary and
672 memory responses to viral infection. Neutrophil activation responses following infection precede
673 broader type I/III IFN-stimulated responses in epithelial, myeloid, and lymphoid cells. By 8 dpi,
674 effector CD8 and *Ifng*+ CD4 T cell subsets accumulate alongside recently differentiated MDMs.
675 Following viral clearance at 14 dpi, T_{RM}-like cells and IgG+/IgA+ B cells appear in the nasal
676 mucosa, which has achieved distinct cellular composition from the naïve state with these adaptive
677 immune subsets being sustained until 60 dpi. Careful investigation of the epithelial cell
678 compartment also revealed a rare, previously undescribed KNIIFE cell subset. We validate and
679 localize the presence and accumulation of these cells, provide evidence for their interaction with
680 *Cxcr6*-expressing lymphocytes, and show co-expression of *Krt13*, *Cd274* (PD-L1), and *Cxcl16* on
681 the nasal floor following viral clearance. Employing the primary infection atlas to annotate and
682 interpret new secondary infection samples using both homologous and heterologous IAV strains
683 showed that rechallenge induces surprisingly widespread yet coordinated and accelerated
684 changes to cellular composition. We identify accelerated neutrophil, macrophage, and T cell
685 responses in memory with a reduced burden on epithelial cells to express the joint interferon and
686 proliferative response programs of primary infection.

687 The nasal mucosa consists of a multi-faceted epithelium that exhibits diverse responses
688 to IAV infection. Basal cells in the nasal mucosa give rise to epithelial cells reminiscent of
689 pseudostratified epithelium found in the trachea (Davis and Wypych, 2021), but we and others
690 have also captured several additional epithelial cell subsets not found in other parts of the airway.
691 Our atlas validates recent work in mice describing sustentacular cells, ionocytes, nasal tuft cells,
692 and serous cells (Brann et al., 2020; Ualiyeva et al., 2024). Moreover, we describe for the first
693 time several clusters of epithelial cells with undetermined function: (1) *Scgb-b27*+*Cck*+, (2)

694 *Meg3*+MHC-II+, (3) *Klk1+Fxyd2*+, and (4) KNIIFE cells. Except for the *Scgb-b27+Cck*+ cluster,
695 the remaining previously undescribed clusters all exist at low frequencies (< 1% of all epithelial
696 cells) in naïve mice and may have been missed in experiments without sufficient cell numbers or
697 utilized cell sorting.

698 The viral signaling and proliferative capacities of epithelial cells associate with COVID-19
699 disease trajectory (Sposito et al., 2021; Ziegler et al., 2021). Our data confirm that transient IFN-
700 responsive epithelial cell subsets, including cycling basal cells, arise in the nasal mucosa during
701 IAV infection. At 5 dpi, type I/III IFNs drive the response, while at 8 dpi, IFNγ levels are increased
702 alongside Th1-like cells. At 5 dpi, nasal basal cells co-expressed cell cycle and IFN-response
703 programs, which have been previously described as non-compatible in lungs (Broggi et al., 2020;
704 Major et al., 2020). Given the diverse roles of nasal epithelial cells and the need to protect
705 olfactory sensory neurons (Dumm et al., 2020), nasal basal cells may be more tolerant of IFN-
706 response signaling during proliferation than basal cells in the lower airways. Notably, epithelial
707 IFN-induced responses were significantly reduced upon rechallenge regardless of IAV strain. This
708 difference could reflect several non-exclusive mechanisms during recall, including an overall
709 reduction or shortening in IFN production or signaling, lower viral load, or a potential tolerized
710 basal cell state. Airway basal cells can develop transcriptional memory in vitro (Adamson et al.,
711 2022), but whether primary infection can confer durable memory to viral immunity, as has been
712 seen for allergic inflammation (Ordovas-Montanes et al., 2018), requires further investigation.

713 In addition to epithelial responses, IAV infection also precipitated a highly dynamic,
714 stepwise response by immune cells that was initially dominated by myeloid subsets. Specifically,
715 we observed a substantial early influx of neutrophils followed by monocytes responding to type
716 I/III IFNs that then differentiated into MDMs concurrent with the arrival of effector T cells
717 expressing IFNγ. The evidence for both resident (Yao et al., 2018) and recruited (Aegerter et al.,
718 2020) macrophages in the lungs to engage in memory responses suggests that a similar
719 phenomenon may occur in the nasal mucosa. After depleting circulating monocytes during acute
720 infection, MDM formation was markedly reduced, indicating that the majority of nasal MDMs at 8
721 dpi differentiated from newly recruited monocytes. Interestingly, during homologous memory
722 response MDMs, but not monocytes, increased in abundance 2 dprc even though overall myeloid
723 frequencies remained unchanged, suggesting that either recruited MDMs replaced local myeloid
724 cells or MDMs already present in the tissue expanded to exert antiviral effector functions. If the
725 latter, understanding the mechanisms by which enhanced myeloid function is maintained and
726 recalled in the nasal mucosa could yield a new avenue for designing improved mucosal vaccines
727 (Iijima and Iwasaki, 2014).

728 The role of adaptive immune responses to IAV infection have been well described in the
729 lower respiratory tract (Chapman and Topham, 2010; Krammer, 2019; McMaster et al., 2015;
730 Onodera et al., 2012; Slütter et al., 2013; Wein et al., 2019), but their dynamics and quality in the
731 nasal mucosa are less understood. Antibody-mediated immunity following primary and secondary
732 IAV infection has been described (Chen et al., 2018) and falls outside the scope of the present
733 study. Antibody-producing B cell response dynamics were variable in our model with sizeable
734 frequencies of IgA+ B cells detected in 1- or 2-of-3 mice at 14 dpi and low numbers of plasma
735 cells at 60 dpi during rechallenge. Flow cytometry validated increased frequencies of IgA+ cells
736 in RM and LNG at 14 dpi. Wellford et al., recently showed in an influenza B model that the OM
737 requires mucosa resident plasma cells to prevent transmission to the brain; the RM, alternatively,
738 can receive neutralizing antibodies from both serum and local plasma cells (Wellford et al., 2022).
739 To what extent local nasal plasma cell derived IgG and IgA play roles in stymying infection during
740 rechallenge, and whether non-neutralizing antibody functions help activate other immune subsets
741 (e.g., Fc receptor mediated signaling), must be further explored.
742 IAV infection of the nasal mucosa resulted in classical T cell responses with both antiviral
743 effector CD8 T cells expressing cytotoxic genes and Th1 CD4 T cells expressing *Ifng* and *Tnfrsf4*
744 (OX40) arising at 8 dpi. Proportionality analysis revealed their coordination with an influx of IFN-
745 Stim MDMs expressing *Cxcl9* and *Cxcl16*, and NICHES predicted several modes of
746 communication between all three clusters, suggesting MDMs, alongside DCs, may provide
747 activation signals for T cells in the nasal mucosa. While infectious titers waned between 2 and 8
748 dpi, effector T cell responses likely played a critical role in completely extinguishing IAV infection
749 by 14 dpi. Finding upward of ~50% of all T and NK cells by 14 dpi belonged to the T_{RM}-like cluster
750 in the RM tissue, we validate their presence and phenotype in the nasal cavity following IAV
751 infection (Pizzolla et al., 2017; Wiley et al., 2001). Unlike in the lung where T_{RM} cells quickly wane
752 following infection (Slütter et al., 2017), our data demonstrate robust frequencies out to 60 dpi
753 that are further amplified during rechallenge; moreover, in addition to the RM, we find T_{RM} in OM
754 and LNG tissue, where virus is only detected at low levels or not at all. While T_{RM} contribute to an
755 effective memory response upon rechallenge (Ariotti et al., 2014; McMaster et al., 2015; Schenkel
756 et al., 2014; Steinbach et al., 2016), differential expression across primary and rechallenge
757 responses of the *Cd103*+ CD8 T cell cluster in our dataset showed few significant gene
758 expression differences between time points; moreover, their relative proportion only increased by
759 ~2-3x over levels at 60 dpi depending on the strain of IAV used. Together, T cell accumulation
760 was substantially higher in a heterologous rechallenge setting compared to the matched strain,
761 suggesting potential compensatory mechanisms of protection without functional neutralizing

762 antibodies. Given recent work highlighting the importance of T_{RM} in mitigating nasal viral infections
763 and transmission (Mao et al., 2022; Pizzolla et al., 2017; Uddbäck et al., 2024), understanding
764 which cell subsets and signals establish, maintain, and expand the T_{RM} niche could help guide
765 mucosal vaccine strategies with heterotypic protection.

766 Following viral clearance, subsets of epithelial cells with potential immune signaling and
767 inflammatory regulation capacity substantially increased in abundance. In addition to a large
768 cluster of goblet/secretory cells with predicted DC/neutrophil communication ability, we also
769 discovered a subset of epithelial cells uniquely expressing *Krt13* and *Krt6a* in the nasal mucosa,
770 which we identify as ***K**rt13*+ **n**asal **i**mmune-**i**nteracting **f**loor **e**pithelial (KNIIFE) cells.
771 Phenotypically, KNIIFE cells were reminiscent of the recently described "hillock" cells in the
772 trachea expressing *Krt13, Ecm1*, and *Lgals3* (Montoro et al., 2018) and squamous cells in human
773 nasal swabs and biopsies (Deprez et al., 2020; Ziegler et al., 2021). However, KNIIFE cells also
774 expressed several genes often found in macrophages including *Cd274* (PD-L1), *Ifngr2*, *Tnf*, and
775 *Cxcl16*. This cluster was present at low levels throughout infection until expanding 14 dpi and
776 remained stable during rechallenge. At 14 dpi, we measured *Krt13* and *Cxcl16* co-expression in
777 situ nearby *Cxcr6* expressing cells, especially along the nasal floor. These results raise the
778 possibility that KNIIFE cells, by providing a source for CXCL16 beyond that expressed by myeloid
779 cells, may contribute to the establishment and/or maintenance of the resident memory T cell pool
780 in the nasal mucosa, as has been suggested for this chemokine pathway in other tissues (Clark
781 et al., 2006; Heim et al., 2023; Morgan et al., 2008; Tse et al., 2014; Wein et al., 2019). We use
782 "KNIIFE" as a convenient acronym for these cells, but their specific functions must still be
783 elucidated. The enrichment of KNIIFE cells along nasal floor and below the vomeronasal organ
784 prompts the question of whether these cells interact with particles or irritants just entering or
785 settling in the nose and play a regulatory role in tissue tolerance and/or immunity.

786 Compositional scRNA-seq analyses are becoming more common to discern differences
787 between disease trajectories (Ordovas-Montanes et al., 2018; Smillie et al., 2019; Zheng et al.,
788 2021), treatment groups (Darrah et al., 2020; Zhang et al., 2022b), and/or species (Chen et al.,
789 2022; Li et al., 2022). Current tools focus on identifying specific clusters or gene programs that
790 are compositionally distinct between groups (Büttner et al., 2021; Cao et al., 2019; Dann et al.,
791 2022). However, the power of compositional scRNA-seq data lies in its structure; namely, singular
792 changes in composition cannot be independent and must correspond with mutual changes in
793 other clusters/programs. Leveraging the biological replicates and multiple timepoints present in
794 our atlas, we utilized straightforward tools for compositional analysis adapted from microbiome
795 research (Gloor et al., 2017; Lin and Peddada, 2020; Quinn et al., 2018) to understand tissue-

796 scale changes within the nasal mucosa throughout IAV infection. PCA of center-log ratio
797 transformed cell cluster abundances across sample replicates separated nasal regions and
798 depicted structured stepwise changes in epithelial and immune cell subsets throughout infection
799 trajectory. Proportionality analysis, which avoids the spurious associations present in Pearson
800 correlation applied to compositional data (Lovell et al., 2015), revealed pairs and groups of
801 clusters with significantly similar compositional trajectories (e.g., IFN-stimulated MDMs and
802 effector CD4 and CD8 T cells) and can be readily applied to discover similarities across various
803 metadata. We note that proportionality will highlight those potential interactions where subsets
804 are changing together in relative abundance. Thus, any interactions that occur between subsets
805 where only changes in gene expression occur may be overlooked by this approach, but newer
806 tools are in development to assess prior interaction potential based on gene expression (Li et al.,
807 2023). Finally, metrics like Aitchison distance (Aitchison et al., 2000) capture holistic changes in
808 tissue-scale cellular composition and support standard tests for differences between group means
809 (e.g., Welch's ANOVA) to assess global similarity and compositional distance traveled by a tissue.
810 Applied to our datasets, the RM "travels" less during an "optimal" memory response to IAV than
811 during primary infection, suggesting prior infection induces a coordination of responses that were
812 previously unsynchronized. We propose that these approaches for analyzing scRNA-seq data
813 constitute a new framework for understanding and summarizing whole tissue- and biopsy-scale
814 changes in cellular composition at high resolution in health, disease, and/or under perturbation.
815 Collectively, our murine nasal mucosa atlas of primary IAV infection longitudinally
816 catalogues the cell types, subsets, and states present throughout distinct nasal regions. We
817 demonstrate the utility of our dataset to serve as an annotation reference for newly generated
818 scRNA-seq datasets and apply it to understand how the response to infection in the RM differs
819 during memory recall following distinct IAV rechallenges. These findings will help contextualize
820 temporal studies of the nose in humans with more complex exposure histories and highlight key
821 immune and epithelial cell responses to recapitulate in future nasal vaccines and therapeutics to
822 drive increased synchronicity in nasal memory responses.
823
824 **Limitations of the study**
825 First, we acknowledge that cluster abundance-based compositional analyses are inherently
826 dependent on how clustering was performed, and thus implicitly incorporates, to some degree,
827 operator bias. While we believe our approach to be as impartial as possible through use of
828 iterative clustering, it will be imperative to implement robust, reproducible clustering analyses (Hu
829 et al., 2019; Patterson-Cross et al., 2021; Zheng et al., 2023) prior to compositional analysis

830 moving forward. Partial labeling of cells by hashing antibodies may also have obscured changes
831 in composition over time. Second, detection of IAV transcripts by scRNA-seq was limited. Other
832 studies have included spike-in primers to facilitate additional capture of viral nucleic acids
833 (Ratnasiri et al., 2023); it is possible that we were not sufficiently sensitive to IAV transcripts
834 without these spike-in primers. Also, cells productively infected with virus may not be sufficiently
835 viable through our tissue processing pipeline, as suggested by the viral reads detected by bulk
836 RNA-seq from tissue lysate, leading to artificially low numbers of cells containing IAV reads. Third,
837 to increase the relative proportion of non-epithelial cells in our scRNA-seq dataset, we performed
838 a partial EpCAM depletion using magnetic beads. This decision was made following experiments
839 comparing this approach to un-depleted RM tissue in naïve mice; we found that while depletion
840 reduced the relative abundance of some epithelial cell clusters, it did not result in the complete
841 loss of any cluster. Thus, the cellular compositions throughout the study represent the nasal
842 mucosa tissue after both dissociation and epithelial cell depletion and, therefore, do not reflect
843 the true frequencies of cell types within intact nasal mucosa. Nevertheless, our atlas can still be
844 used to assign cell cluster labels to new datasets where epithelial cells have not been depleted
845 and could inform spatial transcriptomics approaches to derive more accurate cell abundances in
846 vivo. While this dataset represents the largest scRNA-seq atlas of the murine nasal mucosa to
847 date, we may still be under sampling this complex tissue. Indeed, spatial transcriptomics and/or
848 multiplexed immunofluorescence approaches will help validate the spatial organization and
849 quantification of cell clusters defined here; however, given the complexity of the nasal mucosa
850 and difficulty in sectioning through the nasal bone, further work will need to be done to validate,
851 adapt and refine imaging protocols for this unique tissue. Additional experiments to test how other
852 respiratory pathogens and vaccination strategies impact the composition and timing of responses
853 in the nasal mucosa to IAV challenge are warranted (Rutigliano et al., 2010).
854

855 ***Acknowledgements***

856 We would like to thank members of the Ordovas-Montanes and von Andrian labs for insightful
857 discussions and advice. S.W.K was supported by the Cancer Research Institute's Irvington
858 Postdoctoral Fellowship. J.O.M is a New York Stem Cell Foundation – Robertson Investigator.
859 J.O.M was supported by the AbbVie-Harvard Medical School Alliance, the Richard and Susan
860 Smith Family Foundation, the AGA Research Foundation's AGA-Takeda Pharmaceuticals
861 Research Scholar Award in IBD – AGA2020-13-01, the HDDC Pilot and Feasibility P30
862 DK034854, the Leona M. and Harry B. Helmsley Charitable Trust, The Pew Charitable Trusts
863 Biomedical Scholars, The Broad Next Generation Award, The Chan Zuckerberg Initiative

Pediatric Networks, The Mathers Foundation, The New York Stem Cell Foundation, NIH R01 HL162642, NIH R01 DE031928 and The Cell Discovery Network, a collaborative funded by The Manton Foundation and The Warren Alpert Foundation at Boston Children's Hospital. This work was supported by the AbbVie–HMS Alliance Program. Sequencing of the scRNA-seq libraries was performed with AbbVie Inc. at the Genomics Research Center and Immunoprofiling Center in collaboration with Steven Leonardo (former AbbVie employee), Abel Suarez-Fueyo, Neha Chaudhary, Jozsef Karman (former AbbVie employee), Aridaman Pandit, and Amlan Biswas. Imaging was performed with MicRoN and HMS Center for Immune Imaging at Harvard Medical School. Anti-CCR2 antibody MC-21 and the X-31 IAV strain (A/HKx31) were generously provided by Prof. Matthias Mack (Universität Regensburg) and Prof. Daniel Lingwood (Ragon Institute of MGH, MIT, and Harvard) respectively. Training for the RNAscope experiments was facilitated by Anoohya N. Muppirala and Meenakshi Rao at Boston Children's Hospital. Daniel Lingwood (Ragon Institute of Mass General, MIT, and Harvard), Alex Shalek (MIT), Paolo Cadinu and Jeffrey Moffitt (BCH), Colin Bingle (Sheffield) provided helpful feedback and discussion on experimental design and interpretation of the results. Additionally, we would like to thank Susan Westmoreland for insightful discussions as well as Shankar Subramanian, Michelle Cordoba Gunter, Isabel Chico-Calero, Jochen Salfeld, and Mark Namchuk for supporting the AbbVie–HMS Alliance Program Area 1 which enabled the scope of this work.

Author contributions

Conceptualization, S.W.K., C.M., U.H.vA., and J.O-M,;

Methodology, S.W.K., C.M., and M.M.;

Software, S.W.K., E.M.L., and T.J.L.;

Formal Analysis, S.W.K., C.M., E.M.L., and T.J.L.;

Investigation, S.W.K., C.M., E.M.L., M.M., E.O., J.M., K.N., and J.O-M.;

Data Curation, S.W.K.;

Writing – Original Draft, S.W.K and C.M.;

Writing – Review & Editing, S.W.K., C.M., E.M.L., U.H.vA., and J.O-M.;

Supervision, U.H.vA. and J.O-M.;

Funding Acquisition, S.W.K., U.H.vA., and J.O-M.

Declaration of Interests

S.W.K. reports compensation for consulting services with Monopteros Therapeutics, Flagship Pioneering, and Radera Biosciences. J.O.M. reports compensation for consulting services with

898 Cellarity, Tessel Biosciences, and Radera Biotherapeutics. U.H.v.A. is a paid consultant with
899 financial interests in Avenge Bio, Beam Therapeutics, Bluesphere Bio, Curon, DNAlite, Gate
900 Biosciences, Gentibio, Intergalactic, intrECate Biotherapeutics, Interon, Mallinckrodt
901 Pharmaceuticals, Moderna, Monopteros Biotherapeutics, Morphic Therapeutics, Rubius, Selecta
902 and SQZ.
903
904

905 ***METHODS***
906 ***Resource availability***
907 **Lead contact**
908 Further information and requests for resources and reagents should be directed to and
909 will be fulfilled by the lead contact Jose Ordovas-Montanes (jose.ordovas-
910 montanes@childrens.harvard.edu).
911
912 **Material availability**
913 All the mouse lines used in this study are available from Jackson Laboratories. The anti-
914 CCR2 antibody MC-21 was provided as a gift by Prof. Matthias Mack. This study did not generate
915 new unique reagents.
916
917 **Data and code availability**
918 All sequencing data reported in this paper will be available in FASTQ read format and
919 cellbender corrected gene expression matrix format at Gene Expression Omnibus upon
920 publication as we plan to submit this work for pre-print. The annotated data can also be explored
921 at the Broad Institute Single Cell Portal under study numbers SCP2216 and SCP2221. All the
922 code generated and used to analyze the data reported in this paper will be available on GitHub
923 in the jo-m-lab/IAV-nasal-sc-atlas repository.
924
925 ***Experimental model and subject details***
926 **Mice**
927 All experiments were approved by the Harvard University Institutional Animal Care and
928 Use Committee and run following NIH guidelines. C57BL/6J (B6) mice 6 to 8 weeks old were
929 purchased from The Jackson Laboratory and experiments commenced 1 to 3 weeks following
930 their arrival. Mice were infected with 10^4 pfu PR8 in a 10μL volume that was administered by
931 pipette dropwise to the nares to allow each drop to be inhaled (5μl/nostril). Mice were restrained
932 during this administration but not anesthetized, to maintain the virus in the upper respiratory tract.
933 For rechallenge experiments mice previous inoculated with 10^4 pfu PR8 were administered with
934 either 10^4 pfu PR8 or 10^5 pfu X31 60 days after the initial PR8 infection. A higher dose of X31 was
935 used in rechallenge given its reduced pathology (Rutigliano et al., 2014). All mice were housed in
936 a BSL-2+ facility with specific pathogen free conditions.
937
938 ***Method details***

939 **Virus growth, quantification, and mouse infections**

940 IAV strain A/Puerto Rico/8/1934 (PR8) and Madin-Darby canine kidney (MDCK) cells were
941 generously provided by Dr. Daniel Lingwood and Dr. Maya Sangesland of the Ragon Institute of
942 Mass General, MIT, and Harvard. Virus was propagated and quantified in MDCK cells. MDCK
943 cells were grown at 37°C with 5% CO_2 in cell growth media: Dulbecco's modified eagle's medium
944 (DMEM) (Corning, #10-017-CV), 10% fetal bovine serum (FBS; Gemini #100-106), 1X
945 Penicillin:Streptomycin (Gemini, 100X stock: 400109). PR8 was grown in MDCK cells in influenza
946 growth media: Iscove's DMEM (Corning, # 10-016-CV), 0.2% bovine serum albumin (BSA; EMD
947 Millipore, EM-2960), 1Xm Penicillin:Streptomycin, and 2µg/mL TPCK treated Trypsin (Sigma,
948 T1426).

949 For viral load quantification experiments, mice were sacrificed in CO_2 and lungs and heads
950 were separated. For the nasal cavity, fur and skin were removed and the lower jaws cut off. The
951 entire nasal cavity or lungs were collected into 1mL PBS with 2.3mm Zirconia/Silica beads
952 (Biospec Products, 11079125z) and stored on ice. The tissue was homogenized in an OMNI Bead
953 Ruptor Elite at 3m/s for 30 seconds twice, centrifuged 500g for 5 minutes, and supernatant was
954 collected and stored at -80°C until thawed for plaque assays. Virus titers were measured by
955 plaque assays in confluent MDCK cells in 6-well plates. MDCK cells were grown in cell growth
956 media, washed with sterile phosphate-buffered saline (PBS), then washed with influenza growth
957 media. Media was removed and serial dilutions of viral supernatant in influenza growth media
958 were added to each well in a 400µL volume, incubated for 1 hour at 37°C, then overlayed with
959 0.3% agarose in influenza growth media. Infected cells were incubated for three days at 37°C,
960 fixed with 4% paraformaldehyde, stained with crystal violet, washed, and plaques were counted.
961

962 **Tissue harvesting, single-cell suspension preparation, and hashtag labeling**

963 Three separate regions of the nasal tissue were harvested independently: (1) the
964 respiratory mucosa (RM), (2) the olfactory mucosa (OM), and (3) the lateral nasal gland (LNG).
965 The nasal tissue was collected by removing the skin and connective tissue from around the head,
966 cutting off the lower jaw, and opening the nasal cavity by peeling away the nasal bone from the
967 rest of the skull. Tissue separation and collection was performed using a dissection scope with a
968 4x objective. All nasal tissue surrounding the nasoturbinates, maxillary turbinates, and septum,
969 including the mucosa that runs along the nasal lateral walls between the nasoturbinates and
970 maxillary turbinate, and the mucosal tissue under the nasal bone that connects the nasoturbinates
971 and septum, were collected together and constitute the RM. After removal of the RM the ethmoid
972 turbinates were collected including both the mucosal tissue and the bone and cartilage of the

973 turbinates, but not the surrounding skull, constituting the OM. After removal of the OM, the LNG
974 was exposed and could be collected without any bone or cartilage. The nasal-associated
975 lymphoid tissue (NALT) was not collected in any of the three regions. Matched RM, OM, and LNG
976 regions were collected simultaneously from the three mice per time point, and each time point
977 was processed on a different day.

978 Each nasal tissue region was collected into 750µL Wash Media (RPMI 1640, 2% FBS, 10
979 mM HEPES, and 100U/ml penicillin G, 100µg/ml streptomycin) and stored on ice. Tissues were
980 chopped with scissors then 750µL Digestion Media (Wash Media with 100µg/mL Liberase (Sigma,
981 #5401127001) and 100µg/mL of DNAse I (Roche, #10104159001)) was added. Tissues were
982 incubated at 37°C with end-over-end rotation, 30 minutes for RM and OM, 20 minutes for LNG.
983 13.3µL EDTA (0.5M) was added to each sample and then cells were washed with HBSS Media
984 (HBSS (Ca, Mg Free, 500 mL), 10mM EDTA, 10mM HEPES, 2% FBS) and filtered through a
985 70µm nylon cell strainer. Cells were pelleted by centrifugation 500g for 10 minutes, resuspended
986 with ACK (Ammonium-Chloride-Potassium) lysis buffer for 1 minute on ice, and then diluted with
987 9mL HBSS Media and centrifuged 500g for 5 minutes twice. Cells were then resuspended in 1mL
988 Isolation Buffer (PBS, 0.1% BSA, 2mM EDTA) pre-mixed with 25µL anti-EpCAM-biotin-
989 Dynabeads (anti-EpCAM-biotin antibody (G8.8, Biolegend) bound to Dynabeads Biotin Binder
990 (ThermoFisher)) for a light epithelial cell depletion, incubated for 15 minutes on ice, washed with
991 Isolation Buffer and placed on a Dynamag for 2 minutes. Supernatants were collected, centrifuged
992 500g for 5 minutes, resuspended in 100µL Staining Buffer (PBS, 1% BSA, 0.01% Tween) and
993 10µL Fc block, and incubated on ice for 10 minutes. Next, 0.5µg Biolegend TotalSeq Hashing
994 antibodies B0301, B0302, or B0303 were added so that each mouse had all three nasal regions
995 (RM, OM, and LNG) stained with one of the three antibodies, and incubated on ice for 20 minutes.
996 Cells were then washed extensively to remove excess antibody with 10mL Staining Buffer and
997 centrifugation at 500g for 5 minutes twice. Cells were resuspended in Loading Buffer (PBS and
998 0.04% BSA), counted, and pooled equally (13,500 cells/sample) between three mice for each
999 region. Finally, each set of pooled cells were centrifuged 500g for 5 minutes and resuspended in
1000 42µl Loading Buffer for downstream scRNA-seq processing.
1001

1002 **Single-cell RNA-seq**

1003 Pooled samples from each nasal region (RM, OM, and LNG) were processed using the
1004 10x Genomics Chromium Next GEM Single Cell 3' Kit v3.1 and Feature Barcoding Kit with dual
1005 indices per the manufacturer's instructions. Approximately 40,000 cells per pooled reaction were
1006 loaded on the 10x Genomics Chromium Controller. Library quality was evaluated using the Agilent

1007 TapeStation 4200 (Agilent). Prior to sequencing, the gene expression and hashtag libraries were
1008 pooled 20:1. Sequencing was performed on either the NovaSeq 6000 or NextSeq 2000 (Illumina)
1009 with an average RNA read depth of 16,000 reads/cell and hashtag read depth of 500 reads/cell.
1010

1011 **Immunofluorescence Microscopy**

1012 Mice were euthanized in CO_2 and their heads following skin, fur, and lower jaw removal
1013 were placed in 4% paraformaldehyde for 1-4 hours on ice for fixation. Heads were transferred to
1014 0.5M EDTA for 2-3 days at 4°C for bone decalcification. Heads were transferred to 30% sucrose
1015 in PBS for cryoprotection for 2 days at 4°C then rapidly frozen in NEG-50 using dry ice. Frozen
1016 heads were stored at -20°C until cryostat sectioning. Mouse nasal tissues were cut into 50-100μm
1017 sections, permeabilized with 0.3% Tween in PBS (PBST) for 1 hour, then incubated overnight at
1018 4°C with antibodies, DAPI, and Fc block at a 1:200 dilution in PBST. Antibodies used: anti-
1019 Influenza A virus NS1 (PA5-32243, ThermoFisher), anti-acetyl-α-tubulin (Ly640, D20G3, Cell
1020 Signaling Technology), anti-CD45 (30-F11, Biologend), anti-EpCAM (G8.8, Biolegend), anti-Krt13
1021 (EPR3671, Abcam), anti-PD-L1 (10F.9G2, Biolegend), and anti-IgA (mA-6E1, ThermoFisher).
1022 Samples were then washed 3 times with PBST in 15-minute intervals at room temperature,
1023 mounted on glass slides with Prolong Gold, and visualized with an Olympus FLUOVIEW FV3000
1024 confocal laser scanning microscope.
1025

1026 **qPCR**

1027 RM tissue was collected as described above from mice and lysed in Buffer RLT (Qiagen)
1028 + 1% beta-mercaptoethanol (Sigma) via gentleMACS Octo Dissociator in M-Tubes (Miltenyi
1029 Biotec). RNA was extracted from tissue lysate by RNAEasy Mini column purification (Qiagen)
1030 following the manufacturer's instructions. cDNA was then generated following the SmartSeq II
1031 protocol as previously described (Trombetta et al., 2014). qPCR was performed using TaqMan
1032 reagents and probes (ThermoFisher) on a CFX384 Real-Time PCR System.
1033

1034 **Antibody-based depletion**

1035 Naïve or PR8 infected B6 mice were administered daily 20μg anti-CCR2 depleting
1036 antibodies (MC-21 generously provided by Prof. Matthias Mack, Universität Regensburg) or rat
1037 IgG2b,κ isotype control (Biolegend, #400644) intraperitoneally (i.p.). 24h following one
1038 administration, blood was collected from naïve mice by tail vein bleed into FACS buffer (PBS,
1039 0.5% BSA, 2mM EDTA) and stored on ice before processing for flow cytometry.

1040 PR8 infected mice were administered antibodies 3, 4, and 5 dpi in 24h intervals. For this
1041 experiment, mice were euthanized at 8 dpi.
1042
1043 **Flow cytometry**
1044 Blood was processed for flow cytometry by pelleting cells by centrifugation and
1045 resuspending with ACK lysis buffer to remove RBCs. Cells were then washed with FACS buffer
1046 and stained in 50 µL for flow cytometry using the following antibodies: anti-CCR2 (475301, R&D
1047 Systems), anti-CD11b (M1/70, Biolegend), anti-CD19 (6D5, Biolegend), anti-CD3e (145-2C11,
1048 Biolegend), anti-CD45 (30-F11, Biologend), anti-Ly6C (HK1.4, Biolegend), anti-Ly6G (1A8,
1049 Biolegend), and anti-NK1.1 (PK136, Biolegend). Cells were analyzed using the Beckman Coulter
1050 CytoFLEX.
1051 For RM tissue, mice were anesthetized i.p. with ketamine (100 mg/kg body weight) and
1052 xylazine (10 mg/kg body weight) prior to euthanasia and administered 1µg anti-CD45 antibody
1053 (30-F11, Biologend) by retroorbital intravascular injection to label CD45+ cells in circulation. Mice
1054 were then euthanized 3 minutes later in CO_2. RM tissue was processed as described above for
1055 tissue harvesting and single-cell suspension preparation through ACK lysis and dilution. Cells
1056 were then centrifuged and resuspended in 100 µL FACS buffer LIVE/DEAD Fixable Aqua Dead
1057 Cell Stain (ThermoFisher #L34966) per manufacturer's instructions. Cells were then washed and
1058 stained for 30min at 4°C in the dark with Fc block diluted 1:200 and subsets of the following
1059 antibodies: anti-CD103 (2E7, Biolegend), anti-CD11b (M1/70, Biolegend), anti-CD11c (HL3, BD
1060 Biosciences), anti-CD19 (6D5, Biolegend), anti-CD3e (145-2C11, Biolegend), anti-CD4 (GK1.5,
1061 Biolegend), anti-CD45 (30-F11, Biologend), anti-CD64 (X54-5/7.1, Biolegend), anti-CD69
1062 (H1.2F3, Biolegend), anti-CD8b (YTS156.7.7, Biolegend), anti-Ly6C (HK1.4, Biolegend), anti-
1063 Ly6G (1A8, Biolegend), anti-F4/80 (BM8, Biolegend), anti-MHC-II (M5/114.15.2, Biolegend), and
1064 anti-NK1.1 (PK136, Biolegend). To stain for Krt13, IgA, and IgK/L intracellularly, cells were fixed
1065 and permeabilized using the eBioscience Transcription Factor Staining Buffer Set (ThermoFisher
1066 #00-5523-00) according to the manufacturer's instructions. Cells were stained with anti-Krt13
1067 (EPR3671, abcam) at 1:200, or anti-IgA (mA-6E1, eBioscience), anti-IgK (187.1, BD
1068 Biosciences), and anti-IgL (R26-46, BD Biosciences) at 1:100. Following staining, cells were
1069 washed in FACS buffer, and analyzed. To determine cell counts, AccuCheck Counting Beads
1070 (ThermoFisher #PCB100) were added to every sample.
1071
1072 **RNAscope Microscopy**

1073 RNA *in situ* hybridization was performed according to manufacturer's instructions for the
1074 RNAscope Multiplex Fluorescent Reagent Kit v2 (Advanced Cell Diagnostics ACD, 323270) on
1075 20 µm thin sections of fixed-frozen murine nasal mucosa tissue collected 14 dpi. We implemented
1076 the following modifications to preserve tissue integrity: 1) 5 min PBS wash preceding initial baking
1077 of slides was removed; 2) slides were baked for 30 min at 60°C following EtOH dehydration; 3)
1078 target retrieval time was reduced to 5 min; 4) slides were baked for 60 min at 60°C following target
1079 retrieval; and 5) tissue sections were incubated in Protease Plus instead of Protease III for milder
1080 protease digestion. Probes used included Mm-Krt13 (ACD, 575341), Mm-Cxcr6-C2 (ACD,
1081 871991-C2), Mm-Cxcl16-C3 (ACD, 466681-C3), and Mm-Cd274-C3 (ACD, 420501-C3).
1082 Following signal amplification, Opal 520 (Akoya Biosciences, FP1487001KT), Opal 570 (Akoya
1083 Biosciences, FP1488001KT), and Opal 690 (Akoya Biosciences, FP1497001KT) dyes were used,
1084 diluted 1:1000 in TSA buffer (ACD, 322809). Nuclei were stained with DAPI and slides were
1085 mounted with VECTASHIELD PLUS (Vector Laboratories, H-1900). Confocal images were
1086 collected using an Olympus FLUOVIEW FV3000 confocal laser scanning microscope.
1087
1088 ***Quantification and statistical analysis***
1089 **Single-cell RNA-seq alignment, cleanup, and pre-processing**
1090 To detect reads originating from IAV, we built a combined genome of mm10 (GRCm39)
1091 and the sequences for PR8 (NCBI Taxonomy ID #211044). The eight PR8 genomic viral segment
1092 sequences (NC_002023.1, NC_002022.1, NC_002021.1, NC_002020.1, NC_00219.1,
1093 NC_2018.1, NC_002017.1, and NC_002016.1) and associated IAV gene annotations were added
1094 to the GRCm39 FASTA and GTF files and processed using the CellRanger's built in "mkref"
1095 function. Sequences were then aligned and quantified using this combined genome with the
1096 CellRanger toolkit (v6.0.1) via Cumulus tools (Li et al., 2020)
1097 (https://cumulus.readthedocs.io/en/stable/). Cell sample identity was assigned from the
1098 measurement of TotalSeqB aligned counts using the cumulus demultiplexing tool for feature
1099 barcoding, calling identity for any cell with at least 100 barcodes. To correct for transcript spill-
1100 over, cellbender (Fleming et al., 2022) was applied to the raw output UMI matrices from
1101 CellRanger with the following parameters: *expected_cells=30000*, *fpr=0.01,*
1102 *total_droplets_included=50000*. Cellbender corrected cells were then filtered based on Unique
1103 Molecular Identifiers (UMI) count (>750 & <10000), number of detected genes (>500), and
1104 percentage of mitochondrial genes (<15%). Finally, cells labeled as doublets by demultiplexing
1105 were removed.
1106

1107 **Iterative clustering, cell cluster annotation, and IAV+ cell calling**

1108 Downstream analysis was performed using Seurat (v.4.2.1) (Hao et al., 2021). Briefly, the
1109 entire primary infection dataset underwent normalization using the *scTransform* function followed
1110 by principal component analysis (PCA), shared nearest neighbors (SNN) graph generation,
1111 Louvain clustering, and UMAP embedding. Clustering was performed at multiple resolutions to
1112 help annotate similar and dissimilar clusters. Using clustering *resolution = 0.6,* cluster
1113 specific/enriched markers were calculated. Each cluster was labeled by major cell type based on
1114 the expression of known lineage markers (e.g., *Omp*, *Epcam*, *Ptprc, Flt1,* etc.). Doublet clusters
1115 were also annotated based on the lack of unique markers and/or the presence of multiple mutually
1116 exclusive lineage markers (e.g., *Omp*+*Ptprc*+ cells). Following annotation, doublet clusters were
1117 removed, and the normalization/clustering/doublet removal process was repeated twice more
1118 (total of three times) until no doublet clusters were discernable.

1119 The dataset was then divided into separate objects by cell type label for further
1120 subclustering. Following the same routine applied to the full dataset, clusters for each cell type
1121 were annotated with subset/state labels based on prior knowledge and previously published
1122 scRNAseq datasets of the nasal mucosa (Brann et al., 2020; Ualiyeva et al., 2024; Ziegler et al.,
1123 2021). After the first set of annotations in every cell type object, it was apparent that there were
1124 still intra-sample doublets present: mostly contaminating cell types, but also within cell type
1125 doublets (e.g., ionocyte/sustentacular doublets). These clusters were iteratively removed like in
1126 the analysis of the full dataset, for a total of three rounds in each cell type, yielding a total of 127
1127 clusters across the whole dataset. To visualize these clusters' relationships and distribution
1128 across nasal regions, we built a cell cluster "phylogenetic tree" using ARBOL (Zheng et al., 2021),
1129 where the first tier encodes major cell type, the second tier encodes defined subtypes, and the
1130 third tier encodes cluster identity (**Figure S1F**).

1131 We note that neurons, mostly olfactory sensory neurons, make up a large number of cells
1132 in our primary infection dataset (n > 50,000). Given their importance in mouse olfaction, and their
1133 broad distribution through the OE and OM (**Figure 1B**), we believe that their relative abundance
1134 in our scRNA-seq data is concordant with the anatomy and biology of the nasal mucosa.

1135 Since IAV transcript capture was sparse, we classified IAV+ cells as any cell with 2 or
1136 more UMIs aligned to any IAV PR8 gene.

1137

1138 **Compositional analyses**

1139 After removing multiplets, immune (>97.5%) and endothelial cells (89%) had nearly all
1140 cells assigned a sample replicate while neurons (30.7%), epithelial cells (65.9%), fibroblasts

1141 (52.4%), and other stromal cells (56.4%) had lower sample annotation rates (**Figure S1E**). We
1142 note that cells without a sample replicate assignment were excluded from all compositional
1143 analyses. Within cell type frequencies were calculated on a per replicate basis by counting the
1144 number of cells within each cluster label and dividing by the total number of cells for that cell type
1145 captured in that replicate. For tissue- and region-level compositional analyses, cell cluster
1146 abundances were calculated by deriving cell cluster frequencies over all labeled cells in each
1147 sample replicate, scaling to 3,000 cells per replicate, and log transforming. Subsequent PCAs
1148 were calculated using the center-log-ratio (clr) transformed data.

1149 Proportionality analysis was performed using the propr package (v4.2.6) (Quinn et al.,
1150 2017). We compared the proportionality statistic **ρ,** calculated from the clr transformed abundance
1151 data**,** to standard Pearson correlation across all pairwise comparisons and found **ρ** to be more
1152 stringent for significance cutoffs (FDR<0.05) generated by permutating testing (**Figure S8A**). We
1153 built a network using Cytoscape (v3.9.1) comprised of all significantly proportional cell cluster
1154 pairs to assess groups of cell clusters with similar cell abundance trajectories throughout the
1155 infection time course.

1156 RM sample replicate distances were calculated using the Aitchison distance (Aitchison et
1157 al., 2000). Euclidean distance on the clr transformed data then calculated between all pairs of RM
1158 sample replicates, yielding three distances within a timepoint and nine distances between two
1159 timepoints. Statistics on Aitchison distances were performed using a one-sided non-parametric
1160 Welch's ANOVA and Dunnett's T3 test for multiple comparisons in Prism.

1161

1162 **Neutrophil pseudotime analysis**

1163 The neutrophil pseudotime analysis was performed using diffusion mapping as previously
1164 described (Grieshaber-Bouyer et al., 2021). A principal component analysis was run on all cells
1165 assigned to granulocyte clusters, excluding mast cells. The first 20 principal components were
1166 used to compute a cell-to-cell distance matrix using *1 – Pearson correlation coefficient* as the
1167 distance metric. Using the destiny package in R (Angerer et al., 2016), we computed a diffusion
1168 map with standard parameters with density normalization and rotate enabled. We manually
1169 selected "Progenitor" cells as the root of the trajectory and used the DPT function to calculate the
1170 pseudotime values, manually scaling the values from 0 to 1.

1171

1172 **Cell-cell signaling analysis**

1173 Three cell networks (IFN-stimulated MDMs : *Gzmk*+ CD8 T cells : *Ifng*+*Cd200*+ CD4 T
1174 cells; *Cd103*+ DCs : *Dusp2*+*Icam1*+ mature neutrophils : *Gp2*+*Lyz2*+ goblet/secretory cells*;*

1175 *Krt13*+*Il1a*+ epithelial cells : *Cd103*+ CD8 T cells : CD4 T cells) were selected based on high
1176 proportionality throughout the primary infection time-course or specific biological interest to the
1177 authors. Data for the clusters of interest in each network were then subset to RM and timepoint
1178 of interest to best capture individual cells with sufficient spatial and temporal proximity to plausibly
1179 interact, and re-normalized with Seurat's *NormalizeData* function. Since NICHES calculates the
1180 multiplicative expression of ligand-receptor pairs from a random sampling of cells from each cell
1181 type to predict cell-cell communication, Adaptively thresholded Low-Rank Approximation (ALRA)
1182 imputation was applied to each cell network to reduce the impact of technical zeros due to
1183 potential dropout events (Linderman et al., 2022). NICHES was then run on each cell network
1184 individually, drawing from the OmniPath database of ligand-receptor pairs (Türei et al., 2016) to
1185 generate a cell interaction object whereby rows are ligand-receptor pairs and columns are cell
1186 type pairs (Raredon et al., 2023). These objects were then scaled and passed through principal
1187 component analysis and UMAP dimensionality reduction to generate low-dimensional
1188 embeddings of cell interactions. Differentially expressed interactions were identified using the
1189 Seurat *FindAllMarkers* function, and highly differentially expressed interactions validated by
1190 literature review were selected for display as heatmaps.
1191
1192 **RNAscope co-localization quantification**
1193 RNAscope quantification was carried out using ImageJ software on five fields of view
1194 (FOV) from both the naïve and 14 dpi timepoints (n = 5/timepoint). Ten slices were selected in
1195 the z-plane from each FOV to generate maximum intensity projections across 5 μm, and color
1196 channels were separated using the "Split Channels" function. For each image, a threshold was
1197 set for signal intensity in the *Krt13* channel, allowing generation of a mask of *Krt13* expression
1198 that was subsequently overlaid on both the DAPI and *Cxcl16* channels to generate regions of
1199 interest for further analysis. Within the region of interest in the DAPI channel, nuclei were manually
1200 counted with the aid of the ImageJ plugin "Cell Counter," with inclusion of most segmented nuclei.
1201 Within the region of interest in the *Cxcl16* channel, a threshold was set for *Cxcl16* expression with
1202 the aid of a signal intensity histogram and then punctuate dots were counted automatically with
1203 the "Analyze Particles" function. A measure of average *Cxcl16* puncta per DAPI-stained nuclei in
1204 the *Krt13*+ region was calculated for each FOV.
1205
1206 **Cluster annotation in memory samples**
1207 To assign cluster labels to new scRNA-seq datasets generated from the nasal mucosa,
1208 we leveraged the structure of our data to test the label transfer methods provided in Seurat (Hao

et al., 2021) and scANVI (Xu et al., 2021). We separated the cells from one RM replicate from each time point as a query dataset, using the remaining cells as the reference. With Seurat, we implemented the FindTransferAnchors function on the scTransformed data, using the first 40 PCs from the PCA as the reference. Labels were then assigned with the TransferData function using either cell cluster or cell type identities. With scANVI, we first built a scVI model on the reference data, and then a scANVI model using either cell cluster or cell type identities as labels. The reference scANVI model was then used to train a model on the query data. We calculated the percentage of correctly called cell labels using each method for both sets of labels and found calling to be superior on the cell type level. Thus, we next repeated each procedure within each cell type to learn cell cluster labels and found Seurat to perform better across all cell types (**Figure S9C**). This approach was repeated using two other non-overlapping sets of sample replicates (one per time point) to assess reproducibility. To further validate, we calculated cell cluster abundances using the predicted cell cluster labels for the query replicates and projected into the PCA calculated across the RM samples.

We next applied the two-step label transfer approach using Seurat to new data generated from RM 60 dpi and 2 and 5 dprc. Before performing label transfer, we removed all hashtag annotated cell doublets from the new dataset and applied the same filtering criteria as above. We next performed *scTransform* and PCA on the new dataset. We then predicted cell type labels using all cells from RM samples in the primary infection dataset for reference. We next removed any cells from subsequent analysis that had a maximum prediction assignment score < 0.8 (i.e., 80% is the greatest confidence in label prediction), making up 5% of the total dataset. Given our loading strategy and number of intrasample doublets found in the primary infection dataset, we chose a more stringent cutoff following cell type label prediction. Separating into each cell type and using the processed data from the matching cell type in the primary infection dataset as reference, we performed the same procedure. Here, we were more liberal, keeping all cells with a maximum prediction assignment score ≥ 0.4 since very similar clusters within cell types could receive almost equal prediction probability (e.g., Resting Basal and Abi3bp Resting Basal). With cell cluster labels assigned, we then calculated cell cluster abundances as above and performed downstream differential expression analysis.

1240 ***MAIN TEXT FIGURES***

Figure 1

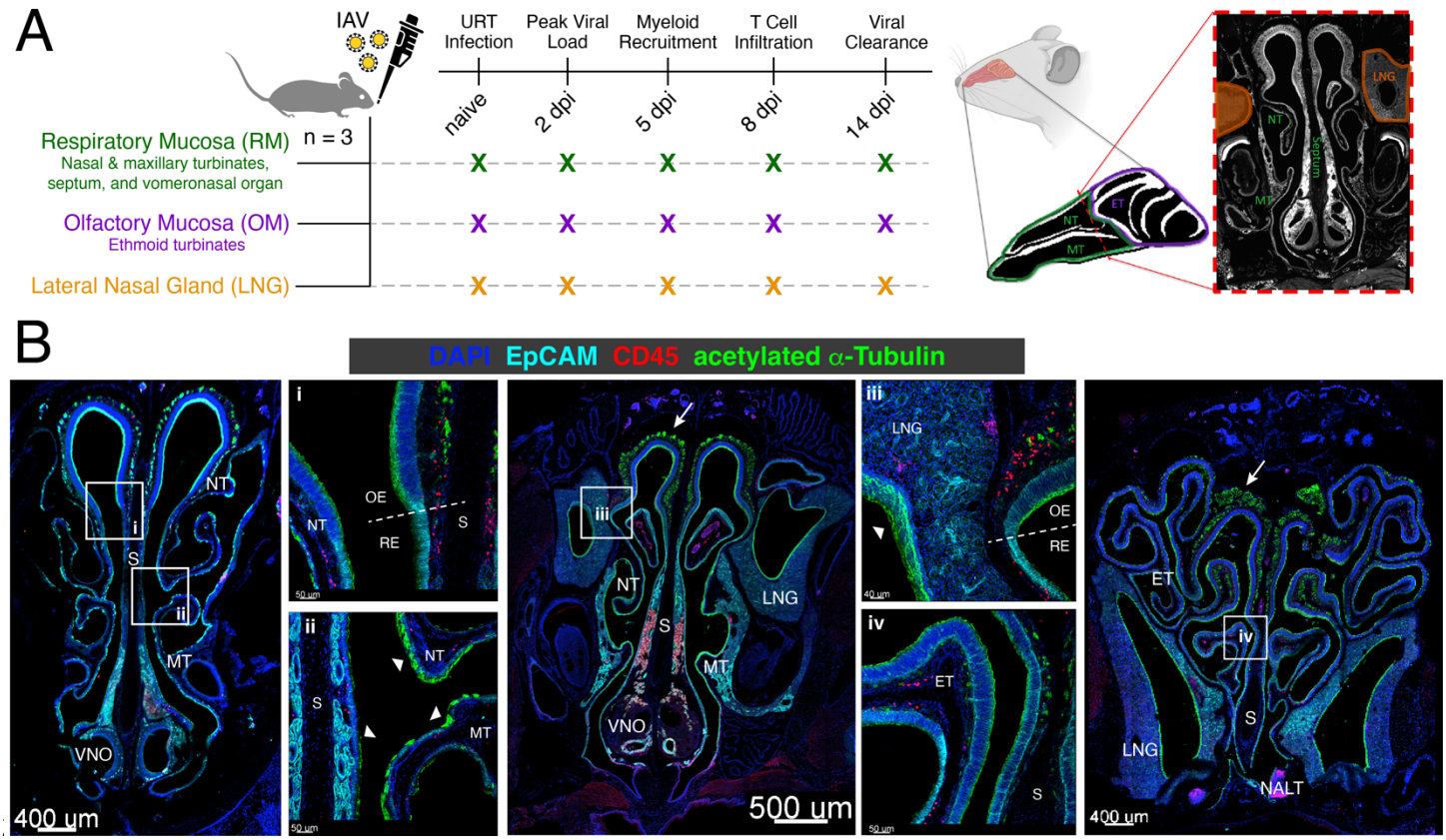

1242 **Figure 1: Experimental design and the structure of the murine nasal mucosa**

1243 (A) Schema depicting the sampling scheme and three tissue regions collected and processed
1244 for scRNA-seq: respiratory mucosa (RM), olfactory mucosa (OM), and lateral nasal gland
1245 (LNG). To infect, 10^4 pfu Influenza A Virus (IAV) PR8 was administered intranasally
1246 (5µl/nostril). dpi = days post infection

1247 (B) Representative immunofluorescence images of coronal slices of the nasal mucosa from a
1248 naïve mouse moving from anterior (left) to dorsal (right) staining for epithelial cells (EpCAM,
1249 teal), immune cells (CD45, red), and ciliated cells/neurons (α-acetylated tubulin, green).
1250 Distinct regions of the mucosa are labeled. Labeled white boxes outline higher resolution
1251 images below. White arrows point to olfactory sensory nerve bundles; white arrowheads point
1252 to cilia. The olfactory epithelium (OE) and respiratory epithelium (RE) both reside within the
1253 collected RM tissue and are differentiated by morphology and the presence of olfactory
1254 sensory neurons. NT = nasoturbinate; S = septum; MT = maxillary turbinate; VNO =
1255 vomeronasal organ; LNG = lateral nasal gland; ET = ethmoid turbinate; NALT = nasal-
1256 associated lymphoid tissue.

1257

Figure 2

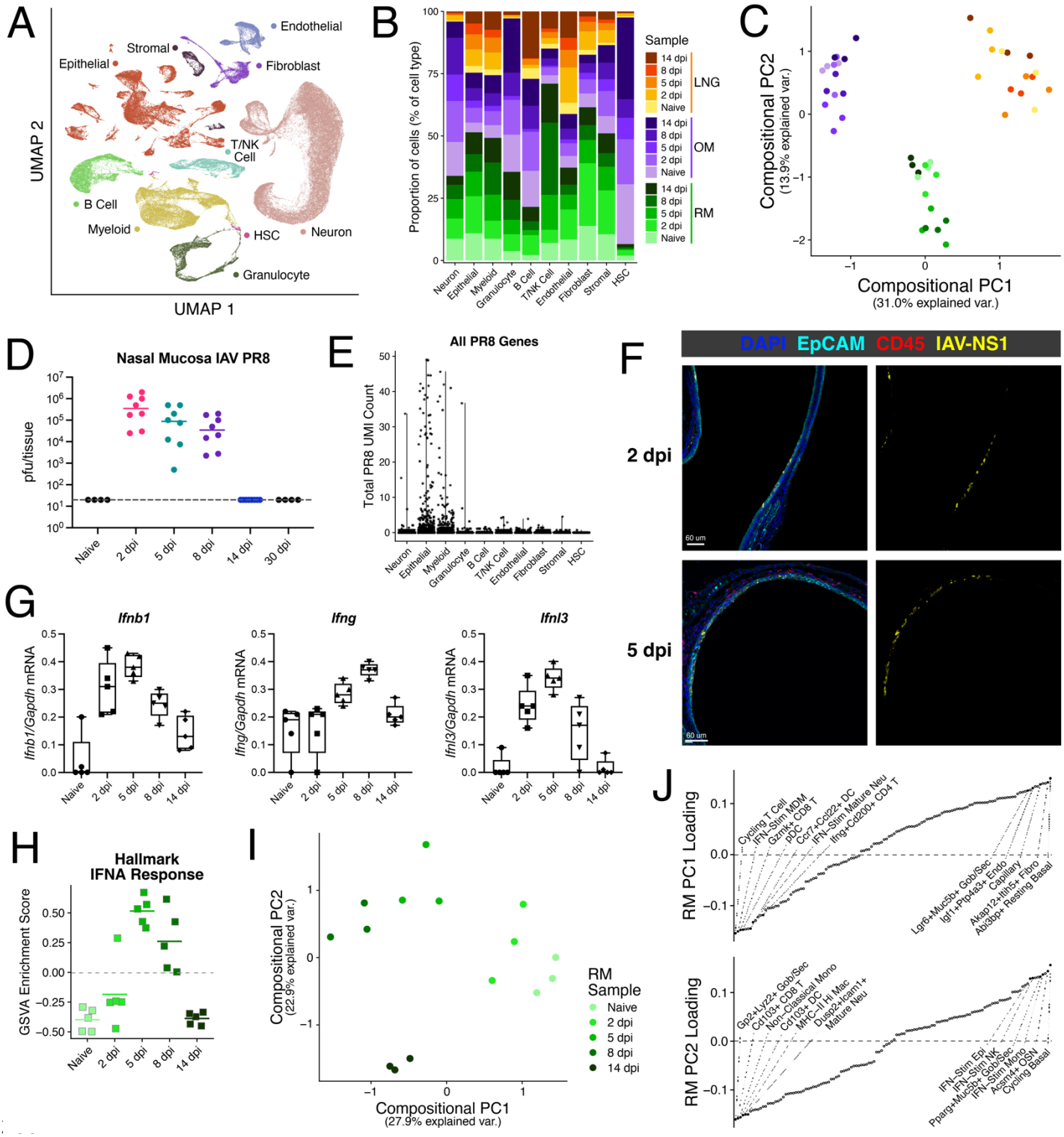

1259

1260 **Figure 2: Single-cell atlas of the nasal mucosa during primary IAV infection**

1261 (A) UMAP embedding of 156,572 nasal cells across three tissue regions and five time points
1262 (n=3 per region/timepoint) colored by cell type. HSC = hematopoietic stem cell.

1263 (B) Stacked bar chart depicting the relative proportions of cells annotated for each cell type by
1264 region and time point.

1265 (C) Compositional principal component analysis (PCA) of all acute infection sample replicates.
1266 Each point represents a sample replicate and distance reflects variation in cell cluster
1267 abundance (scaled cell counts). Dots are colored by region and time point as in **B**.

1268 (D) Infectious IAV PR8 quantification in plaque forming units (pfu) of the entire nasal mucosa.

1269 (E) Summative scTransform-corrected UMI counts per cell across all IAV PR8 genes split by cell
1270 type.

1271 (F) Representative images of IAV infection in RM taken from mice 2 dpi (top) and 5 dpi (bottom).
1272 Staining for EpCAM (teal), CD45 (red), and IAV-NS1 (yellow). Images on the right depict only
1273 the signal in the IAV-NS1 channel.

1274 (G) qPCR of *Ifnb1* (left), *Ifng* (center), and *Ifnl3* from RNA extracted from RM tissue. C_q ratios are
1275 normalized by *Gapdh* C_q. n = 5 per time point.

1276 (H) Gene Set Variation Analysis (GSVA) Enrichment score for Hallmark Response to Interferon-
1277 Alpha on total RM tissue lysate bulk RNA-seq data (n = 5/time point).

1278 (I) Compositional PCA of all cell clusters from only RM samples.

1279 (J) Cell cluster abundance loadings for PC1 (left) and PC2 (right) from (G). Cell cluster names
1280 for several of the most negative and most positive weights for each PC are depicted.

1281

Figure 3

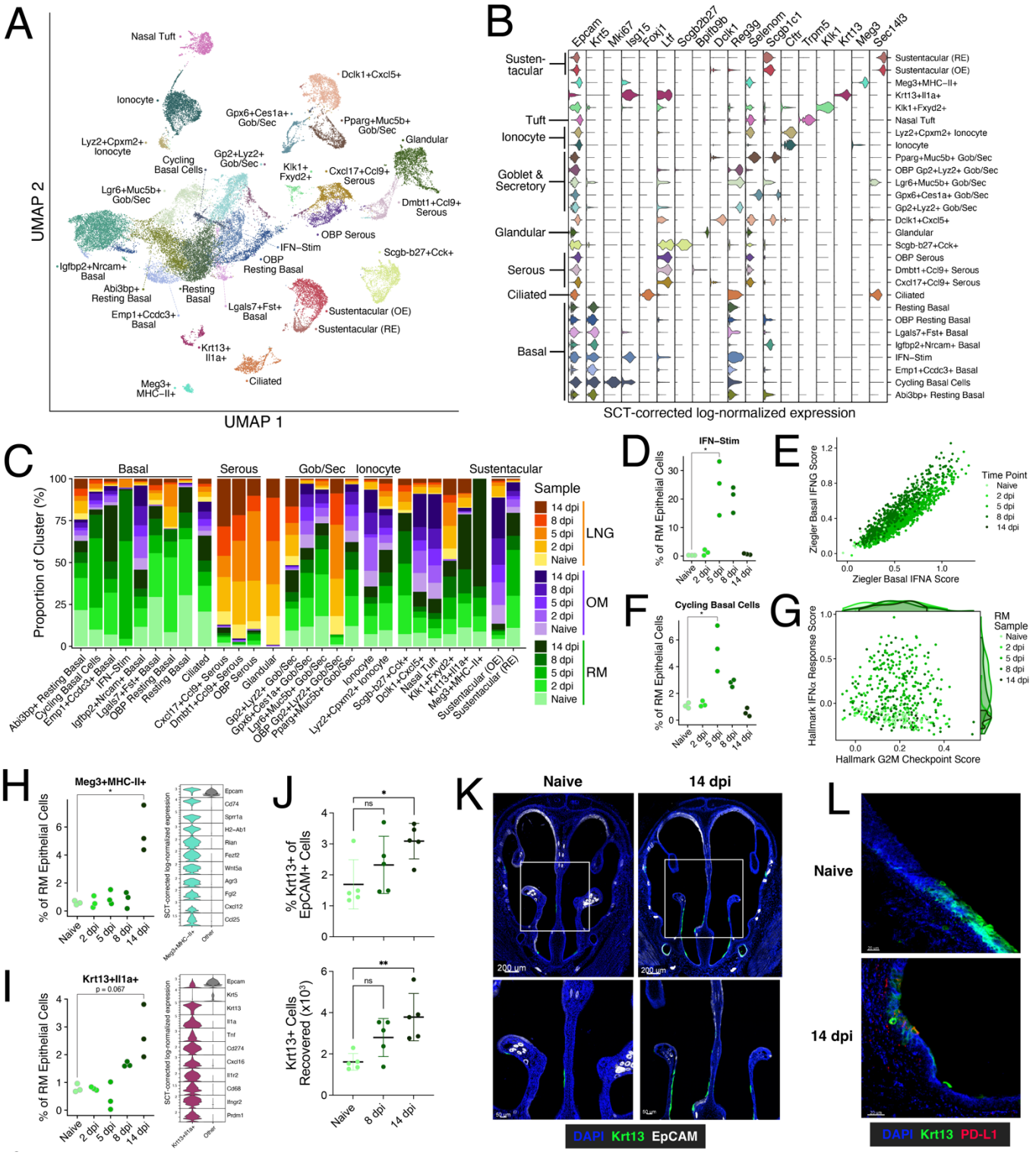

Figure 3: Epithelial cell subclustering reveals diverse subsets including transient IFN-responsive/cycling cells and rare cells with immune-interaction potential arising 14 dpi

1285 (A) UMAP embedding of 38,367 epithelial cells across 27 clusters.
1286 (B) Violin plot depicting epithelial lineage and subset marker expression levels (scTransform-
1287 corrected log-normalized UMI counts) across all discovered clusters (see **Supplementary**
1288 **Table 1**).
1289 (C) Stacked bar chart depicting the relative proportions of cells annotated for each cluster by
1290 region and time point.
1291 (D) Relative frequencies of cells clustered as IFN-Stim as a proportion of all epithelial cells per
1292 replicate RM sample. Only cells with assigned hash calls are included. Welch's t test, *$p <$
1293 0.05.
1294 (E) IFN-Stim epithelial cell scores for signatures derived from airway basal cell cultures
1295 stimulated with IFNα or IFNγ (Ziegler et al., 2020).
1296 (F) Same as in (D) for the cycling basal cell cluster.
1297 (G) Scatter plot of gene module scores for the Hallmark IFNα Response and Hallmark G2M
1298 Checkpoint gene lists (MsigDB v7.5.1) in cycling basal cells. Density plots represent the
1299 scatter plot data.
1300 (H & I) Relative frequency plots of *Meg3*+MHC-II+ (G) and *Krt13*+*Il1a*+ (KNIIFE cells) (H) clusters
1301 (left) as a proportion of all epithelial cells per replicate RM sample. Violin plots of select cluster
1302 specific/enriched genes, except for *Epcam* and *Krt5* (FDR corrected p-values $\leq 10^{-242}$ by 1-
1303 vs-rest Wilcoxon Rank Sum Test) (right).
1304 (J) Mice were infected with 10^4 PFU IAV PR8 and RM tissue was collected and stained
1305 intracellularly for Krt13+ epithelial cells (n = 5/timepoint). Kruskal-Wallis test, *$p < 0.05$, **$p <$
1306 0.01.
1307 (K) Representative immunofluorescence images of the very anterior nasal mucosa in naïve mice
1308 (left) and 14 dpi (right) staining for Krt13 (green) and EpCAM (white).
1309 (L) Representative images within the region shown in (I) in naïve mice (top) and 14 dpi (bottom)
1310 staining for Krt13 (green) and PD-L1 (red). Welch's t test, *$p < 0.05$.
1311

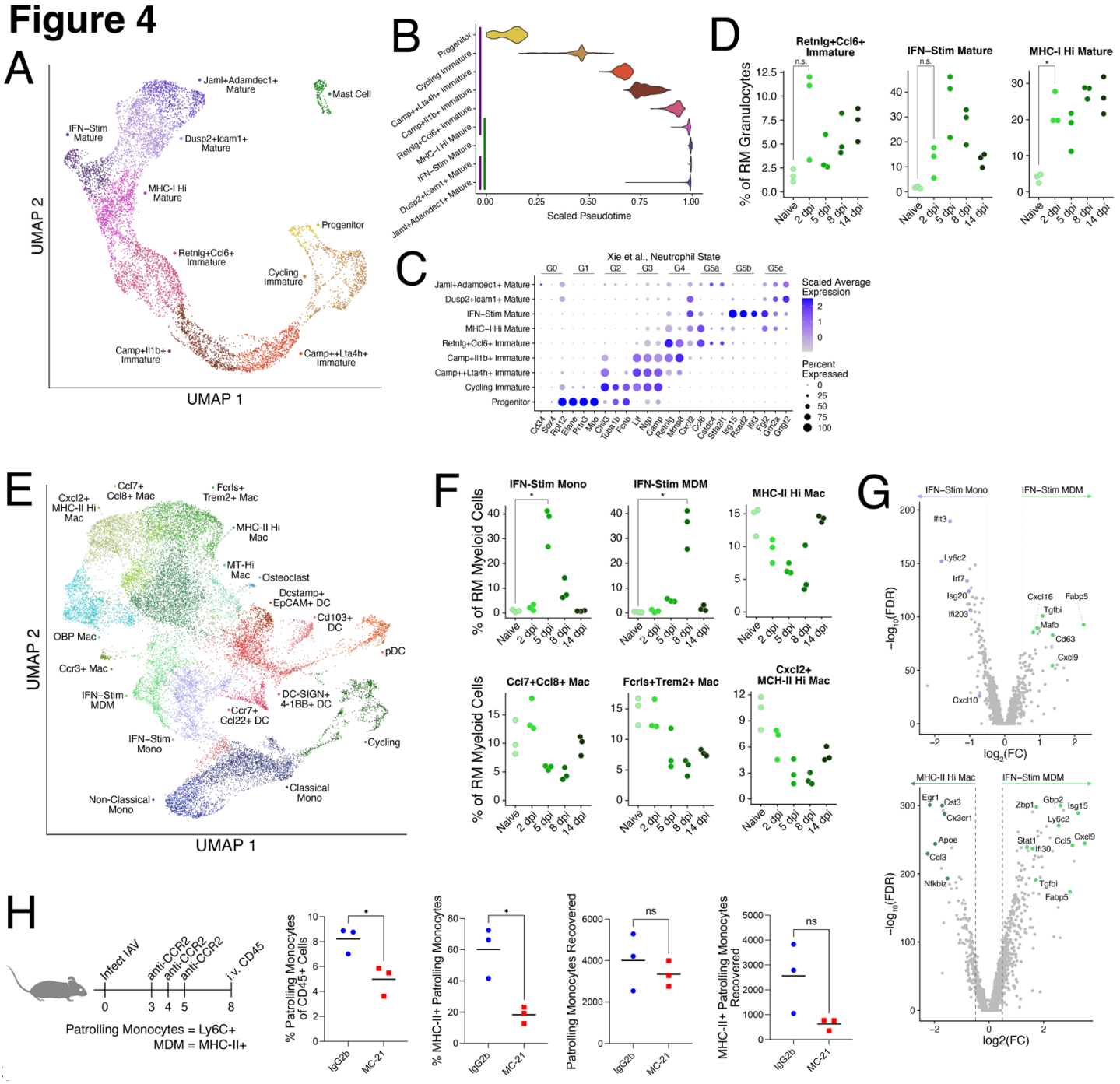

Figure 4: Immediate neutrophil responses are bolstered by recruited antiviral monocytes that differentiate into antiviral monocyte-derived macrophages

(A) UMAP embedding of 7,987 granulocytes across 10 clusters.

(B) Violin plot of assigned pseudotime values to all granulocytes (except mast cells) split by cluster identity. Purple (OM) and green (RM) bars depict in which regions each cluster can be found at high frequencies (see **Figure S4B**).

1319 (C) Expression of blood neutrophil development genes annotated in (Xie et al., 2020) across
1320 nasal mucosa neutrophil clusters.
1321 (D) Relative frequencies of various neutrophil clusters as a proportion of all granulocytes per
1322 replicate RM sample. Only cells with assigned hash calls are included. Welch's t test, *$p <$
1323 0.05.
1324 (E) UMAP embedding of 22,654 macrophages, monocytes, and dendritic cells (DCs) across 17
1325 clusters.
1326 (F) Relative frequencies of various myeloid cell clusters as a proportion of all macrophages,
1327 monocytes, and DCs per replicate RM sample. Welch's t test, *$p < 0.05$.
1328 (G) Volcano plots depicting differentially expressed genes ($|\log2FC| \geq 0.5$; FDR < 0.01) between
1329 IFN-Stim MDMs and IFN-Stim Mono (top) and between IFN-Stim MDMs and MHC-II-Hi Macs
1330 (bottom). Only cells from RM were used in the differential expression analysis. Genes of
1331 interest are labeled.
1332 (H) Mice were infected with 10^4 pfu IAV PR8 and then treated on 3, 4, and 5 dpi with either MC-
1333 21 (anti-CCR2; n=3) or IgG2b (isotype control; n=3). At 8 dpi mice received anti-CD45
1334 intravascularly immediately prior to euthanasia to distinguish cells in the tissue from those in
1335 circulation. Patrolling monocytes were distinguished from circulating monocytes based on
1336 lower expression of Ly6C. Flow cytometry statistics are gated on CD45-EV+ cells; Welch's t
1337 test, *$p < 0.05$.
1338

Figure 5

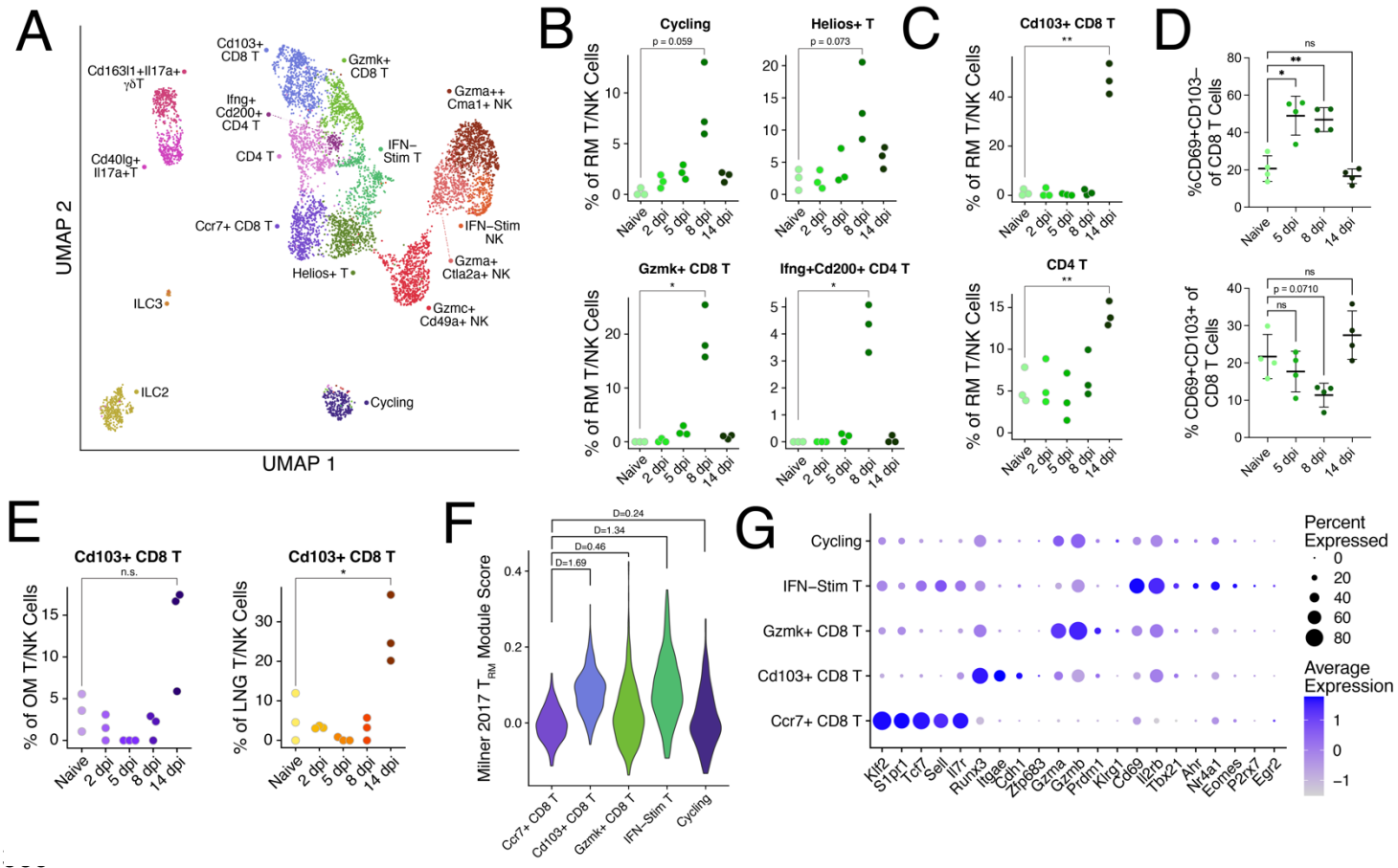

Figure 5: Effector CD4 and CD8 T cells 8 dpi are replaced by T_{RM} cells following viral clearance

(A) UMAP embedding of 6,573 T, NK, and innate lymphoid cells across 16 clusters.

(B & C) Relative frequencies of various T cell clusters as a proportion of all T and NK cells per replicate RM sample. Only cells with assigned hash calls are included.

(D) Mice were infected with 10^4 PFU IAV PR8 and RM tissue was collected to stain for T cells. Kruskal-Wallis, *p < 0.05, **p < 0.01.

(E) Relative frequencies of *Cd103*+ CD8 T cells as a proportion of all T cells, NK cells, and innate lymphocytes per OM replicate sample (left) and LNG replicate sample (right).

(F) Violin plot depicting a gene module score derived from the universal T_{RM} signature as published in (Milner et al., 2017) across all CD8 T cell clusters for cells collected from RM. Cohen's D for effect size is reported between *Ccr7*+ CD8 T cells and each other cluster. Welch's t test, *p < 0.05, **p < 0.01.

1353 (G) Dot plot of genes encoding for canonical surface markers, proteases, and transcription
1354 factors enriched or absent in T_{RM} cells from circulating memory and naïve CD8 T cells. Gene
1355 list derived from (Crowl et al., 2022).
1356

Figure 6

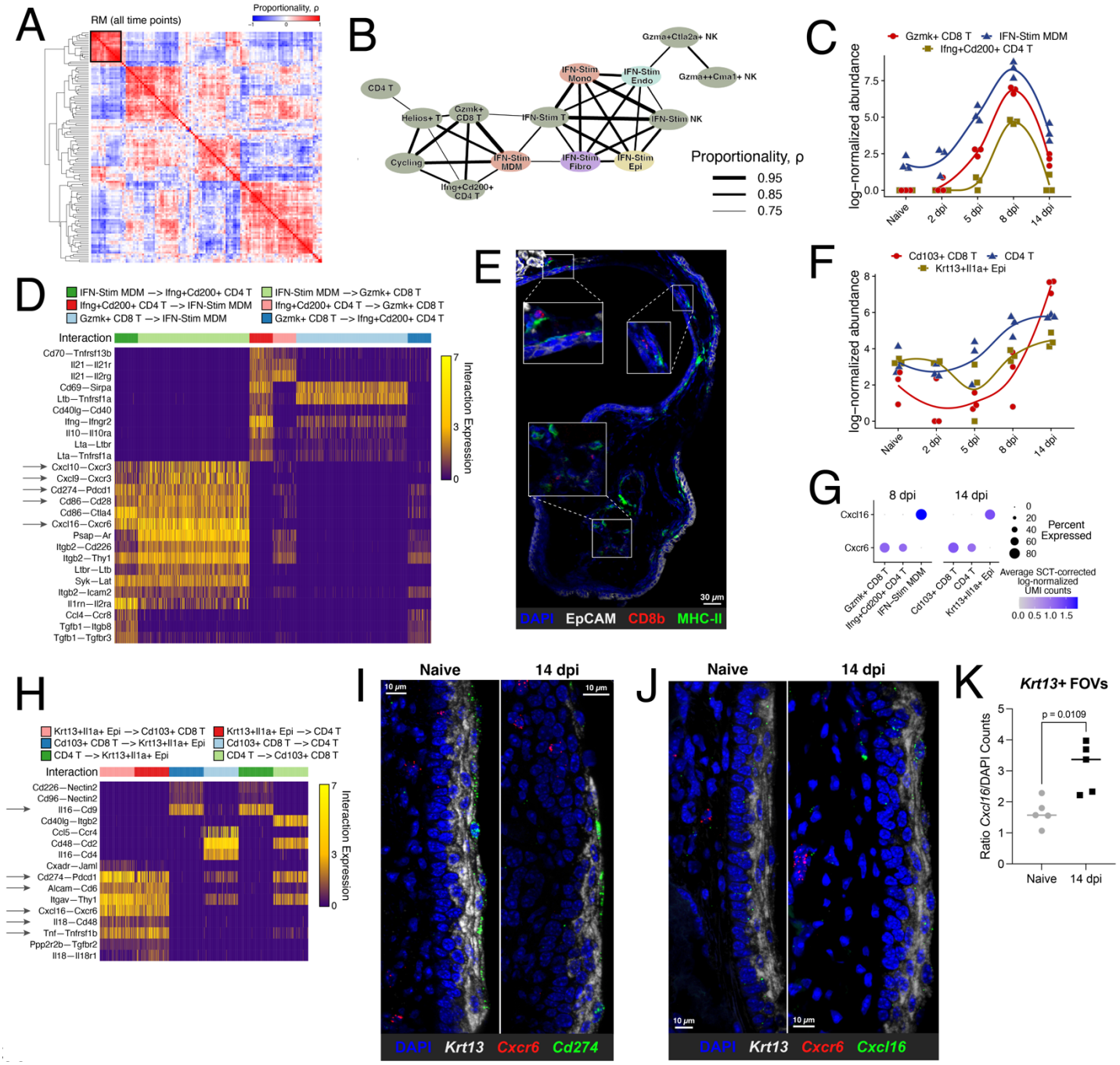

Figure 6: Proportionality and cell-cell communication analyses highlight the CXCL16–CXCR6 signaling pathway in T cell:MDM and T cell:KNIIFE cell interactions

(A) Hierarchically clustered similarity heatmap of sample replicate proportionality calculated across all RM primary infection time points. Black box surrounds the proportionality results for the cell clusters depicted in (B).

1363 (B) Network of significantly proportional (FDR<0.01) cell clusters as in (A). Nodes are colored by
1364 cell type and edge weight is representative of proportionality.
1365 (C) Abundance plot of *Gzmk*+ CD8 T cells, IFN-Stim MDMs, and *Ifng*+*Cd200*+ CD4 T cells in
1366 replicate RM samples. Smoothed lines are calculated using local polynomial regression
1367 fitting.
1368 (D) Heatmap depicting a subset of differentially expressed receptor-ligand interaction pairs
1369 between single-cell pairs identified by NICHES (Raredon et al., 2023) for the clusters
1370 depicted in (C); see **Supplementary Table 2**. Interaction expression is the multiplicative
1371 expression of receptor and ligand gene expression for each member of a single-cell pair. See
1372 for all receptor-ligand interaction pairs. Arrows highlight interactions described in the text.
1373 (E) Representative immunofluorescence imaging of maxillary turbinate at 8 dpi staining for
1374 EpCAM (gray), Cd8b (red), and MHC-II (green). White boxes show enlarged insets.
1375 (F) Abundance plot of *Cd103*+ CD8 T cells, CD4 T cells, and *Krt13*+*Il1a*+ epithelial (KNIIFE)
1376 cells in replicate RM samples.
1377 (G) Dot plot of scTransform-corrected log-normalized *Cxcl16* and *Cxcr6* expression 8 dpi (left) in
1378 the clusters depicted in (C) and 14 dpi (right) in the clusters depicted in (F).
1379 (H) Heatmap like (D) for the clusters shown in (F).
1380 (I) Representative RNAscope in situ staining for *Krt13* (gray)*, Cxcr6* (red)*, and Cd274* (i.e., PD-
1381 L1; green) of the nasal floor in a naïve mouse and 14 dpi mouse. Images depict a maximal
1382 intensity projection across 5 μm (10 slices) in the z-plane.
1383 (J) RNAscope as in (I) staining with *Krt13* (gray)*, Cxcl6* (red)*, and Cxcl16* (green).
1384 (K) Quantification of co-localization of *Krt13* and *Cxcl16* RNAs across multiple RNAscope
1385 images from the nasal floor (n = 5/timepoint). Ratio of the number of *Cxcl16* spots per nucleus
1386 within each *Krt13*+ region is reported. Welch's t test, *p < 0.05.

Figure 7

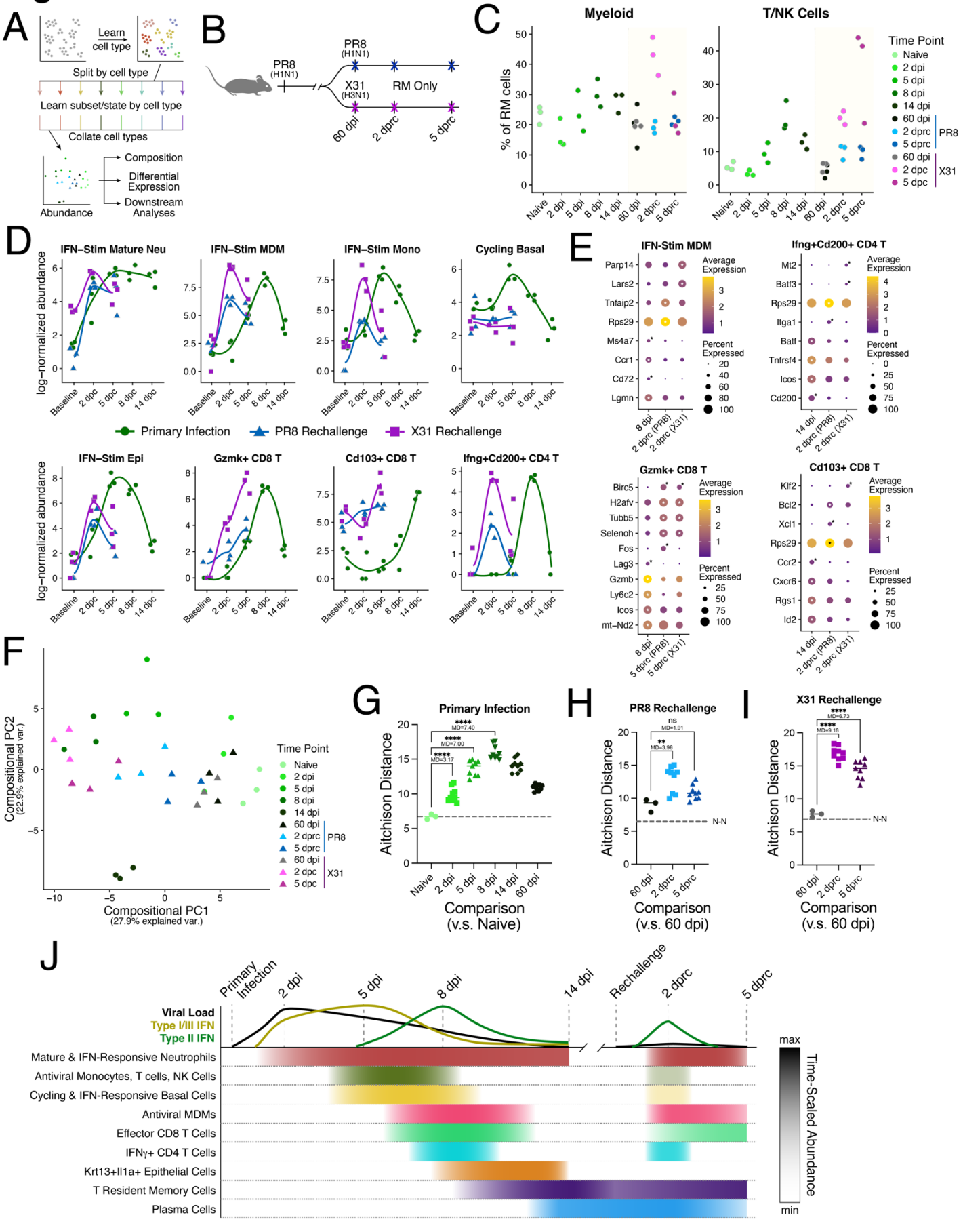
A
Learn cell type
Split by cell type
Learn subset/state by cell type
Collate cell types
Abundance
Composition
Differential Expression
Downstream Analyses
B
PR8 (H1N1)
PR8 (H1N1)
X31 (H3N1)
RM Only
60 dpi
2 dprc
5 dprc
C
Myeloid
T/NK Cells
% of RM cells
Time Point
Naive
2 dpi
5 dpi
8 dpi
14 dpi
60 dpi
2 dprc
5 dprc
PR8
60 dpi
2 dpc
5 dpc
X31
D
IFN–Stim Mature Neu
IFN–Stim MDM
IFN–Stim Mono
Cycling Basal
IFN–Stim Epi
Gzmk+ CD8 T
Cd103+ CD8 T
Ifng+Cd200+ CD4 T
log–normalized abundance
Baseline
2 dpc
5 dpc
8 dpc
14 dpc
Primary Infection
PR8 Rechallenge
X31 Rechallenge
E
IFN-Stim MDM
Ifng+Cd200+ CD4 T
Gzmk+ CD8 T
Cd103+ CD8 T
Average Expression
Percent Expressed
F
Compositional PC2 (22.9% explained var.)
Compositional PC1 (27.9% explained var.)
G
Primary Infection
Aitchison Distance
Comparison (v.s. Naive)
H
PR8 Rechallenge
Comparison (v.s. 60 dpi)
I
X31 Rechallenge
Comparison (v.s. 60 dpi)
J
Primary Infection
Rechallenge
Viral Load
Type I/III IFN
Type II IFN
Mature & IFN-Responsive Neutrophils
Antiviral Monocytes, T cells, NK Cells
Cycling & IFN-Responsive Basal Cells
Antiviral MDMs
Effector CD8 T Cells
IFNγ+ CD4 T Cells
Krt13+Il1a+ Epithelial Cells
T Resident Memory Cells
Plasma Cells
max
min
Time-Scaled Abundance

1388 **Figure 7: IAV rechallenge induces accelerated and coordinated memory immune**
1389 **responses**
1390 (A) Analysis scheme applied to RM samples to learn cell cluster identity.
1391 (B) Schema depicting experimental design for IAV rechallenge experiments. Mice previously
1392 infected with PR8 were administered either PR8 (H1N1) or X31 (H3N2) 60 dpi and RM was
1393 sampled prior to rechallenge, 2 and 5 days post rechallenge (dprc).
1394 (C) Relative frequencies of myeloid cells and T & NK cells as a proportion of all sequenced cells
1395 per RM replicate sample in primary infection and following rechallenge.
1396 (D) Abundance plots of various clusters showing overlaid primary infection (green) and
1397 rechallenge responses with PR8 in blue and X31 in pink. Baseline refers to samples from
1398 naïve mice in primary infection and to samples from 60 dpi in rechallenge. dpc = days post
1399 challenge. Smoothed lines are calculated using local polynomial regression fitting.
1400 (E) Dot plots depicting select cluster-specific and differentially expressed genes between primary
1401 infection and homologous and heterologous rechallenge in IFN-Stim MDMs (top left),
1402 *Ifng*+*Cd200*+ CD4 T cells (top right), *Gzmk*+ CD8 T cells (bottom left), and *Cd103*+ CD8 T
1403 cells (bottom right). Time points were chosen from peak responses in each challenge.
1404 Significantly enriched genes are labeled at each timepoint (*FDR<0.01). See
1405 **Supplementary Table 4** for all differentially expressed genes in each comparison.
1406 (F) Compositional PCA of primary infection and secondary challenge RM sample replicates.
1407 Here, secondary challenge samples were projected into the PC space calculated across only
1408 primary infection samples (see **Figure 2H**).
1409 (G, H, & I) Euclidean distances calculated between center log ratio transformed abundance values
1410 (Aitchison distance). The farther the Aitchison distance between two sample replicates, the
1411 less similar their compositions. (G) All pairs of naïve replicates and primary infection + 60 dpi
1412 replicates. (H) All pairs of 60 dpi replicates with matched PR8 rechallenge replicates. (I) All
1413 pairs of 60 dpi replicates with matched X31 rechallenge replicates. Dotted line plotted at the
1414 median naïve-naïve Aitchison distance (N-N). P values reported for multiple hypothesis
1415 corrected Welch's ANOVA. MD = mean difference; *p<0.05; **p<0.01; ***p<0.001, ****p<
1416 0.0001.
1417 (J) Timeline schematic of primary IAV infection and rechallenge depicting viral load trajectory,
1418 IFN dynamics, and immune and epithelial cell cluster response timing and duration.
1419

1420 ***SUPPLEMENTARY MATERIAL***

Figure S1

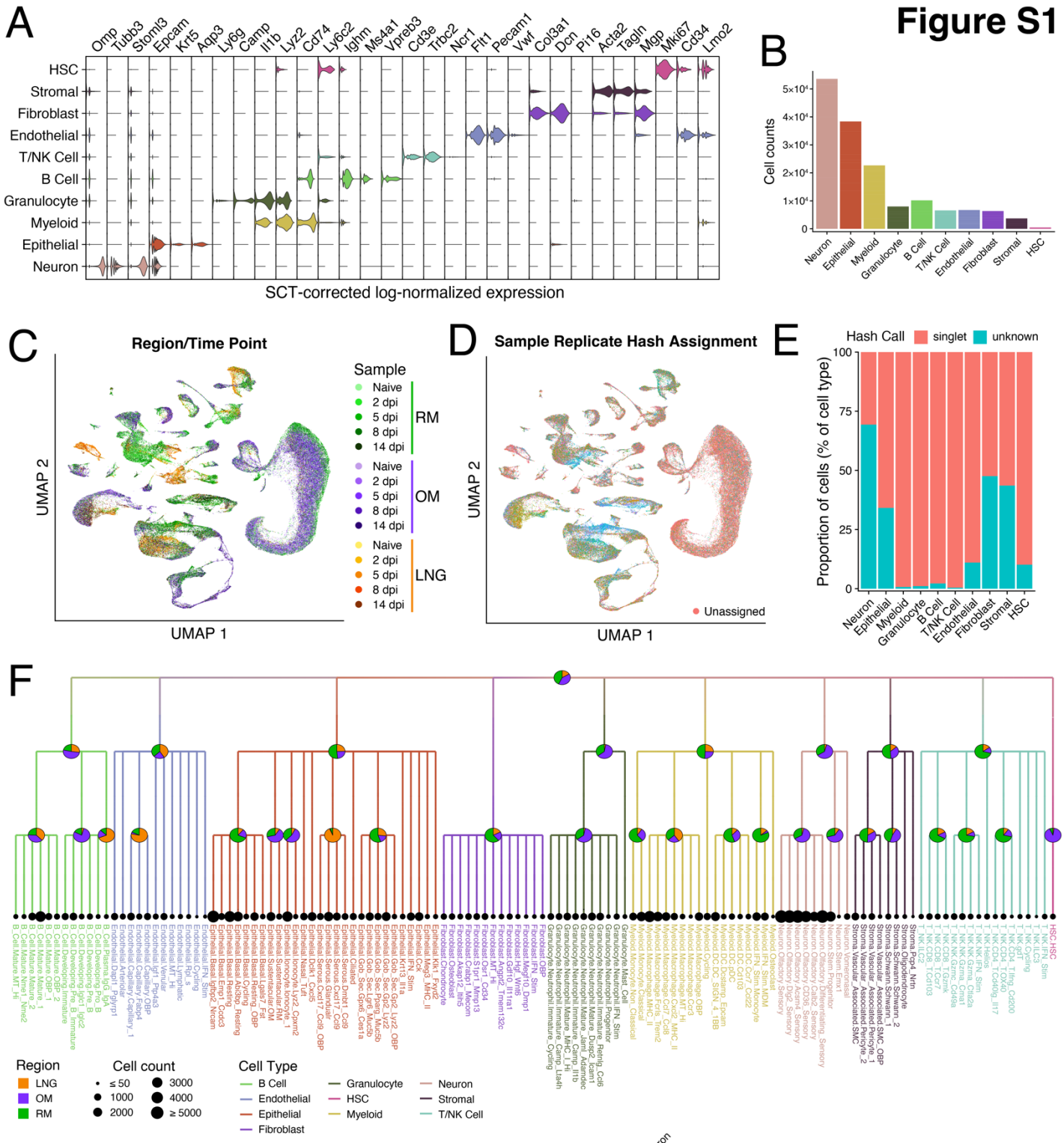
A
Omp
Tubb3
Stoml3
Epcam
Krt5
Aqp3
Ly6g
Camp
Il1b
Lyz2
Cd74
Ly6c2
Ighm
Ms4a1
Vpreb3
Cd3e
Tfbc2
Ncr1
Flt1
Pecam1
Vwf
Col3a1
Dcn
Pi16
Acta2
Tagln
Mgp
Mki67
Cd34
Lmo2
HSC
Stromal
Fibroblast
Endothelial
T/NK Cell
B Cell
Granulocyte
Myeloid
Epithelial
Neuron
SCT-corrected log-normalized expression
B
Cell counts
5×10⁴
4×10⁴
3×10⁴
2×10⁴
1×10⁴
0
Neuron
Epithelial
Myeloid
Granulocyte
B Cell
T/NK Cell
Endothelial
Fibroblast
Stromal
HSC
C
Region/Time Point
UMAP 2
UMAP 1
Sample
Naive
2 dpi
5 dpi
8 dpi
14 dpi
RM
OM
LNG
D
Sample Replicate Hash Assignment
UMAP 2
UMAP 1
Unassigned
E
Hash Call
singlet
unknown
Proportion of cells (% of cell type)
100
75
50
25
0
Neuron
Epithelial
Myeloid
Granulocyte
B Cell
T/NK Cell
Endothelial
Fibroblast
Stromal
HSC
F
Region
LNG
OM
RM
Cell count
≤ 50
1000
2000
3000
4000
≥ 5000
Cell Type
B Cell
Endothelial
Epithelial
Fibroblast
Granulocyte
HSC
Myeloid
Neuron
Stromal
T/NK Cell
G
Compositional PC1 Loading
0.1
0.0
−0.1
Schwann 1
Dapl1+Polyrp1+ Endo
Igfbp2-Nrcam+ Basal
Dclk1+Cxcl5+ Epi
Jam1+Adamdec1+ Mature Neu
Dcstamp+EpCAM+ DC
Fabp4+ Capillary
Gzmc+Cd49a+ NK
Scgb-b27+Cck+ Epi
Cxcl17+Cd9+ Serous
OBP Macrophage
Compositional PC2 Loading
0.1
0.0
−0.1
−0.2
Vomeronasal Sensory Neuron
IFN-Stim Mature Neu
Chondrocyte
Meg3+MHC-II+ Epi
IFN-Stim Epi
CyclingBasal
Crabp1+Mecom+ Fibro
Cycling Endo
MHC-II+ Hi Mac
Glandular
HSC
Camp++Ltah4+ Immature Neu

1422 **Figure S1: Clustering and sample replicate assignment across nasal mucosa regions and**
1423 **cell types**
1424 (A) Violin plots of representative genes used to assign cell type identity to clusters.
1425 (B) Numbers of cells classified as each cell type across all samples, including cells that did not
1426 receive a hash call.
1427 (C) UMAP embedding as in **Figure 2A** colored by region and time point.
1428 (D) UMAP as in (D) colored by hash call assignment. There are 45 sample replicates across the
1429 dataset in addition to cells without definitive hash identities ("Unassigned").
1430 (E) Stacked bar chart depicting the relative proportion of cells with assigned sample replicate
1431 identity (i.e., hash call) by cell type. Singlet = single sample replicate call; unknown = too few
1432 barcodes measured to assign a sample replicate identity.
1433 (F) Cell lineage tree generated with ARBOL (Zheng et al., 2023) depicting all 127 clusters found
1434 in the dataset through cell type subclustering. Branches are colored by cell type. Pie charts
1435 at each branching point depict the relative proportion of cells from each nasal mucosa region.
1436 Dot size at each end node is proportional to the number of cells assigned to that cluster. See
1437 **Supplementary Table 1** for all differentially expressed markers across clusters within each
1438 cell type.
1439 (G) Cell cluster abundance loadings from the PCA shown in **Figure 2C** for PC1 (left) and PC2
1440 (right) from (F). Cell cluster names for several of the most negative and most positive weights
1441 for each PC are depicted.
1442

Figure S2

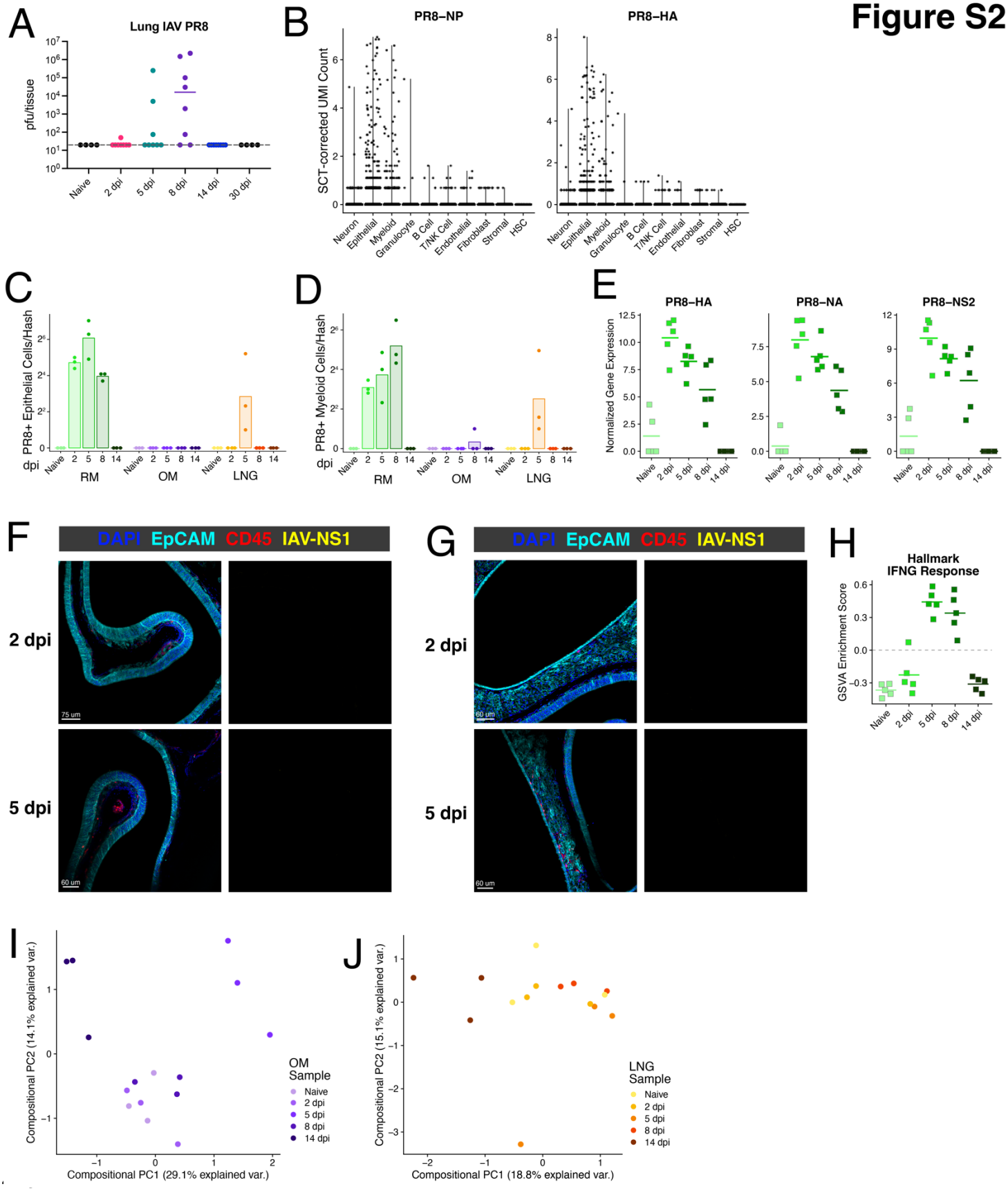
A
Lung IAV PR8
pfu/tissue
Naive
2 dpi
5 dpi
8 dpi
14 dpi
30 dpi
B
PR8–NP
PR8–HA
SCT-corrected UMI Count
Neuron
Epithelial
Myeloid
Granulocyte
B Cell
T/NK Cell
Endothelial
Fibroblast
Stromal
HSC
C
PR8+ Epithelial Cells/Hash
dpi
RM
OM
LNG
D
PR8+ Myeloid Cells/Hash
E
PR8–HA
PR8–NA
PR8–NS2
Normalized Gene Expression
F
DAPI EpCAM CD45 IAV-NS1
2 dpi
5 dpi
75 um
60 um
G
H
Hallmark
IFNG Response
GSVA Enrichment Score
I
Compositional PC2 (14.1% explained var.)
Compositional PC1 (29.1% explained var.)
OM
Sample
J
Compositional PC2 (15.1% explained var.)
Compositional PC1 (18.8% explained var.)
LNG
Sample

1444 **Figure S2: Viral transcript capture, global antiviral responses, and changes in OM and LNG**
1445 **composition**
1446 (A) Infectious IAV PR8 quantification in plaque forming units (pfu) of the entire lung.
1447 (B) scTransform-corrected UMI counts for the IAV PR8 genes encoding NP (left) and HA (right)
1448 by cell type.
1449 (C & D) Number of PR8+ epithelial cells (D) and myeloid cells (E) by time point and region. PR8+
1450 cells are classified by having at least 2 UMI aligning to PR8 genes.
1451 (E) Log-normalized expression of PR8 genes in bulk RNA-seq samples generated from whole
1452 RM tissue lysate (n = 5/timepoint).
1453 (F & G) Representative images of IAV infection in OM (E) and LNG (F) taken from mice 2 dpi (top)
1454 and 5 dpi (bottom). Staining for EpCAM (teal), CD45 (red), and IAV-NS1 (yellow). Images on
1455 the right depict only the signal in the IAV-NS1 channel.
1456 (H) Gene Set Variation Analysis (GSVA) Enrichment score for Hallmark Response to Interferon-
1457 Gamma on total RM tissue lysate bulk RNA-seq data (n = 5/time point)
1458 (I & J) Compositional PCA of only OM samples (I) and only LNG samples (J).
1459

Figure S3

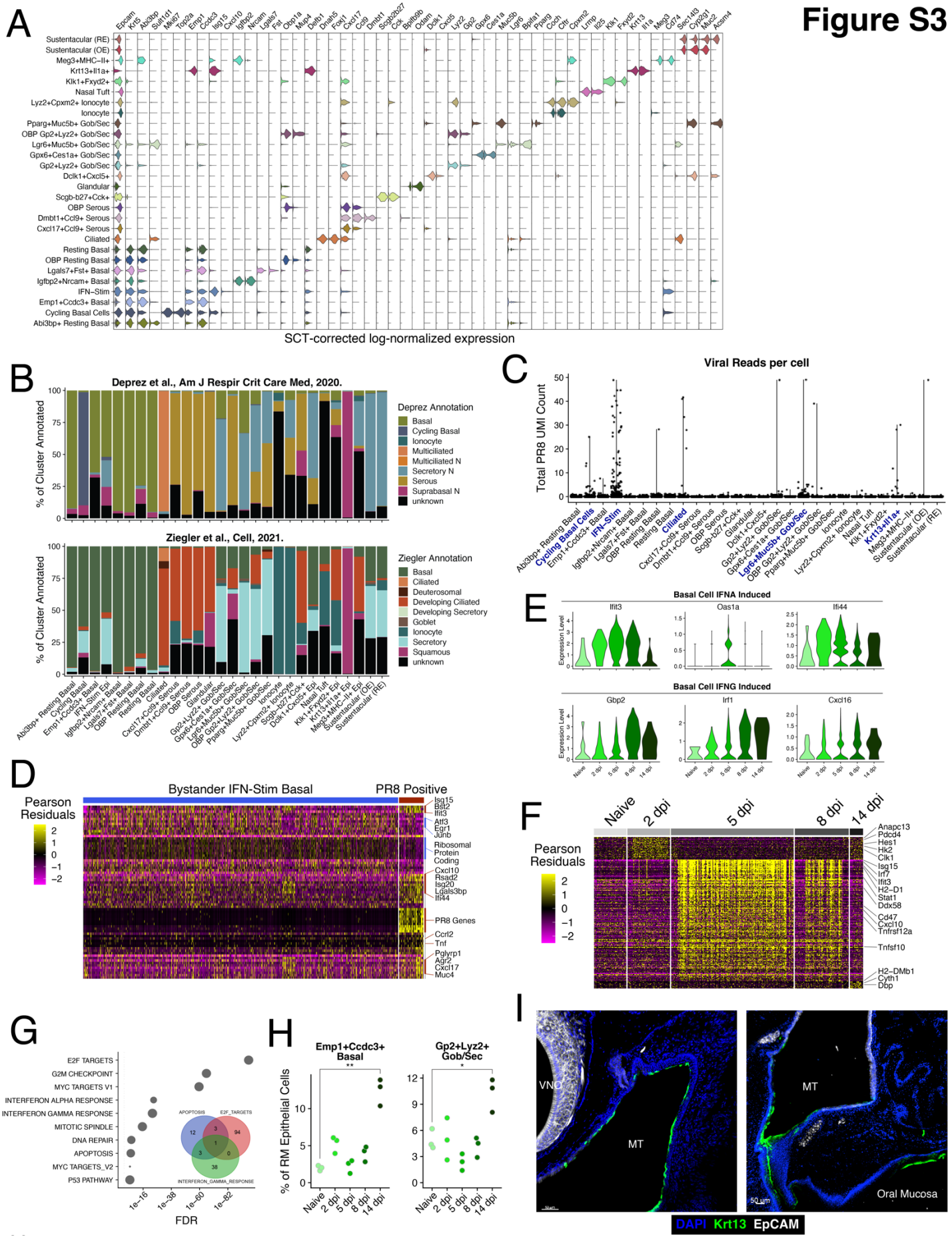
A
SCT-corrected log-normalized expression
B
Deprez et al., Am J Respir Crit Care Med, 2020.
% of Cluster Annotated
Deprez Annotation
Basal
Cycling Basal
Ionocyte
Multiciliated
Multiciliated N
Secretory N
Serous
Suprabasal N
unknown
Ziegler et al., Cell, 2021.
Ziegler Annotation
Basal
Ciliated
Deuterosomal
Developing Ciliated
Developing Secretory
Goblet
Ionocyte
Secretory
Squamous
unknown
C
Viral Reads per cell
Total PR8 UMI Count
D
Bystander IFN-Stim Basal
PR8 Positive
Pearson Residuals
PR8 Genes
E
Basal Cell IFNA Induced
Basal Cell IFNG Induced
Expression Level
F
Naive
2 dpi
5 dpi
8 dpi
14 dpi
Pearson Residuals
G
FDR
H
Emp1+Ccdc3+ Basal
Gp2+Lyz2+ Gob/Sec
% of RM Epithelial Cells
I
VNO
MT
Oral Mucosa
DAPI Krt13 EpCAM

1461 **Figure S3: Epithelial cell heterogeneity and response cluster dynamics**

1462 (A) Violin plots depicting differentially expressed marker genes (FDR<0.01) across all 28
1463 epithelial clusters (see **Supplementary Table 1**).

1464 (B) Stacked bar charts depicting the relative proportions of mouse nasal mucosa epithelial cells
1465 annotated for each human nasal epithelial cell type from (Deprez et al., 2020) and (Ziegler
1466 et al., 2021) by label transfer. Cells with poor assignments (maximum prediction score < 0.4)
1467 were labeled as "unknown".

1468 (C) Summative scTransform-corrected UMI counts across all 8 IAV genes by epithelial cell
1469 cluster. Clusters with ≥5 cells with more than 2 PR8 UMIs have their cluster names bolded
1470 in blue.

1471 (D) Heatmap depicting all differentially expressed genes between PR8 positive (≥2 PR8 UMIs)
1472 and bystander IFN-Stim epithelial cells from RM 5 and 8 dpi. Scaled Pearson residuals from
1473 scTransform are plotted.

1474 (E) Expression in IFN-Stim epithelial cells of representative IFNα and IFNγ induced ISGs from
1475 the stimulation signatures derived from airway basal cell cultures (Ziegler et al., 2020).

1476 (F) Heatmap depicting all differentially expressed genes (FDR<0.01) in Cycling Basal cells from
1477 RM between timepoints. Scaled Pearson residuals from scTransform are plotted.

1478 (G) Gene set analysis (hypergeometric test) of all differentially enriched genes in Cycling Basal
1479 cells compared to all other epithelial cell clusters (FDR<0.01). The Hallmark pathways from
1480 MsigDB (v7.5.1) were used. Inset: venn diagram showing the number genes that are within
1481 the Hallmark Apoptosis, E2F Targets, and Interferon Gamma Response pathways.

1482 (H) Relative frequencies of *Emp1*+*Ccdc3*+ basal cells (top) and *Gp2*+*Lyz2*+ Gob/Sec cells
1483 (bottom) as a proportion of all epithelial cells per replicate RM sample. Only cells with
1484 assigned hash calls are included. Welch's t test, *p < 0.05, **p < 0.01.

1485 (I) Representative immunofluorescence images of the nasal mucosa 14 dpi taken more
1486 posterior than **Figure 3K** where the nasal mucosa connects to the oral cavity.

1487

Figure S4

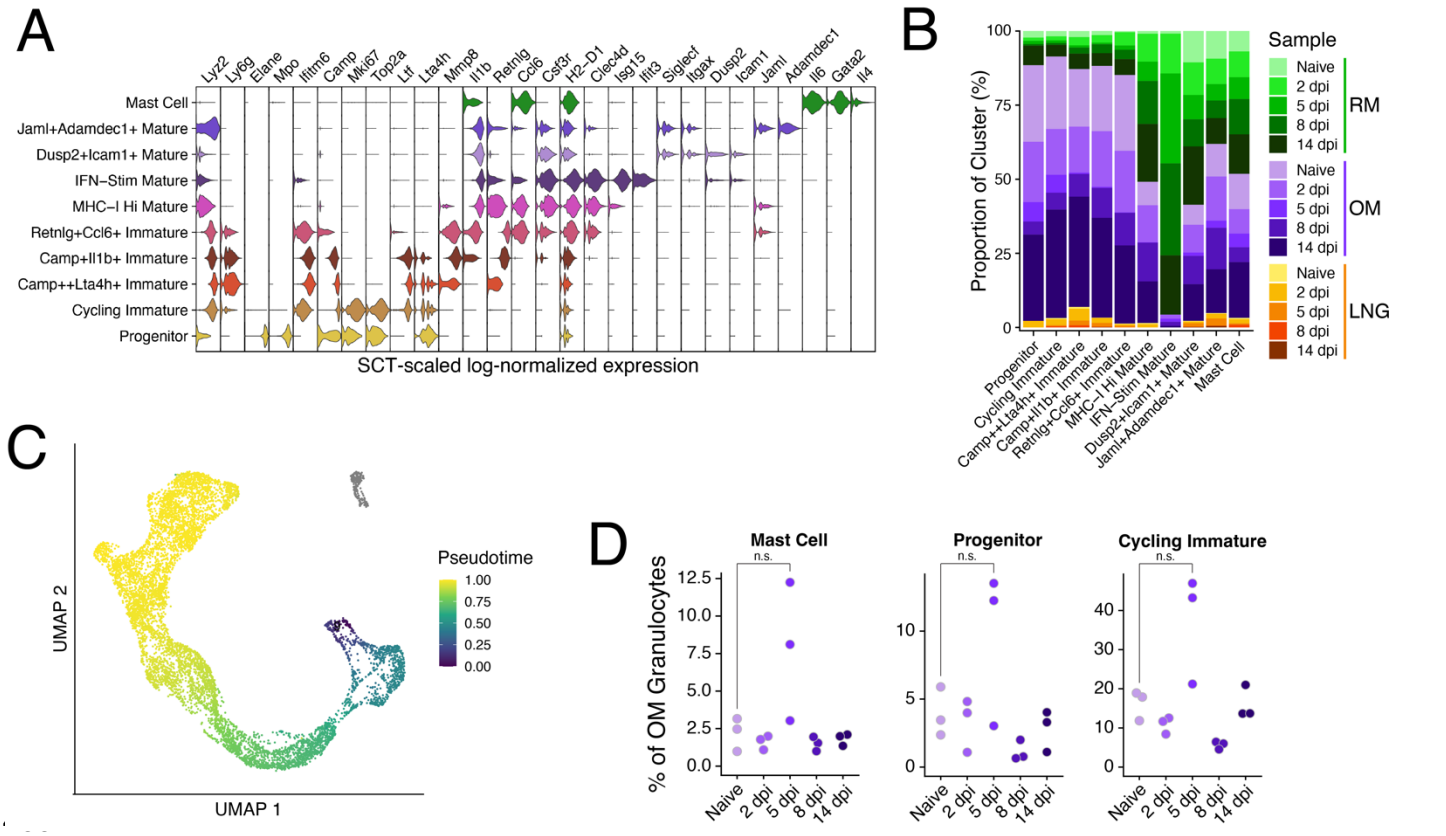

Figure S4: Granulocyte heterogeneity

(A) Violin plots depicting differentially expressed marker genes (FDR<0.01) across all 10 granulocyte clusters (see **Supplementary Table 1**).

(B) Stacked bar chart depicting the relative proportions of cells annotated for each granulocyte cluster by region and time point.

(C) UMAP of granulocytes colored by pseudotime. Mast Cells were not included in the pseudotime analysis and are colored gray.

(D) Relative frequencies of Mast cells (left), progenitors (center), and cycling immature (right) as a proportion of all granulocytes per replicate OM sample.

Figure S5

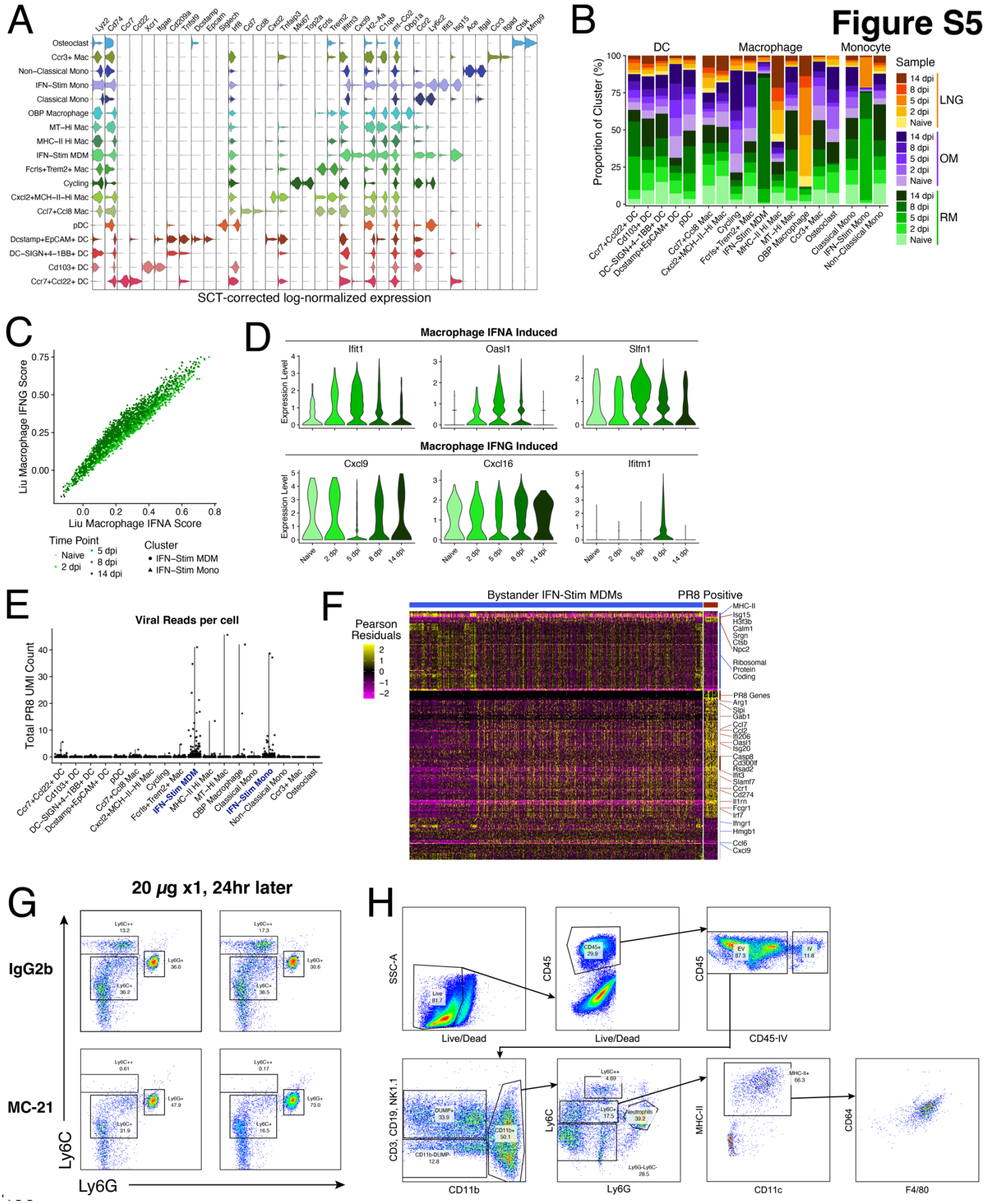
A
SCT-corrected log-normalized expression
B
DC
Macrophage
Monocyte
Proportion of Cluster (%)
Sample
LNG
OM
RM
C
Liu Macrophage IFNG Score
Liu Macrophage IFNA Score
Time Point
Cluster
D
Macrophage IFNA Induced
Macrophage IFNG Induced
Expression Level
E
Viral Reads per cell
Total PR8 UMI Count
F
Bystander IFN-Stim MDMs
PR8 Positive
Pearson Residuals
G
20 μg x1, 24hr later
IgG2b
MC-21
Ly6C
Ly6G
H
SSC-A
Live/Dead
CD45
CD45-IV
CD3, CD19, NK1.1
CD11b
Ly6C
Ly6G
MHC-II
CD11c
CD64
F4/80

1500 **Figure S5: Myeloid heterogeneity, viral+ cells, and monocyte depletion**

1501 (A) Violin plots depicting differentially expressed marker genes (FDR<0.01) across all 18
1502 macrophage, monocyte, and DC clusters (see **Supplementary Table 1**).

1503 (B) Stacked bar chart depicting the relative proportions of cells annotated for each myeloid
1504 cluster by region and time point.

1505 (C) IFN-Stim monocyte and MDM scores for signatures derived from bone marrow-derived
1506 macrophage cultures stimulated with IFNα or IFNγ (Liu et al., 2012).

1507 (D) Expression in representative IFNα and IFNγ induced ISGs from (C).

1508 (E) Summative scTransform-corrected UMI counts across all 8 IAV genes by myeloid cell cluster.
1509 Clusters with ≥5 cells with more than 2 PR8 UMIs have their cluster names bolded in blue.

1510 (F) Heatmap depicting all differentially expressed genes between PR8 positive (≥2 PR8 UMIs)
1511 and bystander IFN-Stim MDMs from RM 8 dpi. Scaled Pearson residuals from scTransform
1512 are plotted.

1513 (G) Mice (n = 4) were treated i.p. with control antibody (top) or anti-CCR2 antibody (bottom) and
1514 blood was collected 24 hours later for flow cytometry. Pre-gated on Dead–CD45+CD3–
1515 CD19–CD11b+.

1516 (H) Representative gating scheme for Ly6C+ and Ly6C++ monocytes in the nasal mucosa.

1517

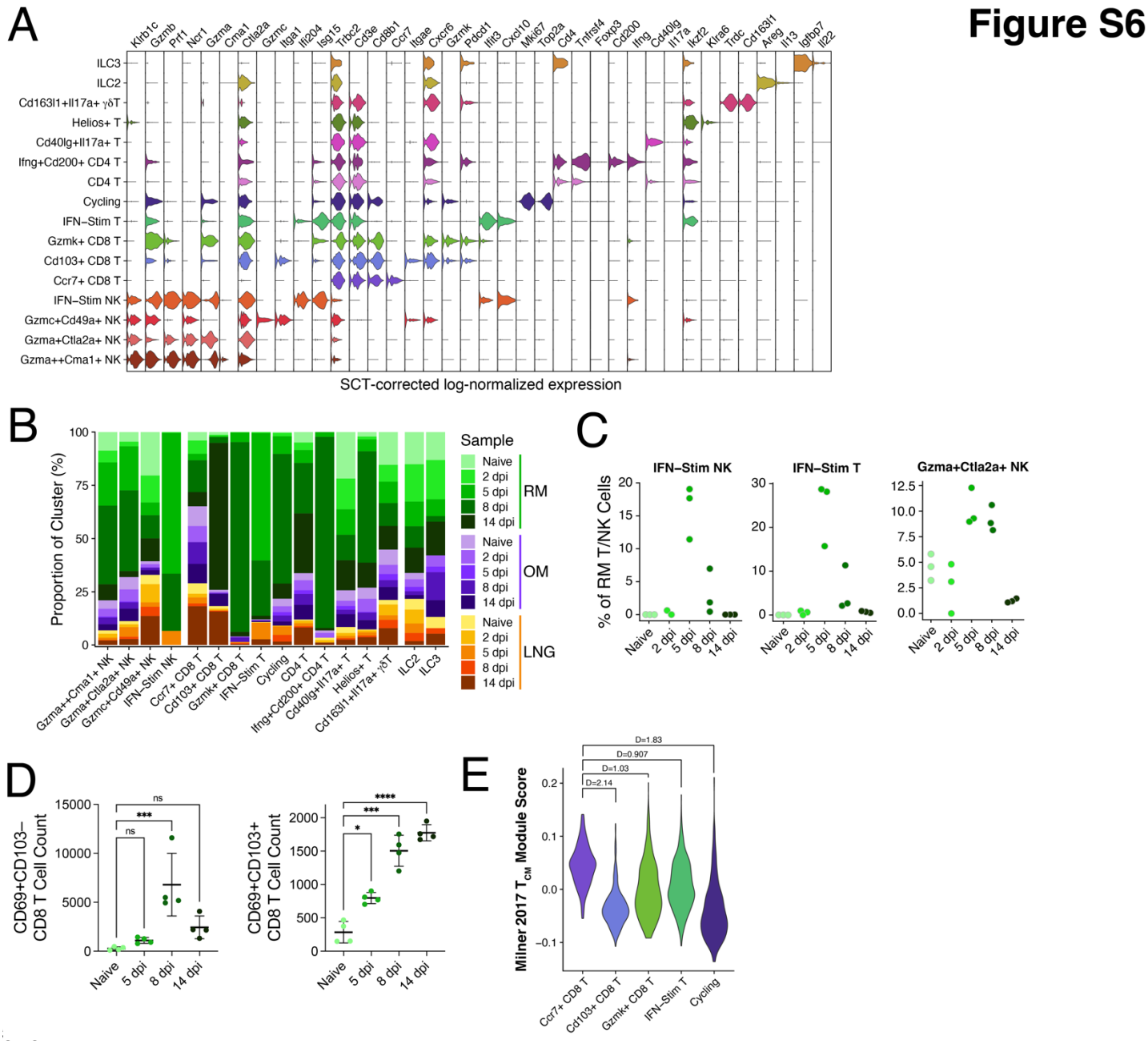

Figure S6: T cell, NK cell, and innate lymphocyte heterogeneity and T_{RM} responses

(A) Violin plots depicting differentially expressed marker genes (FDR<0.01) across all 16 T cell, NK cell, and innate lymphocyte cell clusters (see **Supplementary Table 1**).

(B) Stacked bar chart depicting the relative proportions of cells annotated for each myeloid cluster by region and time point.

(C) Relative frequencies of IFN-Stim NK cells (left), IFN-Stim T cells (middle), and *Gzma+Ctla2a+* NK cells (right) as a proportion of all T cells, NK cells, and innate lymphocytes per RM replicate sample.

1527 (D) Mice were infected with 10^4 PFU IAV PR8 and RM tissue was collected to stain for T cells.
1528 Kruskal-Wallis, *p < 0.05, **p < 0.01.
1529 (E) Violin plot depicting a gene module score derived from the universal T circulating memory
1530 (T_{CM}) cell signature as published in (Milner et al., 2017) across all CD8 T cell clusters.
1531 Cohen's D for effect size is reported between *Ccr7*+ CD8 T cells and each other cluster.
1532

Figure S7

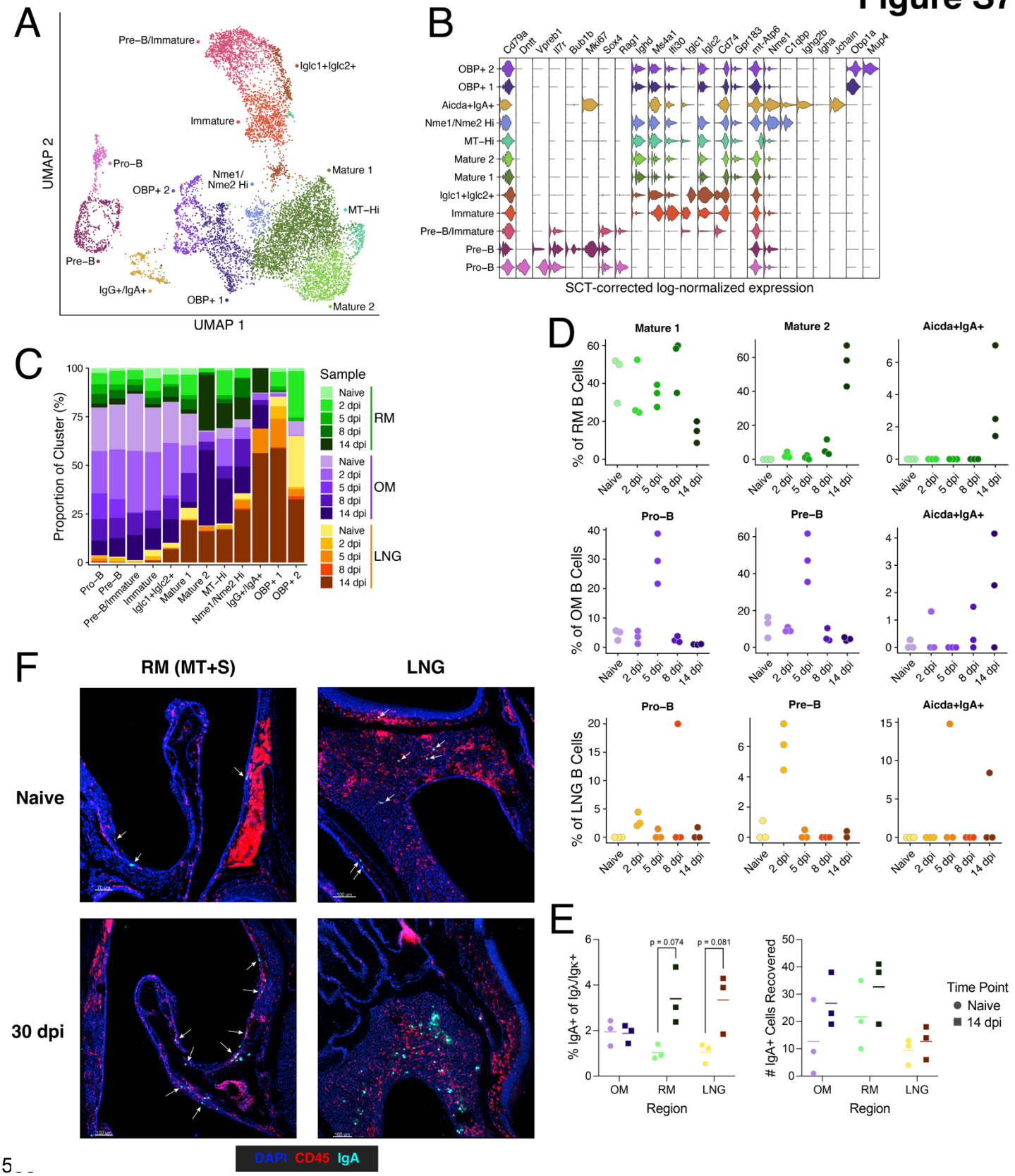
A
Pre–B/Immature
Igl1+Igl2+
Immature
Pro–B
Nme1/
Nme2 Hi
OBP+ 2
Mature 1
MT–Hi
Pre–B
IgG+/IgA+
OBP+ 1
Mature 2
UMAP 2
UMAP 1
B
Cd79a
Dntt
Vpreb1
Il7r
Bub1b
Mki67
Sox4
Rag1
Ighd
Ms4a1
Ifi30
Iglc1
Iglc2
Cd74
Gpr183
mt-Atp6
Nme1
C1qbp
Ighg2b
Igha
Jchain
Obp1a
Mup4
OBP+ 2
OBP+ 1
Aicda+IgA+
Nme1/Nme2 Hi
MT–Hi
Mature 2
Mature 1
Igl1+Igl2+
Immature
Pre–B/Immature
Pre–B
Pro–B
SCT-corrected log-normalized expression
C
Proportion of Cluster (%)
Sample
Naive
2 dpi
5 dpi
8 dpi
14 dpi
RM
OM
LNG
Pro–B
Pre–B
Pre–B/Immature
Immature
Igl1+Igl2+
Mature 1
Mature 2
MT–Hi
Nme1/Nme2 Hi
IgG+/IgA+
OBP+ 1
OBP+ 2
D
Mature 1
Mature 2
Aicda+IgA+
Pro–B
Pre–B
Aicda+IgA+
Pro–B
Pre–B
Aicda+IgA+
% of RM B Cells
% of OM B Cells
% of LNG B Cells
Naive
2 dpi
5 dpi
8 dpi
14 dpi
E
% IgA+ of Igλ/Igκ+
p = 0.074
p = 0.081
OM
RM
LNG
Region
IgA+ Cells Recovered
Time Point
Naive
14 dpi
F
RM (MT+S)
LNG
Naive
30 dpi
DAPI CD45 IgA

15

1534 **Figure S7: B cell heterogeneity and cluster dynamics**

1535 (A) UMAP embedding of 10,167 B cells across 12 clusters.

1536 (B) Violin plots depicting differentially expressed marker genes (FDR<0.01) across all 12 B cell
1537 clusters (see **Supplementary Table 1**).

1538 (C) Stacked bar chart depicting the relative proportions of cells annotated for each B cell cluster
1539 by region and time point.

1540 (D) Relative frequencies of several B cell clusters as proportions of all B cells per RM replicate
1541 sample (top), OM replicate sample (middle), and LNG replicate sample (bottom).

1542 (E) Mice were infected with 10^4 PFU IAV PR8 and RM, OM, and LNG tissue were collected to
1543 stain intracellularly for IgA cells. Welch's t test.

1544 (F) Representative immunofluorescence images staining for IgA producing cells in the RM (left)
1545 and LNG (right) in naïve mice (top) and 30 dpi (bottom). White arrows point to IgA+ cells in
1546 the sparser images.

1547

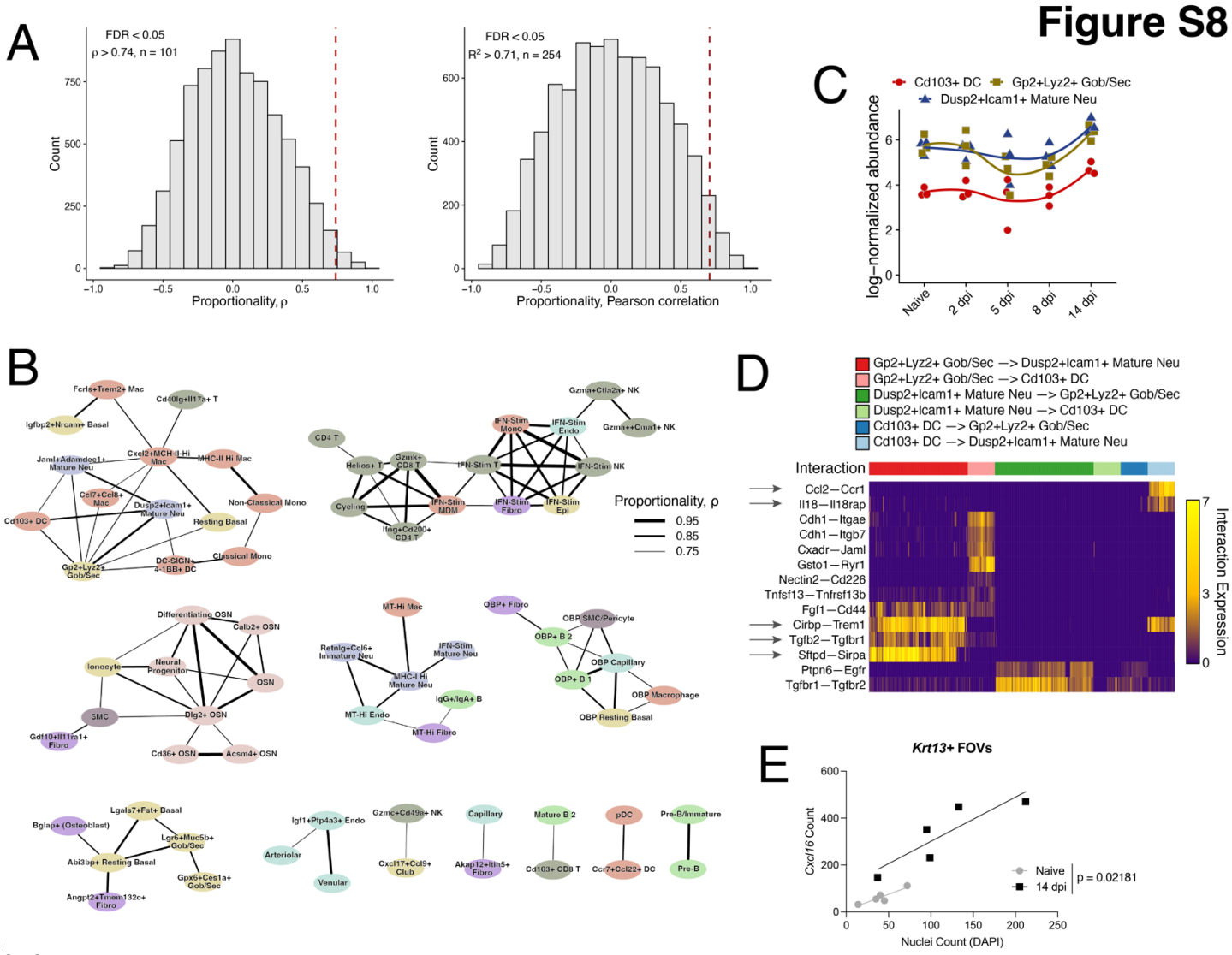

Figure S8: Proportionality and cell-cell communication analysis

(A) Histograms of calculated proportionality (left) and Pearson correlation (right) statistics across all RM sample replicates. The significance cutoff (FDR<0.05) for each statistic is marked by the red dashed line and was calculated from a background of 1000 permutations of the data.

(B) Network of all significantly proportional (FDR<0.01) cell clusters across all RM replicate samples. Nodes are colored by cell type and edge weight is representative of proportionality.

(C) Abundance plot of *Cd103+* DCs, *Gp2+Lyz2+* Gob/Sec cells, and *Dusp2+Icam1+* Mature Neutrophils in replicate RM samples. Smoothed lines are calculated using local polynomial regression fitting.

(D) Heatmap depicting a subset of differentially expressed receptor-ligand interaction pairs between single-cell pairs identified by NICHES (Raredon et al., 2023) for the clusters depicted in (C); see **Supplementary Table 2**. Interaction expression is the multiplicative

1561 expression of receptor and ligand gene expression for each member of a single-cell pair.
1562 Arrows highlight interactions described in the text.
1563 (E) Quantification of nuclei and *Cxcl16* spots within *Krt13*+ regions of interest across 10
1564 RNAscope images in a naïve mouse and 14 dpi (n = 5/timepoint). Linear regression, p value
1565 reported for difference in intercepts.
1566

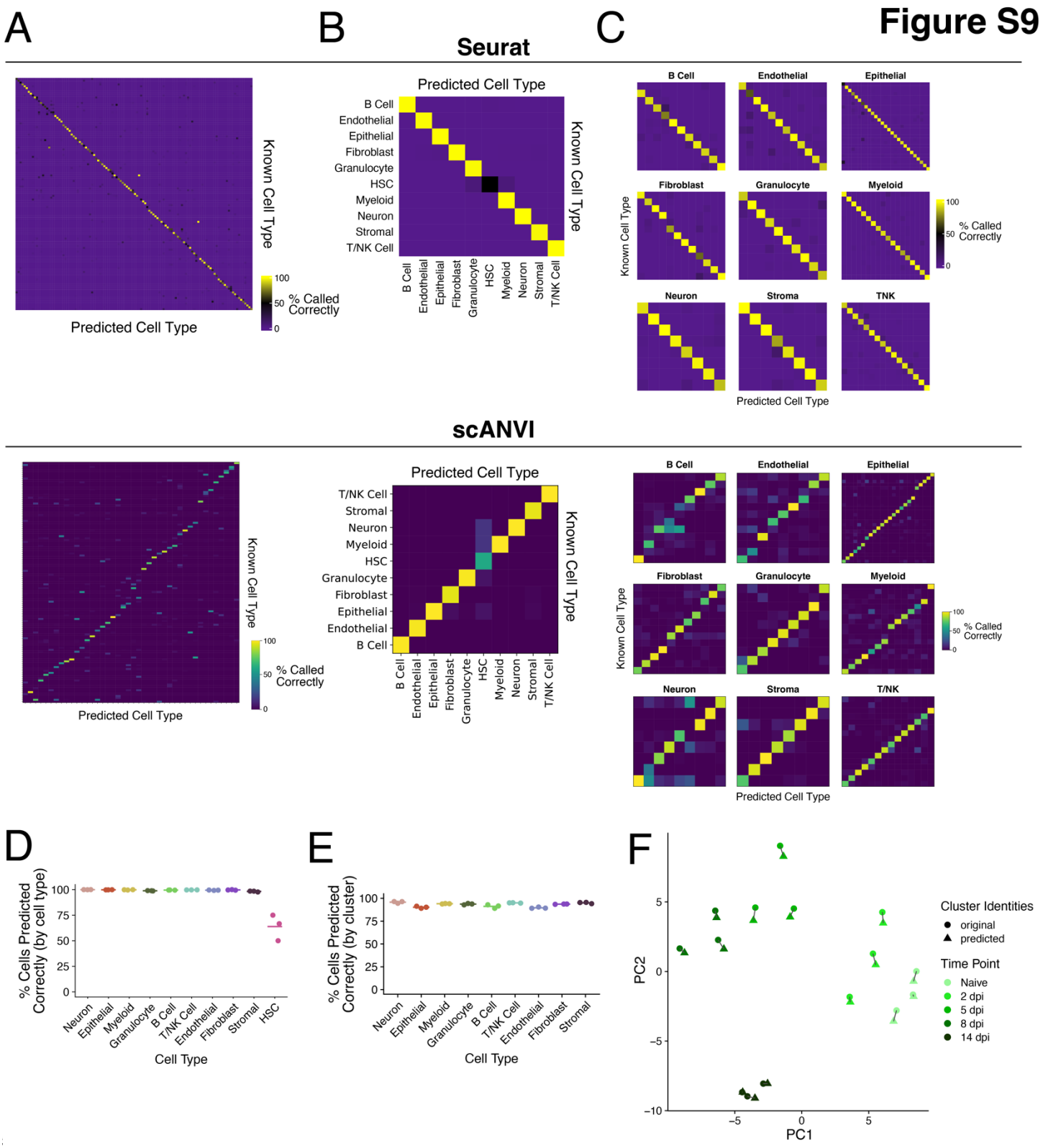

Figure S9: Validating label transfer methods to assign cell cluster identities to new nasal mucosa samples

Initially, one sample replicate per timepoint was separated from the RM dataset to be used as a query trained using a reference made from the remaining sample replicates and unclassified cells. The top and bottom depict results from Seurat and scANVI respectively.

(A) Heatmaps depicting the per-cluster on-target prediction frequency when calculated across all 127 cluster labels.

(B) Heatmaps depicting the per-cell-type on-target prediction frequency when calculated across the 9 cell type labels.

(C) After predicting cell type labels, new query and reference pairs were generated within each cell type and label transfer was performed within each. Heatmaps depicting the per-cluster on-target prediction frequency when calculated within all clusters within each respective cell type.

Following comparison of Seurat and scANVI, the label transfer approach was reiterated two more times in Seurat using other sets of replicates as the query and reference datasets.

(D) Percentage of cells with an accurate cell type label by cell type. Each dot reflects a distinct query+reference comparison.

(E) Percentage of cells with an accurate cluster label by cell type. Each dot reflects a distinct query+reference comparison.

(F) Compositional PCA from **Figure 2I** where the query sample replicates were projected using the predicted cell cluster labels. Lines connect the query predicted sample compositions to their matching compositions as determined by the initial clustering and labeling.

Figure S10

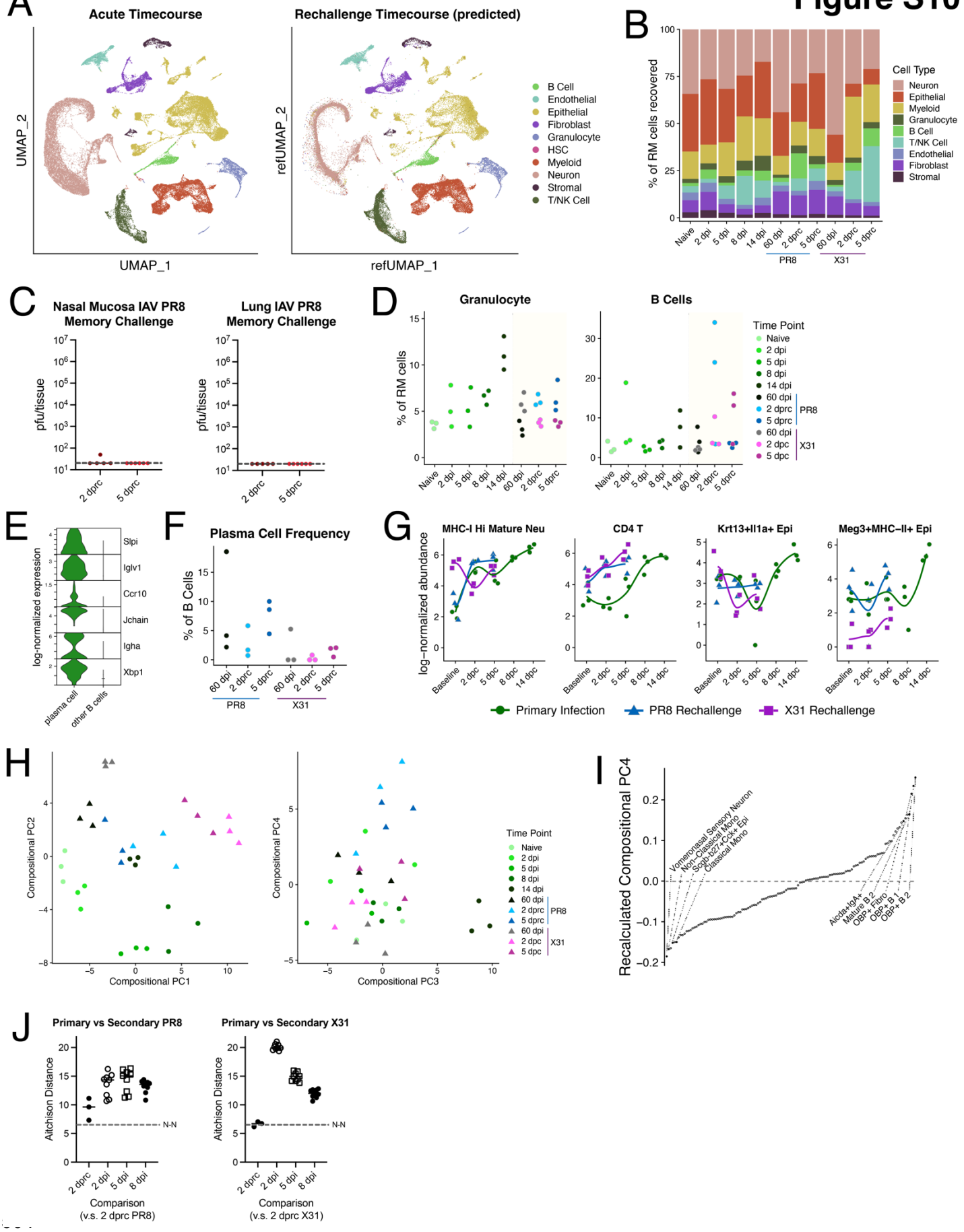

A
Acute Timecourse
Rechallenge Timecourse (predicted)
UMAP_2
UMAP_1
refUMAP_2
refUMAP_1
B Cell
Endothelial
Epithelial
Fibroblast
Granulocyte
HSC
Myeloid
Neuron
Stromal
T/NK Cell
B
% of RM cells recovered
Cell Type
Neuron
Epithelial
Myeloid
Granulocyte
B Cell
T/NK Cell
Endothelial
Fibroblast
Stromal
Naive
2 dpi
5 dpi
8 dpi
14 dpi
60 dpi
2 dprc
5 dprc
PR8
X31
C
Nasal Mucosa IAV PR8 Memory Challenge
Lung IAV PR8 Memory Challenge
pfu/tissue
2 dprc
5 dprc
D
Granulocyte
B Cells
% of RM cells
Time Point
Naive
2 dpi
5 dpi
8 dpi
14 dpi
60 dpi
2 dprc
5 dprc
PR8
60 dpi
2 dpc
5 dpc
X31
E
log-normalized expression
Slpi
Iglv1
Ccr10
Jchain
Igha
Xbp1
plasma cell
other B cells
F
Plasma Cell Frequency
% of B Cells
60 dpi
2 dprc
5 dprc
PR8
X31
G
MHC-I Hi Mature Neu
CD4 T
Krt13+Il1a+ Epi
Meg3+MHC−II+ Epi
log−normalized abundance
Baseline
2 dpc
5 dpc
8 dpc
14 dpc
Primary Infection
PR8 Rechallenge
X31 Rechallenge
H
Compositional PC2
Compositional PC1
Compositional PC4
Compositional PC3
Time Point
Naive
2 dpi
5 dpi
8 dpi
14 dpi
60 dpi
2 dprc
5 dprc
PR8
60 dpi
2 dpc
5 dpc
X31
I
Recalculated Compositional PC4
Vomeronasal Sensory Neuron
Non−Classical Mono
Scgb−b27+Cck+ Epi
Classical Mono
Aicda+IgA+
Mature B 2
OBP+ Fibro
OBP+ B 1
OBP+ B 2
J
Primary vs Secondary PR8
Primary vs Secondary X31
Aitchison Distance
N-N
2 dprc
2 dpi
5 dpi
8 dpi
Comparison
(v.s. 2 dprc PR8)
Comparison
(v.s. 2 dprc X31)

1592 **Figure S10: Changes in RM composition following secondary challenge**

1593 (A) UMAP of all RM cells from the primary infection dataset (left) and the projected UMAP of all
1594 cells in the rechallenge dataset (right) colored by cell type.

1595 (B) Stacked bar chart depicting the relative proportions of cells annotated for each cell type by
1596 time point. Cells from RM samples only.

1597 (C) Infectious IAV PR8 quantification in pfu of the entire nasal mucosa (left) and lung (right)
1598 during IAV PR8 rechallenge.

1599 (D) Relative frequencies of granulocytes and B cells as a proportion of all sequenced cells per
1600 RM replicate sample in primary infection and following rechallenge.

1601 (E) Violin plot of select plasma cell specific/enriched genes (FDR corrected p-values $\leq 10^{-118}$ by
1602 1-vs-rest Wilcoxon Rank Sum Test).

1603 (F) Relative frequency of the plasma cell cluster as proportions of all B cells per RM replicate in
1604 rechallenge. Plasma cells were not found in the primary infection dataset.

1605 (G) Abundance plots of various clusters showing overlaid primary infection (green) and
1606 rechallenge responses with PR8 in blue and X31 in pink. Baseline refers to samples from
1607 naïve mice in primary infection and to samples from 60 dpi in rechallenge. dpc = days post
1608 challenge. Smoothed lines are calculated using local polynomial regression fitting.

1609 (H) Compositional PCA recalculated using both primary infection and secondary challenge RM
1610 sample replicates. PCs 1-2 (left) and 3-4 (right).

1611 (I) Cell cluster abundance loadings for PC3 (E). Cell cluster names for several of the most
1612 negative and most positive weights for each PC are depicted.

1613 (J) Heatmap depicting all pairwise Aitchison distances between all RM sample replicates.

1614

1615 **Supplementary Table 1: Differentially expressed genes across clusters within each cell**
1616 **type.** Differential expression analysis was performed across cells from all samples within each
1617 cell type using the Wilcoxon Rank Sum test.

1618

1619 **Supplementary Table 2: Cell cluster counts per sample replicate across all regions and**
1620 **time points.** Annotated counts for each sample replicate across all 127 clusters in the dataset.
1621 Abundances per sample, and the total number of cells recovered per reaction are also reported.

1622

1623 **Supplementary Table 3: Differentially expressed receptor-ligand pairs identified by**
1624 **NICHES.** Within each NICHES analysis, differential expression was performed across all cell-
1625 pairs at the specific timepoint of interest using the ROC test built into Seurat. See **Figure 6**.

1626

1627 **Supplementary Table 4: Differentially expressed genes between primary infection and**
1628 **secondary challenge.** Differential expression analysis ("bidomal" test) was performed between
1629 timepoints using cells from RM only within the specified clusters in **Figure 7E**.

1630

REFERENCES

Adamson, M. S., Nesic, S., Buness, A., Bayrak, K., Schmitz, S., Soler, S., Zillinger, T., Marx, S., Lambing, S., Andryka-Cegielski, K., et al. (2022). RIG-I activation primes and trains innate antiviral immune memory. 2022.10.27.514004.

Aegerter, H., Kulikauskaite, J., Crotta, S., Patel, H., Kelly, G., Hessel, E. M., Mack, M., Beinke, S. and Wack, A. (2020). Influenza-induced monocyte-derived alveolar macrophages confer prolonged antibacterial protection. *Nat Immunol* 21, 145–157.

Aitchison, J., Barceló-Vidal, C., Martín-Fernández, J. A. and Pawlowsky-Glahn, V. (2000). Logratio Analysis and Compositional Distance. *Mathematical Geology* 32, 271–275.

Angerer, P., Haghverdi, L., Büttner, M., Theis, F. J., Marr, C. and Buettner, F. (2016). destiny: diffusion maps for large-scale single-cell data in R. *Bioinformatics* 32, 1241–1243.

Ariotti, S., Hogenbirk, M. A., Dijkgraaf, F. E., Visser, L. L., Hoekstra, M. E., Song, J.-Y., Jacobs, H., Haanen, J. B. and Schumacher, T. N. (2014). Skin-resident memory CD8+ T cells trigger a state of tissue-wide pathogen alert. *Science* 346, 101–105.

Bastard, P., Rosen, L. B., Zhang, Q., Michailidis, E., Hoffmann, H.-H., Zhang, Y., Dorgham, K., Philippot, Q., Rosain, J., Béziat, V., et al. (2020). Autoantibodies against type I IFNs in patients with life-threatening COVID-19. *Science* 370,.

Bastard, P., Zhang, Q., Zhang, S.-Y., Jouanguy, E. and Casanova, J.-L. (2022). Type I interferons and SARS-CoV-2: from cells to organisms. *Current Opinion in Immunology* 74, 172–182.

Bosch, A. A. T. M., Biesbroek, G., Trzcinski, K., Sanders, E. A. M. and Bogaert, D. (2013). Viral and Bacterial Interactions in the Upper Respiratory Tract. *PLOS Pathogens* 9, e1003057.

Bosch-Camós, L., Alonso, U., Esteve-Codina, A., Chang, C.-Y., Martín-Mur, B., Accensi, F., Muñoz, M., Navas, M. J., Dabad, M., Vidal, E., et al. (2022). Cross-protection against African swine fever virus upon intranasal vaccination is associated with an adaptive-innate immune crosstalk. *PLOS Pathogens* 18, e1010931.

Boudreau, C. M. and Alter, G. (2019). Extra-Neutralizing FcR-Mediated Antibody Functions for a Universal Influenza Vaccine. *Frontiers in Immunology* 10,.

Bouvier, N. M. and Lowen, A. C. (2010). Animal Models for Influenza Virus Pathogenesis and Transmission. *Viruses* 2, 1530–1563.

Boyd, D. F., Allen, E. K., Randolph, A. G., Guo, X. J., Weng, Y., Sanders, C. J., Bajracharya, R., Lee, N. K., Guy, C. S., Vogel, P., et al. (2020). Exuberant fibroblast activity compromises lung function via ADAMTS4. *Nature* 587, 466–471.

Brandes, M., Klauschen, F., Kuchen, S. and Germain, R. N. (2013). A Systems Analysis Identifies a Feedforward Inflammatory Circuit Leading to Lethal Influenza Infection. *Cell* 154, 197–212.

1668 Brann, D. H., Tsukahara, T., Weinreb, C., Lipovsek, M., Van den Berge, K., Gong, B., Chance,
1669 R., Macaulay, I. C., Chou, H.-J., Fletcher, R. B., et al. (2020). Non-neuronal expression
1670 of SARS-CoV-2 entry genes in the olfactory system suggests mechanisms underlying
1671 COVID-19-associated anosmia. *Science Advances* 6, eabc5801.

1672 Broggi, A., Ghosh, S., Sposito, B., Spreafico, R., Balzarini, F., Cascio, A. L., Clementi, N.,
1673 Santis, M. D., Mancini, N., Granucci, F., et al. (2020). Type III interferons disrupt the lung
1674 epithelial barrier upon viral recognition. *Science* 369, 706–712.

1675 Büttner, M., Ostner, J., Müller, C. L., Theis, F. J. and Schubert, B. (2021). scCODA is a
1676 Bayesian model for compositional single-cell data analysis. *Nat Commun* 12, 6876.

1677 Cao, Y., Lin, Y., Ormerod, J. T., Yang, P., Yang, J. Y. H. and Lo, K. K. (2019). scDC: single cell
1678 differential composition analysis. *BMC Bioinformatics* 20, 721.

1679 Chapman, T. J. and Topham, D. J. (2010). Identification of a Unique Population of Tissue-
1680 Memory CD4+ T Cells in the Airways after Influenza Infection That Is Dependent on the
1681 Integrin VLA-1. *The Journal of Immunology* 184, 3841–3849.

1682 Chen, X., Liu, S., Goraya, M. U., Maarouf, M., Huang, S. and Chen, J.-L. (2018). Host Immune
1683 Response to Influenza A Virus Infection. *Front Immunol* 9, 320.

1684 Chen, K., Zhang, J., Huang, Y., Tian, X., Yang, Y. and Dong, A. (2022). Single-cell RNA-seq
1685 transcriptomic landscape of human and mouse islets and pathological alterations of
1686 diabetes. *iScience* 25, 105366.

1687 Clark, S. E. (2020). Commensal bacteria in the upper respiratory tract regulate susceptibility to
1688 infection. *Current Opinion in Immunology* 66, 42–49.

1689 Clark, R. A., Chong, B., Mirchandani, N., Brinster, N. K., Yamanaka, K., Dowgiert, R. K. and
1690 Kupper, T. S. (2006). The Vast Majority of CLA+ T Cells Are Resident in Normal Skin1.
1691 *The Journal of Immunology* 176, 4431–4439.

1692 Costa-Martins, A. G., Mane, K., Lindsey, B. B., Ogava, R. L. T., Castro, Í., Jagne, Y. J., Sallah,
1693 H. J., Armitage, E. P., Jarju, S., Ahadzie, B., et al. (2021). Prior upregulation of interferon
1694 pathways in the nasopharynx impacts viral shedding following live attenuated influenza
1695 vaccine challenge in children. *Cell Reports Medicine* 2, 100465.

1696 Crowl, J. T., Heeg, M., Ferry, A., Milner, J. J., Omilusik, K. D., Toma, C., He, Z., Chang, J. T.
1697 and Goldrath, A. W. (2022). Tissue-resident memory CD8+ T cells possess unique
1698 transcriptional, epigenetic and functional adaptations to different tissue environments.
1699 *Nat Immunol* 23, 1121–1131.

1700 Dann, E., Henderson, N. C., Teichmann, S. A., Morgan, M. D. and Marioni, J. C. (2022).
1701 Differential abundance testing on single-cell data using k-nearest neighbor graphs. *Nat*
1702 *Biotechnol* 40, 245–253.

1703 Darrah, P. A., Zeppa, J. J., Maiello, P., Hackney, J. A., Wadsworth, M. H., Hughes, T. K.,
1704 Pokkali, S., Swanson, P. A., Grant, N. L., Rodgers, M. A., et al. (2020). Prevention of
1705 tuberculosis in macaques after intravenous BCG immunization. *Nature* 577, 95–102.

1706 Davis, J. D. and Wypych, T. P. (2021). Cellular and functional heterogeneity of the airway
1707 epithelium. *Mucosal Immunol* 14, 978–990.

1708 Denning, N.-L., Aziz, M., Murao, A., Gurien, S. D., Ochani, M., Prince, J. M. and Wang, P.
1709 (2020). Extracellular CIRP as an endogenous TREM-1 ligand to fuel inflammation in
1710 sepsis. *JCI Insight* 5,.

1711 Deprez, M., Zaragosi, L.-E., Truchi, M., Becavin, C., Ruiz García, S., Arguel, M.-J., Plaisant, M.,
1712 Magnone, V., Lebrigand, K., Abelanet, S., et al. (2020). A Single-Cell Atlas of the Human
1713 Healthy Airways. *Am J Respir Crit Care Med* 202, 1636–1645.

1714 Dumm, R. E., Wellford, S. A., Moseman, E. A. and Heaton, N. S. (2020). Heterogeneity of
1715 Antiviral Responses in the Upper Respiratory Tract Mediates Differential Non-lytic
1716 Clearance of Influenza Viruses. *Cell Reports* 32,.

1717 Fleming, S. J., Chaffin, M. D., Arduini, A., Akkad, A.-D., Banks, E., Marioni, J. C., Philippakis, A.
1718 A., Ellinor, P. T. and Babadi, M. (2022). Unsupervised removal of systematic background
1719 noise from droplet-based single-cell experiments using CellBender. 791699.

1720 Gardai, S. J., Xiao, Y.-Q., Dickinson, M., Nick, J. A., Voelker, D. R., Greene, K. E. and Henson,
1721 P. M. (2003). By Binding SIRPα or Calreticulin/CD91, Lung Collectins Act as Dual
1722 Function Surveillance Molecules to Suppress or Enhance Inflammation. *Cell* 115, 13–23.

1723 Gloor, G. B., Macklaim, J. M., Pawlowsky-Glahn, V. and Egozcue, J. J. (2017). Microbiome
1724 Datasets Are Compositional: And This Is Not Optional. *Frontiers in Microbiology* 8,.

1725 Grieshaber-Bouyer, R., Radtke, F. A., Cunin, P., Stifano, G., Levescot, A., Vijaykumar, B.,
1726 Nelson-Maney, N., Blaustein, R. B., Monach, P. A. and Nigrovic, P. A. (2021). The
1727 neutrotime transcriptional signature defines a single continuum of neutrophils across
1728 biological compartments. *Nat Commun* 12, 2856.

1729 Habibi, M. S., Thwaites, R. S., Chang, M., Jozwik, A., Paras, A., Kirsebom, F., Varese, A.,
1730 Owen, A., Cuthbertson, L., James, P., et al. (2020). Neutrophilic inflammation in the
1731 respiratory mucosa predisposes to RSV infection. *Science* 370,.

1732 Hao, Y., Hao, S., Andersen-Nissen, E., Mauck, W. M., Zheng, S., Butler, A., Lee, M. J., Wilk, A.
1733 J., Darby, C., Zager, M., et al. (2021). Integrated analysis of multimodal single-cell data.
1734 *Cell* 184, 3573-3587.e29.

1735 Harkema, J. R., Carey, S. A. and Wagner, J. G. (2006). The Nose Revisited: A Brief Review of
1736 the Comparative Structure, Function, and Toxicologic Pathology of the Nasal Epithelium.
1737 *Toxicol Pathol* 34, 252–269.

1738 Heim, T. A., Lin, Z., Steele, M. M., Mudianto, T. and Lund, A. W. (2023). CXCR6 promotes
1739 dermal CD8+ T cell survival and transition to long-term tissue residence.
1740 2023.02.14.528487.

1741 Hu, M.-W., Kim, D. W., Liu, S., Zack, D. J., Blackshaw, S. and Qian, J. (2019). PanoView: An
1742 iterative clustering method for single-cell RNA sequencing data. *PLOS Computational*
1743 *Biology* 15, e1007040.

1744 Hufford, M. M., Kim, T. S., Sun, J. and Braciale, T. J. (2015). The Effector T Cell Response to
1745 Influenza Infection. In *Influenza Pathogenesis and Control - Volume II* (ed. Oldstone, M.
1746 B. A.) and Compans, R. W.), pp. 423–455. Cham: Springer International Publishing.

1747 Ibricevic, A., Pekosz, A., Walter, M. J., Newby, C., Battaile, J. T., Brown, E. G., Holtzman, M. J.
1748 and Brody, S. L. (2006). Influenza Virus Receptor Specificity and Cell Tropism in Mouse
1749 and Human Airway Epithelial Cells. *Journal of Virology* 80, 7469–7480.

1750 Iijima, N. and Iwasaki, A. (2014). A local macrophage chemokine network sustains protective
1751 tissue-resident memory CD4 T cells. *Science* 346, 93–98.

1752 Iuliano, A. D., Roguski, K. M., Chang, H. H., Muscatello, D. J., Palekar, R., Tempia, S., Cohen,
1753 C., Gran, J. M., Schanzer, D., Cowling, B. J., et al. (2018). Estimates of global seasonal
1754 influenza-associated respiratory mortality: a modelling study. *Lancet* 391, 1285–1300.

1755 Iwasaki, A. and Medzhitov, R. (2015). Control of adaptive immunity by the innate immune
1756 system. *Nat. Immunol.* 16, 343–353.

1757 Jiang, X., Clark, R. A., Liu, L., Wagers, A. J., Fuhlbrigge, R. C. and Kupper, T. S. (2012). Skin
1758 infection generates non-migratory memory CD8+ TRM cells providing global skin
1759 immunity. *Nature* 483, 227–231.

1760 Johansson, C. and Kirsebom, F. C. M. (2021). Neutrophils in respiratory viral infections.
1761 *Mucosal Immunol* 14, 815–827.

1762 Johnson, P. R., Feldman, S., Thompson, J. M., Mahoney, J. D. and Wright, P. F. (1986).
1763 Immunity to Influenza A Virus Infection in Young Children: A Comparison of Natural
1764 Infection, Live Cold-Adapted Vaccine, and Inactivated Vaccine. *The Journal of Infectious*
1765 *Diseases* 154, 121–127.

1766 Johnson Jr., P. R., Feldman, S., Thompson, J. M., Mahoney, J. D. and Wright, P. F. (1985).
1767 Comparison of long-term systemic and secretory antibody responses in children given
1768 live, attenuated, or inactivated influenza A vaccine. *Journal of Medical Virology* 17, 325–
1769 335.

1770 Jung, S.-H., Hwang, B.-H., Shin, S., Park, E.-H., Park, S.-H., Kim, C. W., Kim, E., Choo, E.,
1771 Choi, I. J., Swirski, F. K., et al. (2022). Spatiotemporal dynamics of macrophage
1772 heterogeneity and a potential function of Trem2hi macrophages in infarcted hearts. *Nat*
1773 *Commun* 13, 4580.

1774 Kadoki, M., Patil, A., Thaiss, C. C., Brooks, D. J., Pandey, S., Deep, D., Alvarez, D., Andrian, U.
1775 H. von, Wagers, A. J., Nakai, K., et al. (2017). Organism-Level Analysis of Vaccination
1776 Reveals Networks of Protection across Tissues. *Cell* 171, 398-413.e21.

1777 Kaufmann, E., Sanz, J., Dunn, J. L., Khan, N., Mendonça, L. E., Pacis, A., Tzelepis, F., Pernet,
1778 E., Dumaine, A., Grenier, J.-C., et al. (2018). BCG Educates Hematopoietic Stem Cells
1779 to Generate Protective Innate Immunity against Tuberculosis. *Cell* 172, 176-190.e19.

1780 Kim, Y.-M. and Shin, E.-C. (2021). Type I and III interferon responses in SARS-CoV-2 infection.
1781 *Exp Mol Med* 53, 750–760.

1782 Klinkhammer, J., Schnepf, D., Ye, L., Schwaderlapp, M., Gad, H. H., Hartmann, R., Garcin, D.,
1783 Mahlakõiv, T. and Staeheli, P. (2018). IFN-λ prevents influenza virus spread from the
1784 upper airways to the lungs and limits virus transmission. *eLife* 7, e33354.

1785 Kochs, G., García-Sastre, A. and Martínez-Sobrido, L. (2007). Multiple Anti-Interferon Actions of
1786 the Influenza A Virus NS1 Protein. *J Virol* 81, 7011–7021.

1787 Krammer, F. (2019). The human antibody response to influenza A virus infection and
1788 vaccination. *Nat Rev Immunol* 19, 383–397.

1789 Lavelle, E. C. and Ward, R. W. (2022). Mucosal vaccines — fortifying the frontiers. *Nat Rev*
1790 *Immunol* 22, 236–250.

1791 Li, B., Gould, J., Yang, Y., Sarkizova, S., Tabaka, M., Ashenberg, O., Rosen, Y., Slyper, M.,
1792 Kowalczyk, M. S., Villani, A.-C., et al. (2020). Cumulus provides cloud-based data
1793 analysis for large-scale single-cell and single-nucleus RNA-seq. *Nat Methods* 17, 793–
1794 798.

1795 Li, H., Wang, X., Wang, Y., Zhang, M., Hong, F., Wang, H., Cui, A., Zhao, J., Ji, W. and Chen,
1796 Y.-G. (2022). Cross-species single-cell transcriptomic analysis reveals divergence of cell
1797 composition and functions in mammalian ileum epithelium. *Cell Regeneration* 11, 19.

1798 Li, J., Hubisz, M. J., Earlie, E. M., Duran, M. A., Hong, C., Varela, A. A., Lettera, E., Deyell, M.,
1799 Tavora, B., Havel, J. J., et al. (2023). Non-cell-autonomous cancer progression from
1800 chromosomal instability. *Nature* 620, 1080–1088.

1801 Liew, F., Talwar, S., Cross, A., Willett, B. J., Scott, S., Logan, N., Siggins, M. K., Swieboda, D.,
1802 Sidhu, J. K., Efstathiou, C., et al. (2023). SARS-CoV-2-specific nasal IgA wanes 9
1803 months after hospitalisation with COVID-19 and is not induced by subsequent
1804 vaccination. *eBioMedicine* 87,.

1805 Lin, H. and Peddada, S. D. (2020). Analysis of microbial compositions: a review of normalization
1806 and differential abundance analysis. *npj Biofilms Microbiomes* 6, 1–13.

1807 Linderman, G. C., Zhao, J., Roulis, M., Bielecki, P., Flavell, R. A., Nadler, B. and Kluger, Y.
1808 (2022). Zero-preserving imputation of single-cell RNA-seq data. *Nat Commun* 13, 192.

1809 Liu, S.-Y., Sanchez, D. J., Aliyari, R., Lu, S. and Cheng, G. (2012). Systematic identification of
1810 type I and type II interferon-induced antiviral factors. *Proceedings of the National*
1811 *Academy of Sciences* 109, 4239–4244.

1812 Lovell, D., Pawlowsky-Glahn, V., Egozcue, J. J., Marguerat, S. and Bähler, J. (2015).
1813 Proportionality: A Valid Alternative to Correlation for Relative Data. *PLOS Computational*
1814 *Biology* 11, e1004075.

1815 Mack, M., Cihak, J., Simonis, C., Luckow, B., Proudfoot, A. E. I., Plachý, J., Brühl, H., Frink, M.,
1816 Anders, H.-J., Vielhauer, V., et al. (2001). Expression and Characterization of the
1817 Chemokine Receptors CCR2 and CCR5 in Mice1. *The Journal of Immunology* 166,
1818 4697–4704.

1819 MacLean, A. J., Richmond, N., Koneva, L., Attar, M., Medina, C. A. P., Thornton, E. E., Gomes,
1820 A. C., El-Turabi, A., Bachmann, M. F., Rijal, P., et al. (2022). Secondary influenza
1821 challenge triggers resident memory B cell migration and rapid relocation to boost
1822 antibody secretion at infected sites. *Immunity* 55, 718-733.e8.

1823 Major, J., Crotta, S., Llorian, M., McCabe, T. M., Gad, H. H., Priestnall, S. L., Hartmann, R. and
1824 Wack, A. (2020). Type I and III interferons disrupt lung epithelial repair during recovery
1825 from viral infection. *Science* 369, 712–717.

1826 Manicassamy, B., Manicassamy, S., Belicha-Villanueva, A., Pisanelli, G., Pulendran, B. and
1827 García-Sastre, A. (2010). Analysis of in vivo dynamics of influenza virus infection in mice
1828 using a GFP reporter virus. *PNAS* 107, 11531–11536.

1829 Mao, T., Israelow, B., Peña-Hernández, M. A., Suberi, A., Zhou, L., Luyten, S., Reschke, M.,
1830 Dong, H., Homer, R. J., Saltzman, W. M., et al. (2022). Unadjuvanted intranasal spike
1831 vaccine elicits protective mucosal immunity against sarbecoviruses. *Science* 378,
1832 eabo2523.

1833 Matsuoka, Y., Lamirande, E. W. and Subbarao, K. (2009). The mouse model for influenza. *Curr*
1834 *Protoc Microbiol* Chapter 15, Unit 15G.3.

1835 McMaster, S. R., Wilson, J. J., Wang, H. and Kohlmeier, J. E. (2015). Airway-Resident Memory
1836 CD8 T Cells Provide Antigen-Specific Protection against Respiratory Virus Challenge
1837 through Rapid IFN-γ Production. *The Journal of Immunology* 195, 203–209.

1838 Milner, J. J., Toma, C., Yu, B., Zhang, K., Omilusik, K., Phan, A. T., Wang, D., Getzler, A. J.,
1839 Nguyen, T., Crotty, S., et al. (2017). Runx3 programs CD8+ T cell residency in non-
1840 lymphoid tissues and tumours. *Nature* 552, 253–257.

1841 Montoro, D. T., Haber, A. L., Biton, M., Vinarsky, V., Lin, B., Birket, S. E., Yuan, F., Chen, S.,
1842 Leung, H. M., Villoria, J., et al. (2018). A revised airway epithelial hierarchy includes
1843 CFTR-expressing ionocytes. *Nature* 560, 319–324.

1844 Morens, D. M., Taubenberger, J. K. and Fauci, A. S. (2023). Rethinking next-generation
1845 vaccines for coronaviruses, influenzaviruses, and other respiratory viruses. *Cell Host &*
1846 *Microbe* 31, 146–157.

1847 Morgan, A. J., Guillen, C., Symon, F. A., Birring, S. S., Campbell, J. J. and Wardlaw, A. J.
1848 (2008). CXCR6 identifies a putative population of retained human lung T cells
1849 characterised by co-expression of activation markers. *Immunobiology* 213, 599–608.

1850 Moriyama, M., Chen, I.-Y., Kawaguchi, A., Koshiba, T., Nagata, K., Takeyama, H., Hasegawa,
1851 H. and Ichinohe, T. (2016). The RNA- and TRIM25-Binding Domains of Influenza Virus
1852 NS1 Protein Are Essential for Suppression of NLRP3 Inflammasome-Mediated
1853 Interleukin-1β Secretion. *Journal of Virology* 90, 4105–4114.

1854 Ols, S., Yang, L., Thompson, E. A., Pushparaj, P., Tran, K., Liang, F., Lin, A., Eriksson, B.,
1855 Karlsson Hedestam, G. B., Wyatt, R. T., et al. (2020). Route of Vaccine Administration
1856 Alters Antigen Trafficking but Not Innate or Adaptive Immunity. *Cell Reports* 30, 3964-
1857 3971.e7.

1858 Onodera, T., Takahashi, Y., Yokoi, Y., Ato, M., Kodama, Y., Hachimura, S., Kurosaki, T. and
1859 Kobayashi, K. (2012). Memory B cells in the lung participate in protective humoral
1860 immune responses to pulmonary influenza virus reinfection. *Proceedings of the National*
1861 *Academy of Sciences* 109, 2485–2490.

1862 Ordovas-Montanes, J., Dwyer, D. F., Nyquist, S. K., Buchheit, K. M., Vukovic, M., Deb, C.,
1863 Wadsworth, M. H., Hughes, T. K., Kazer, S. W., Yoshimoto, E., et al. (2018). Allergic
1864 inflammatory memory in human respiratory epithelial progenitor cells. *Nature* 560, 649.

1865 Ordovas-Montanes, J., Beyaz, S., Rakoff-Nahoum, S. and Shalek, A. K. (2020). Distribution and
1866 storage of inflammatory memory in barrier tissues. *Nat Rev Immunol* 1–13.

1867 Park, A. and Iwasaki, A. (2020). Type I and Type III Interferons – Induction, Signaling, Evasion,
1868 and Application to Combat COVID-19. *Cell Host Microbe* 27, 870–878.

1869 Patterson-Cross, R. B., Levine, A. J. and Menon, V. (2021). Selecting single cell clustering
1870 parameter values using subsampling-based robustness metrics. *BMC Bioinformatics* 22,
1871 39.

1872 Pizzolla, A., Nguyen, T. H. O., Smith, J. M., Brooks, A. G., Kedzierska, K., Heath, W. R.,
1873 Reading, P. C. and Wakim, L. M. (2017). Resident memory CD8+ T cells in the upper
1874 respiratory tract prevent pulmonary influenza virus infection. *Science Immunology* 2,.

1875 Quinn, T. P., Richardson, M. F., Lovell, D. and Crowley, T. M. (2017). propr: An R-package for
1876 Identifying Proportionally Abundant Features Using Compositional Data Analysis. *Sci*
1877 *Rep* 7, 16252.

1878 Quinn, T. P., Erb, I., Richardson, M. F. and Crowley, T. M. (2018). Understanding sequencing
1879 data as compositions: an outlook and review. *Bioinformatics* 34, 2870–2878.

1880 Raredon, M. S. B., Yang, J., Kothapalli, N., Lewis, W., Kaminski, N., Niklason, L. E. and Kluger,
1881 Y. (2023). Comprehensive visualization of cell–cell interactions in single-cell and spatial
1882 transcriptomics with NICHES. *Bioinformatics* 39, btac775.

1883 Ratnasiri, K., Wilk, A. J., Lee, M. J., Khatri, P. and Blish, C. A. (2023). Single-cell RNA-seq
1884 methods to interrogate virus-host interactions. *Semin Immunopathol* 45, 71–89.

1885 Rossen, R. D., Butler, W. T., Waldman, R. H., Alford, R. H., Hornick, R. B., Togo, Y. and Kasel,
1886 J. A. (1970). The Proteins in Nasal Secretion: II. A Longitudinal Study of IgA and
1887 Neutralizing Antibody Levels in Nasal Washings From Men Infected With Influenza
1888 Virus. *JAMA* 211, 1157–1161.

1889 Roth, G. A., Abate, D., Abate, K. H., Abay, S. M., Abbafati, C., Abbasi, N., Abbastabar, H., Abd-
1890 Allah, F., Abdela, J., Abdelalim, A., et al. (2018). Global, regional, and national age-sex-
1891 specific mortality for 282 causes of death in 195 countries and territories, 1980–2017: a
1892 systematic analysis for the Global Burden of Disease Study 2017. *The Lancet* 392,
1893 1736–1788.

1894 Russell, M. W., Moldoveanu, Z., Ogra, P. L. and Mestecky, J. (2020). Mucosal Immunity in
1895 COVID-19: A Neglected but Critical Aspect of SARS-CoV-2 Infection. *Frontiers in*
1896 *Immunology* 11,.

1897 Rutigliano, J. A., Morris, M. Y., Yue, W., Keating, R., Webby, R. J., Thomas, P. G. and Doherty,
1898 P. C. (2010). Protective Memory Responses Are Modulated by Priming Events prior to
1899 Challenge. *J Virol* 84, 1047–1056.

1900 Rutigliano, J. A., Sharma, S., Morris, M. Y., Oguin, T. H., McClaren, J. L., Doherty, P. C. and
1901 Thomas, P. G. (2014). Highly Pathological Influenza A Virus Infection Is Associated with
1902 Augmented Expression of PD-1 by Functionally Compromised Virus-Specific CD8+ T
1903 Cells. *Journal of Virology* 88, 1636–1651.

1904 Schenkel, J. M., Fraser, K. A., Beura, L. K., Pauken, K. E., Vezys, V. and Masopust, D. (2014).
1905 Resident memory CD8 T cells trigger protective innate and adaptive immune responses.
1906 *Science* 346, 98–101.

1907 Schneider, M. A., Brühl, H., Wechselberger, A., Cihak, J., Stangassinger, M., Schlöndorff, D.
1908 and Mack, M. (2005). In vitro and in vivo properties of a dimeric bispecific single-chain
1909 antibody IgG-fusion protein for depletion of CCR2+ target cells in mice. *European*
1910 *Journal of Immunology* 35, 987–995.

1911 Shinya, K., Ebina, M., Yamada, S., Ono, M., Kasai, N. and Kawaoka, Y. (2006). Influenza virus
1912 receptors in the human airway. *Nature* 440, 435–436.

1913 Slütter, B., Pewe, L. L., Kaech, S. M. and Harty, J. T. (2013). Lung Airway-Surveilling CXCR3hi
1914 Memory CD8+ T Cells Are Critical for Protection against Influenza A Virus. *Immunity* 39,
1915 939–948.

1916 Slütter, B., Van Braeckel-Budimir, N., Abboud, G., Varga, S. M., Salek-Ardakani, S. and Harty,
1917 J. T. (2017). Dynamics of influenza-induced lung-resident memory T cells underlie
1918 waning heterosubtypic immunity. *Science Immunology* 2, eaag2031.

1919 Smillie, C. S., Biton, M., Ordovas-Montanes, J., Sullivan, K. M., Burgin, G., Graham, D. B.,
1920 Herbst, R. H., Rogel, N., Slyper, M., Waldman, J., et al. (2019). Intra- and Inter-cellular
1921 Rewiring of the Human Colon during Ulcerative Colitis. *Cell* 178, 714-730.e22.

1922 Sposito, B., Broggi, A., Pandolfi, L., Crotta, S., Clementi, N., Ferrarese, R., Sisti, S., Criscuolo,
1923 E., Spreafico, R., Long, J. M., et al. (2021). The interferon landscape along the
1924 respiratory tract impacts the severity of COVID-19. *Cell* 184, 4953-4968.e16.

1925 Stary, G., Olive, A., Radovic-Moreno, A. F., Gondek, D., Alvarez, D., Basto, P. A., Perro, M.,
1926 Vrbanac, V. D., Tager, A. M., Shi, J., et al. (2015). VACCINES. A mucosal vaccine
1927 against Chlamydia trachomatis generates two waves of protective memory T cells.
1928 *Science* 348, aaa8205.

1929 Steinbach, K., Vincenti, I., Kreutzfeldt, M., Page, N., Muschaweckh, A., Wagner, I., Drexler, I.,
1930 Pinschewer, D., Korn, T. and Merkler, D. (2016). Brain-resident memory T cells
1931 represent an autonomous cytotoxic barrier to viral infection. *Journal of Experimental*
1932 *Medicine* 213, 1571–1587.

1933 Sterlin, D., Mathian, A., Miyara, M., Mohr, A., Anna, F., Claër, L., Quentric, P., Fadlallah, J.,
1934 Devilliers, H., Ghillani, P., et al. (2021). IgA dominates the early neutralizing antibody
1935 response to SARS-CoV-2. *Science Translational Medicine* 13, eabd2223.

1936 Steuerman, Y., Cohen, M., Peshes-Yaloz, N., Valadarsky, L., Cohn, O., David, E., Frishberg, A.,
1937 Mayo, L., Bacharach, E., Amit, I., et al. (2018). Dissection of Influenza Infection In Vivo
1938 by Single-Cell RNA Sequencing. *Cell Syst* 6, 679-691.e4.

1939 Takaba, H., Morishita, Y., Tomofuji, Y., Danks, L., Nitta, T., Komatsu, N., Kodama, T. and
1940 Takayanagi, H. (2015). Fezf2 Orchestrates a Thymic Program of Self-Antigen
1941 Expression for Immune Tolerance. *Cell* 163, 975–987.

1942 Tang, B. M., Shojaei, M., Teoh, S., Meyers, A., Ho, J., Ball, T. B., Keynan, Y., Pisipati, A.,
1943 Kumar, A., Eisen, D. P., et al. (2019). Neutrophils-related host factors associated with
1944 severe disease and fatality in patients with influenza infection. *Nat Commun* 10, 3422.

1945 Trombetta, J. J., Gennert, D., Lu, D., Satija, R., Shalek, A. K. and Regev, A. (2014). Preparation
1946 of Single-Cell RNA-Seq Libraries for Next Generation Sequencing. *Current Protocols in*
1947 *Molecular Biology* 107,.

1948 Tse, S.-W., Radtke, A. J., Espinosa, D. A., Cockburn, I. A. and Zavala, F. (2014). The
1949 Chemokine Receptor CXCR6 Is Required for the Maintenance of Liver Memory CD8+ T
1950 Cells Specific for Infectious Pathogens. *The Journal of Infectious Diseases* 210, 1508–
1951 1516.

1952 Türei, D., Korcsmáros, T. and Saez-Rodriguez, J. (2016). OmniPath: guidelines and gateway for
1953 literature-curated signaling pathway resources. *Nat Methods* 13, 966–967.

1954 Ualiyeva, S., Lemire, E., Wong, C., Perniss, A., Boyd, A. A., Avilés, E. C., Minichetti, D. G.,
1955 Maxfield, A., Roditi, R., Matsumoto, I., et al. (2024). A nasal cell atlas reveals
1956 heterogeneity of tuft cells and their role in directing olfactory stem cell proliferation.
1957 *Science Immunology* 9, eabq4341.

1958 Uddbäck, I., Michalets, S. E., Saha, A., Mattingly, C., Kost, K. N., Williams, M. E., Lawrence, L.
1959 A., Hicks, S. L., Lowen, A. C., Ahmed, H., et al. (2024). Prevention of respiratory virus
1960 transmission by resident memory CD8+ T cells. *Nature* 626, 392–400.

1961 Wein, A. N., McMaster, S. R., Takamura, S., Dunbar, P. R., Cartwright, E. K., Hayward, S. L.,
1962 McManus, D. T., Shimaoka, T., Ueha, S., Tsukui, T., et al. (2019). CXCR6 regulates
1963 localization of tissue-resident memory CD8 T cells to the airways. *Journal of*
1964 *Experimental Medicine* 216, 2748–2762.

1965 Weisberg, S. P., Ural, B. B. and Farber, D. L. (2021). Tissue-specific immunity for a changing
1966 world. *Cell* 184, 1517–1529.

1967 Wellford, S. A., Moseman, A. P., Dao, K., Wright, K. E., Chen, A., Plevin, J. E., Liao, T.-C.,
1968 Mehta, N. and Moseman, E. A. (2022). Mucosal plasma cells are required to protect the
1969 upper airway and brain from infection. *Immunity* 55, 2118-2134.e6.

1970 Weltzin, R., Traina-Dorge, V., Soike, K., Zhang, J.-Y., Mack, P., Soman, G., Drabik, G. and
1971 Monath, T. P. (1996). Intranasal Monoclonal IgA Antibody to Respiratory Syncytial Virus
1972 Protects Rhesus Monkeys against Upper and Lower Respiratory Tract Infection. *The*
1973 *Journal of Infectious Diseases* 174, 256–261.

1974 Wickenhagen, A., Sugrue, E., Lytras, S., Kuchi, S., Noerenberg, M., Turnbull, M. L., Loney, C.,
1975 Herder, V., Allan, J., Jarmson, I., et al. (2021). A prenylated dsRNA sensor protects
1976 against severe COVID-19. *Science* 374, eabj3624.

1977 Wiley, J. A., Hogan, R. J., Woodland, D. L. and Harmsen, A. G. (2001). Antigen-Specific CD8+
1978 T Cells Persist in the Upper Respiratory Tract Following Influenza Virus Infection. *J*
1979 *Immunol* 167, 3293–3299.

1980 Woof, J. M. and Mestecky, J. (2005). Mucosal immunoglobulins. *Immunological Reviews* 206,
1981 64–82.

1982 Xie, X., Shi, Q., Wu, P., Zhang, X., Kambara, H., Su, J., Yu, H., Park, S.-Y., Guo, R., Ren, Q., et
1983 al. (2020). Single-cell transcriptome profiling reveals neutrophil heterogeneity in
1984 homeostasis and infection. *Nat Immunol* 21, 1119–1133.

1985 Xu, C., Lopez, R., Mehlman, E., Regier, J., Jordan, M. I. and Yosef, N. (2021). Probabilistic
1986 harmonization and annotation of single-cell transcriptomics data with deep generative
1987 models. *Molecular Systems Biology* 17, e9620.

1988 Yao, Y., Jeyanathan, M., Haddadi, S., Barra, N. G., Vaseghi-Shanjani, M., Damjanovic, D., Lai,
1989 R., Afkhami, S., Chen, Y., Dvorkin-Gheva, A., et al. (2018). Induction of Autonomous
1990 Memory Alveolar Macrophages Requires T Cell Help and Is Critical to Trained Immunity.
1991 *Cell* 175, 1634-1650.e17.

1992 Zhang, Q., Bastard, P., Liu, Z., Pen, J. L., Moncada-Velez, M., Chen, J., Ogishi, M., Sabli, I. K.
1993 D., Hodeib, S., Korol, C., et al. (2020). Inborn errors of type I IFN immunity in patients
1994 with life-threatening COVID-19. *Science* 370,.

1995 Zhang, H., Alford, T., Liu, S., Zhou, D. and Wang, J. (2022a). Influenza virus causes lung
1996 immunopathology through down-regulating PPARγ activity in macrophages. *Frontiers in*
1997 *Immunology* 13,.

1998 Zhang, K., Erkan, E. P., Jamalzadeh, S., Dai, J., Andersson, N., Kaipio, K., Lamminen, T.,
1999 Mansuri, N., Huhtinen, K., Carpén, O., et al. (2022b). Longitudinal single-cell RNA-seq
2000 analysis reveals stress-promoted chemoresistance in metastatic ovarian cancer.
2001 *Science Advances* 8, eabm1831.

2002 Zheng, H. B., Doran, B. A., Kimler, K., Yu, A., Tkachev, V., Niederlova, V., Cribbin, K., Fleming,
2003 R., Bratrude, B., Betz, K., et al. (2021). A Treatment-Naïve Cellular Atlas of Pediatric
2004 Crohn's Disease Predicts Disease Severity and Therapeutic Response.
2005 2021.09.17.21263540.

2006 Zheng, H. B., Doran, B. A., Kimler, K., Yu, A., Tkachev, V., Niederlova, V., Cribbin, K., Fleming,
2007 R., Bratrude, B., Betz, K., et al. (2023). Concerted changes in the pediatric single-cell
2008 intestinal ecosystem before and after anti-TNF blockade. *eLife* 12,.

2009 Ziegler, C. G. K., Allon, S. J., Nyquist, S. K., Mbano, I. M., Miao, V. N., Tzouanas, C. N., Cao,
2010 Y., Yousif, A. S., Bals, J., Hauser, B. M., et al. (2020). SARS-CoV-2 Receptor ACE2 Is
2011 an Interferon-Stimulated Gene in Human Airway Epithelial Cells and Is Detected in
2012 Specific Cell Subsets across Tissues. *Cell* 181, 1016-1035.e19.

2013 Ziegler, C. G. K., Miao, V. N., Owings, A. H., Navia, A. W., Tang, Y., Bromley, J. D., Lotfy, P.,
2014 Sloan, M., Laird, H., Williams, H. B., et al. (2021). Impaired local intrinsic immunity to
2015 SARS-CoV-2 infection in severe COVID-19. *Cell* 184, 4713-4733.e22.

2016